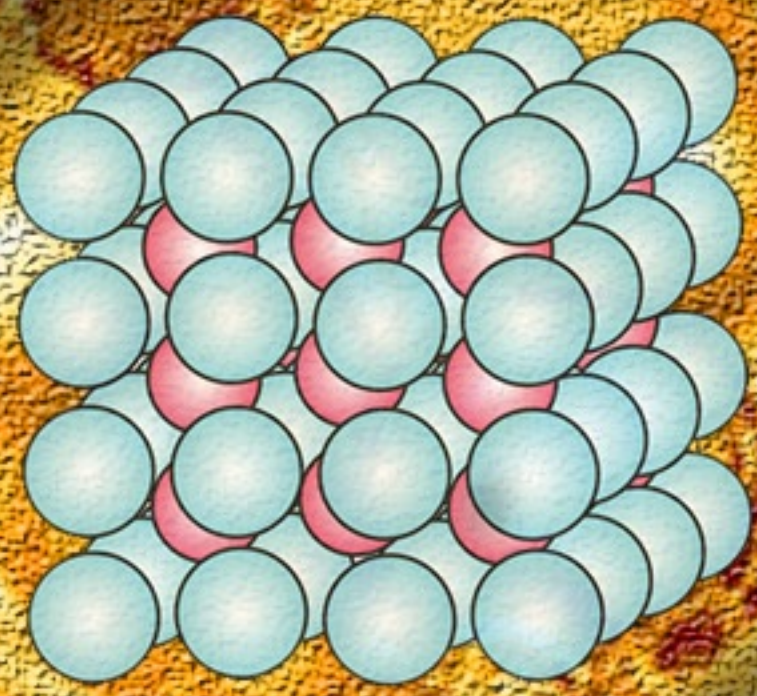
INTERNATIONAL SCIENTIFIC JOURNAL

"MATERIAL SCIENCE"



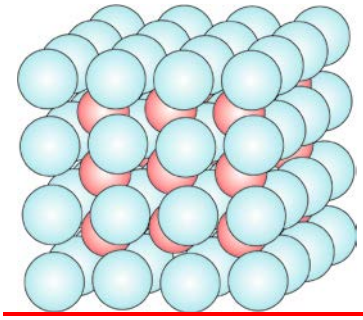
„NONEQUILIBRIUM PHASE TRANSFORMATIONS"

YEAR III, ISSUE 3/2017

ISSN PRINT 2367-749X
ISSN WEB 2534-8477

PUBLISHER: SCIENTICIC TECHNICAL UNION OF MECHANICAL ENGINEERING INDUSTRY 4.0

108 Rakovski str., 1000 Sofia, Bulgaria
tel./fax (+359 2) 986 22 40, tel. (+359 2) 987 72 90,
office@stumejournals.com, www.stumejournals.com



INTERNATIONAL SCIENTIFIC JOURNAL

MATERIALS SCIENCE. NON-EQUILIBRIUM PHASE TRANSFORMATIONS

PUBLISHER:

SCIENTIFIC TECHNICAL UNION OF MECHANICAL ENGINEERING

108, Rakovski Str., 1000 Sofia, Bulgaria
tel. (+359 2) 987 72 90,
tel./fax (+359 2) 986 22 40,
office@stumejournals.com

ISSN PRINT 2367-749X, ISSN WEB 2534-8477
YEAR III, ISSUE 3 / 2017

EDITORIAL BOARD

CHIEF EDITOR
Prof. Dimitar Stavrev – Bulgaria

DEPUTY EDITOR:
Dr. Alexander Krugljakow, Germany
Prof. Sergey Dobatkin, Russia
Prof. Sergey Nikulin, Russia
Prof. Victor Anchev, Bulgaria

RESPONSIBLE SECRETARY:
Assoc. Prof. Tsanka Dikova, Bulgaria

MEMBERS:

Prof. Adel Mahmud, Iraq
Prof. Anna Proikova, Bulgaria
Prof. Bekir Sami Yilbas, Saudi Arabia
Prof. Dermot Brabazon, Ireland
Prof. Dipten Misra, India
Assoc. Prof.Eugeniy Grigoriev, Russia
Prof. F. W. Travis, United Kingdom
Prof. Gennagiy Bagluk, Ukraine
Assoc. Prof. Ibrahim E.Saklakoglu, Turkey
Prof. Iis Sopyan, Malaysia
Prof. Ivan Parshorov, Bulgaria
Prof. Ivanja Markova, Bulgaria
Prof. Janez Grum, Slovenia
Prof. Jens Bergstrom, Sweden
Prof. Leszek Dobrzanski, Poland
Prof. Ludmila Kaputkina, Russia
Prof. Nikolai Dulgerov, Bulgaria
Prof. Omer Keles, Turkey
Prof. Plamen Danev, Bulgaria
Prof. Rui Vilar, Portugal
Prof. Rusko Shishkov, Bulgaria
Prof. Saleem Hashmi, Ireland
Dr. Sefika Kasman, Turkey
Prof. Seiji Katayama, Japan
Prof. Souren Mitra, India
Dr. Sumsun Naher, United Kingdom
Prof. Svetlana Gubenko, Ukraine
Prof. Sveto Cvetkovski, Macedonia
Prof. Ventsislav Toshkov, Bulgaria
Prof. Yovka Dragieva, Bulgaria

C O N T E N T S

STRUCTURAL-PHASE TRANSFORMATIONS DURING CONTINUOUS COOLING OF MEDIUM-CARBON HIGH-STRENGTH STEELS WITH DIFFERENT CONTENT OF MOLYBDENUM AND NIOBIUM
Prof. Koptseva N.V., PhD Chukin D.M., Gushchina M.S. 78

TRANSFORMATION OF HETEROPHASE NON-METALLIC INCLUSIONS "HIGH-MELTING PHASE SURROUNDING WITH LOW-MELTING COVER" IN STEELS UNDER LASER ACTION
Prof.. Dr. Sci. Gubenko S. 82

SCHEME OF TREATMENT AND ITS EFFECT ON THE STRAIN HETEROGENEITY AND STRUCTURAL CHANGES IN BILLETS OF LOW-CARBON STEEL
V.I. Semenov, G.A. Aleshin, A.G. Raab, N. Tontchev, V. Kamburov, E. Yankov 87

NANOCOMPOSITE MATERIALS BASED ON THERMOPLASTIC BLENDS FOR THE TECHNOLOGICAL EQUIPMENT WITH A LONG SERVICE LIFE
Senior lecturer Antonov A., Assoc. Prof. cand. eng. Avdeychik S., Senior lecturer Sarokin V., Prof. Dr. Eng. Struk V.,
Assoc. Prof. cand. eng. Vorontsov A., Assoc. Prof. cand. eng. Mikhailova L. 92

EFFECT OF HOT PLASTIC DEFORMATION ON DECOMPOSITION OF MAGNESIUM SOLID SOLUTION CONTAINING RARE-EARTH METALS
Prof. Rokhlin L.L., PhD. Lukyanova E.A., PhD. Dobatkina T.V., Korolkova I.G., Ovchinnikova O.A. 95

PRODUCTION OF POWDER POROUS MATERIALS FROM MECHANICALLY ACTIVATED ALUMINUM OXIDE
Prof., Dr. Eng., Cor. Member of NAS of Belarus Ilyushchanka A., Cand. Eng., Docent Kusin R., Cand. Eng., Docent Letsko A.I.
Charniak I., Zhehzdryn D., Ilyukevich A. 98

EFFECT OF OXYGEN AND NITROGEN CONTENTS ON THE STRUCTURE OF THE Ti-6Al-4V ALLOY MANUFACTURED BY SELECTIVE LASER MELTING
Prof. Kazantseva N. Dr.of Sci., Prof. Krakhmalev P. PhD., Yadroitsev I. PhD., Fefelov A. PhD., Merkushev A., Ilyinikh M. ,
Vinogradova N. PhD., Ezhov I. PhD Student, Kurennykh T. PhD. 101

ELASTIC PHASE TRANSITION IN METALS: THE PRESSURE EFFECT
Dr. Krasilnikov O.M., Prof, Dr. Vekilov Yu.Kh., PhD Lugovskoy A.V., PhD Belov M.P. 104

INFLUENCE OF THERMAL-CYCLIC DEFORMATION AND HEAT TREATMENT ON THE STRUCTURE AND PHYSICAL PROPERTIES OF STEEL 10
D.Sc. (Eng.), Prof. Prudnikov A., Ph.D. student Prudnikov V. 108

PRESSURE DERIVATIVES OF ELASTIC CONSTANTS OF ALUMINUM ALLOY AMg6 AND NANOSTRUCTURED ALLOY n-AMg6. COMPARISON OF EXPERIMENTAL AND CALCULATED FROM THIRD-ORDER ELASTIC CONSTANTS DATA
Assoc. Prof., Dr. Prokhorov V., Leading Res., Dr. Gromnitskaya E. 111

RESIDUAL STRESSES AND FRACTURE TOUGHNESS BORIDE CERAMIC COMPOSITES WITH MONOCRYSTALLINE MATRIX
Soloviova T.O.,Loboda P.I., Karasevska O.P., Samsonik I.V. 115

C-BETAVOLTAIC ENERGYCONVERTER IN POR-SIC/SI
V.I.Chepurnov, M.V.Dolgopolov, A.V.Gurskaya, A.A.Akimchenko, O.V.Kuznetsov, A.V.Radenko, V.V.Radenko, A.S.Mashnin 119

STRUCTURAL-PHASE TRANSFORMATIONS DURING CONTINUOUS COOLING OF MEDIUM-CARBON HIGH-STRENGTH STEELS WITH DIFFERENT CONTENT OF MOLYBDENUM AND NIOBIUM

СТРУКТУРНО-ФАЗОВЫЕ ПРЕВРАЩЕНИЯ ПРИ НЕПРЕРЫВНОМ ОХЛАЖДЕНИИ СРЕДНЕУГЛЕРОДИСТЫХ ВЫСОКОПРОЧНЫХ СТАЛЕЙ С РАЗЛИЧНЫМ СОДЕРЖАНИЕМ МОЛИБДЕНА И НИОБИЯ

Prof. Koptseva N.V., PhD Chukin D.M., Gushchina M.S.
Magnitogorsk State Technical University, Magnitogorsk, Russia
e-mail: chukindmitry@gmail.com

Abstract/Резюме: *In the article are considered structural phase transformations during continuous cooling of medium-carbon steel with different contents of molybdenum and niobium. The features of the phase transformations course during decomposition of austenite depending on the cooling rate are revealed. The structure and microhardness were studied. Continuous cooling transformation (CCT) diagrams are constructed for all studied chemical compositions. The effect of molybdenum and niobium on the kinetics of phase transformations and the hardness of the steels studied are shown.*

KEYWORDS: MEDIUM-CARBON HIGH-STRENGTH STEEL, STRUCTURAL-PHASE TRANSFORMATIONS, CCT DIAGRAM.

1. Introduction / Введение

One of the strategic directions for the development of the modern metallurgical industry is the creation and introduction of technology for the production of plate products with increased strength characteristics [1-3]. Such high-strength steels are promising materials for the production of high-tech products of a new generation used in various high-tech industries [4-6]. Of particular interest in this respect is the hardening from rolling heat of medium-carbon steels, which makes it possible to obtain a hardness of at least 5000 MPa while maintaining sufficient ductility and viscosity [7, 8]. The development of modes of thermal hardening of steel from rolling heating is impossible without an analysis of the effect of temperature-time cooling parameters on the nature of the final products of decomposition and their properties [9-12]. In addition, such carbide-forming elements as niobium, vanadium and molybdenum can exert a strong influence [13, 14]. Meanwhile, the CCT diagrams of the undercooled austenite decomposition for steels of this class, given in various sources, do not give a sufficiently complete picture of the phase transformations features ~~of~~ and require specification.

In connection with the foregoing, the aim of the work is to study the mechanisms of the undercooled austenite transformation during continuous cooling with various rates of medium-carbon steel alloyed with niobium and molybdenum and determination of the temperature-time parameters of cooling, ensuring its high-strength state.

2. Material and methods of research / Материал и методика исследования

Steel for research were melted in the conditions of a small innovative enterprise «Thermodeform-NMSTU». Their chemical composition is indicated in Table 1.

Table 1. Chemical composition of test steels

Melt	Mass fraction of elements,%						
	C	Si	Mn	Cr	Ni	Mo	Nb
1	0,28	0,24	0,83	0,50	0,90	0,32	0,005
2	0,29	0,27	0,87	0,50	0,85	0,70	0,006
3	0,29	0,11	0,90	0,56	0,92	0,42	0,027

The determination of critical points and the construction of a CCT diagram were carried out using the Gleeble 3500 research complex on samples with a diameter of 10 mm and a length of 80 mm. To transfer the steel to an austenitic state, heating was carried out in a vacuum at a rate of 5 °C/s to 980 °C with an exposure time of 5 min. To construct CCT diagrams samples were cooled at rates of 1, 3, 5, 10, 20 °C/s. During heating and cooling the temperature of the sample was fixed with a chromel-alumel thermocouple.

For microstructure analysis microsections were prepared by the standard method using a resin pressing «Transoptic» on an automated press Buechler Simplimet 1000. To reveal the microstructure the surface of the section was etched in a 4% solution of nitric acid in ethyl alcohol by immersion of a polished surface in a bath with a reagent.

To determine the qualitative and quantitative characteristics of the structure an optical microscope Meiji Techno was used using the Thixomet PRO computer image analysis system. The microstructure at magnifications of more than 1000 times was examined using a scanning electron microscope JEOL JSM 6490 LV in secondary electrons.

Microhardness was determined on a Buchler Mikromet hardness tester by pressing a diamond pyramid with an angle between opposite faces of 136 ° in accordance with GOST 9450-60 at a load of 1 kg and a loading time of 10 s.

This work was carried out within the framework of the main part of the state task of the Ministry of Education and Science of the Russian Federation 2017-05GZ (No. 17.1.18.2412.01 of 09/01/2017, r.№ 1 from 25.01 0,2017). The study was financially supported by Ministry of Education and Science of the Russian Federation within the scope of accomplishment of multiple-purpose project on creation of modern high-tech production with the participation of higher education institution (Contract 03.G25.31.0235).

3. Results and discussion / Результаты и дискуссия

The microstructure of the steel No. 1 samples after cooling at different rates is illustrated in Fig. 1.

At a cooling rate of 1 °C/s bainite with a small amount of martensitic regions is observed in the structure (Fig. 1, a). As the cooling rate increases from 1 to 10 °C/s, the amount of bainite

decreases from 95 to 30%, and the amount of martensite, respectively, increases (Fig. 1, b). At a cooling rate of 20 °C/s, the structure mainly consists of martensite (Fig. 1, c). However, even with such a cooling rate, an insignificant amount of bainite is observed in the structure not exceeding 5%.

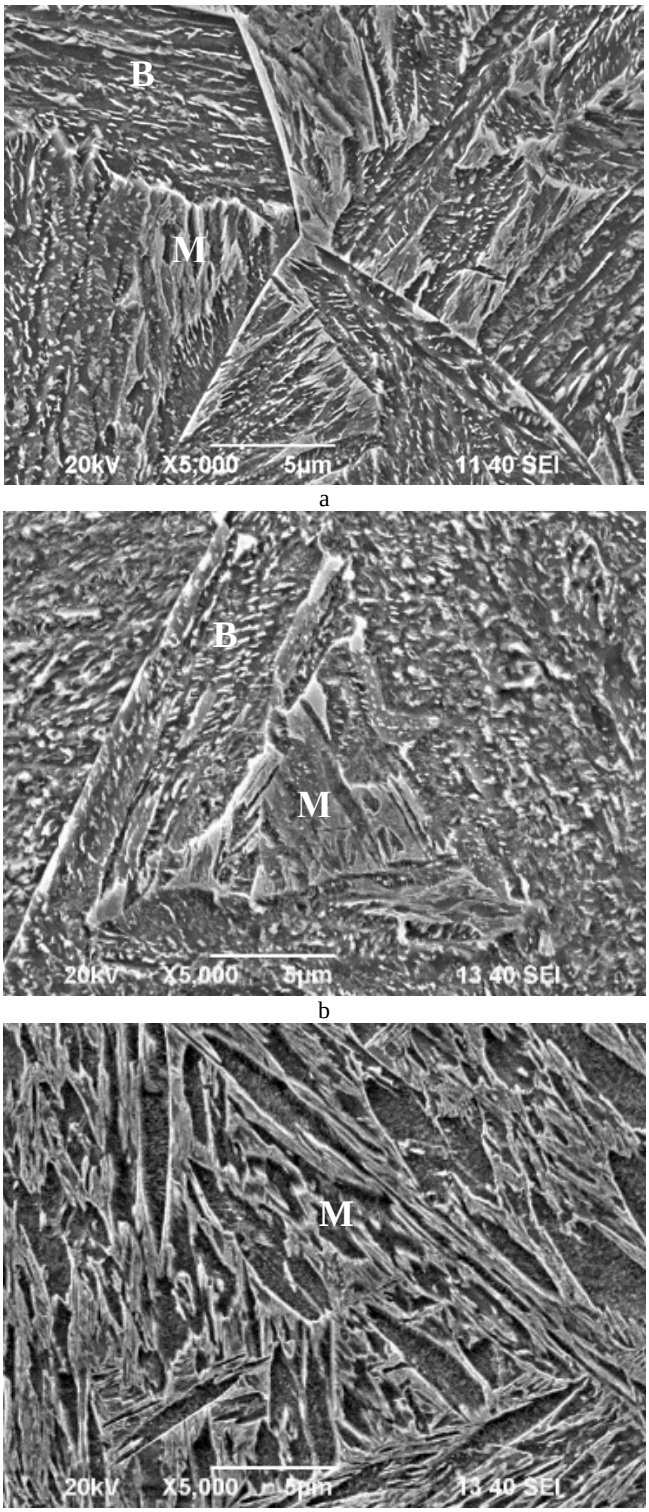


Fig. 1. The microstructure of the steel No. 1 after cooling with the rates 1 (a), 5 (b), 20 (c) °C/s

As the cooling rate increases, the microhardness changes from 3241 MPa (at 1 °C/s) to 5033 MPa (at 20 °C/s), which is caused by an increase in the amount of the martensite component (Table 2).

An analysis of the results shows that in the steel No. 1 at cooling rates from 1 to 20 °C/s two mechanisms of transformation of the undercooled austenite are realized: intermediate (it may be regarded as a martensitic transformation involving the diffusion of carbon atoms) and diffusionless (martensitic).

Upon cooling at a rate of 1 °C/s the decomposition of the undercooled austenite begins with the formation of bainite by an intermediate mechanism at temperatures of 628 °C. As the cooling rate increases, the temperature of the beginning of the bainitic transformation decreases: at 5 °C/s it is 567 °C, at 10 °C/s - 508 °C and at 20 °C/s – 435 °C. At all studied cooling rates diffusionless transformation is realized, the temperature of the beginning of which, depending on the cooling rate, varies from 382 to 430 °C. It should be noted that in the investigated range of cooling rates, the intermediate transformation cannot be completely suppressed. At the cooling rate of 20 °C/s, the amount of bainite is small, the volume effect of the austenite transformation is small and is not fixed by the dilatometric method.

The microstructure of the steel No. 2 samples after cooling at different rates is shown in Fig. 2.

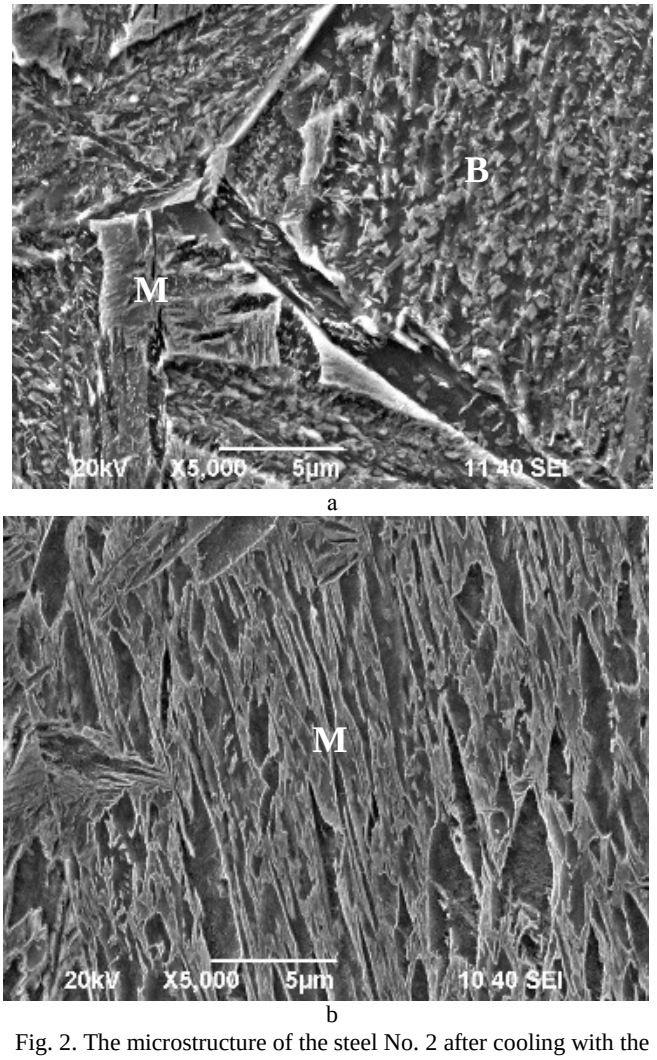


Fig. 2. The microstructure of the steel No. 2 after cooling with the rates 1 (a) и 10 (b) °C/s

The carried out studies showed that at cooling rates from 1 to 5 °C/s in the undercooled austenite decomposition in the steel melt No. 2 like in the steel No. 1 bainite and martensite are observed in the structure (Fig. 2, a). However, the amount of bainite in the steel No. 2 compared with the steel No. 1 is considerably less at the same cooling rate and ranges from 75 to 3%. At a rate of 3 °C/s, the amount of martensite is already 93%, and, beginning with a cooling rate of 10 °C/s, no bainite is found in the structure, and it consists entirely of martensite.

As the cooling rate increases, the microhardness changes from 3888 MPa (at 1 °C/s) to 5423 MPa (at 20 °C/s), which is the same as in the steel No. 1, due to an increase in the martensite component (Table 2).

Thus, with the continuous cooling of the steel No. 2, both bainitic and martensitic transformations of the undercooled austenite are observed. In this case, the bainite transformation is shifted to the right, and its start temperatures have changed significantly. At a speed of 1 °C/s, it starts at 603 °C, at 5 °C/s - 398 °C and is suppressed with a further increase in speed. The martensitic point had dropped to 331-380 °C. Such a change in the transformation temperature, the relative volume fraction of structural components and the microhardness in comparison with the steel No. 1 is associated with an increase in the molybdenum content by two times.

The microstructure of the steel No. 3 after cooling with different rates is demonstrated in Fig. 3.

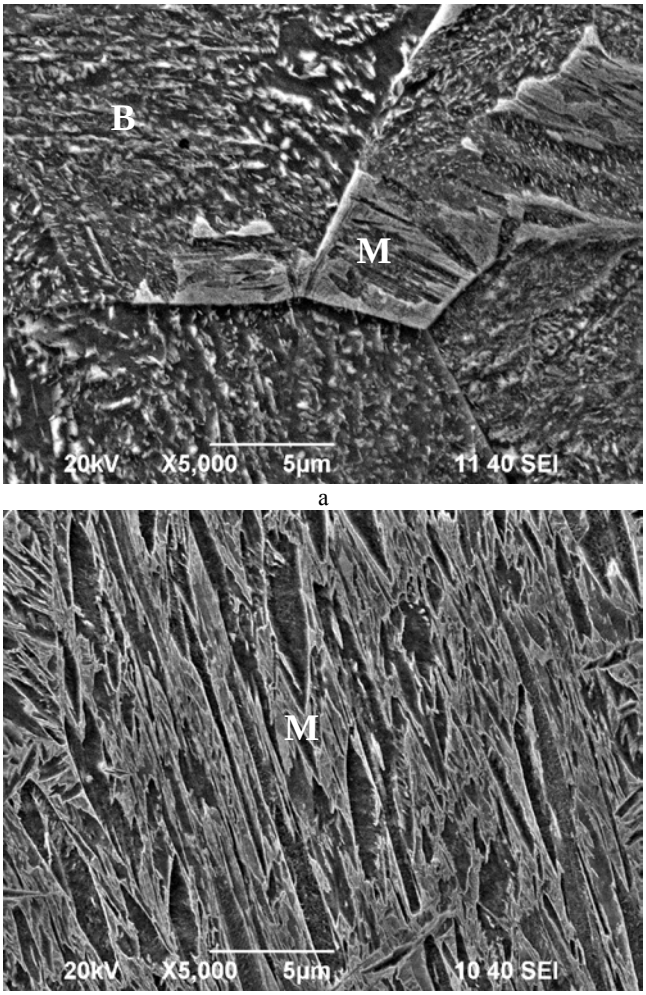


Fig. 3. The microstructure of the steel No. 3 after cooling with the rates 1 (a) и 10 (b) °C/s

Table 2. Quantitative characteristics of the microstructure and hardness of the steel under study at different cooling rates

Steel	Cooling rates, °C/s	Relative volume fraction of structural components, %		Microhardness, MPa
		Bainite (B)	Martensite (M) + $A_{retained}$	
1	1	95	5	3241
	3	50	50	4767
	5	40	60	4915
	10	30	70	4978
	20	5	95	5033
2	1	75	25	3888
	3	7	93	5372
	5	3	97	5484
	10	0	100	5408
	20	0	100	5423
3	1	80	20	3477
	3	30	70	4674
	5	5	95	5192
	10	0	100	5476
	20	0	100	5466

Structural-phase transformation in the steel No. 3 microalloyed with niobium is analogous to the described conversions for steel No. 2. The difference is that the bainite transformation is shifted to the left. This means that the stability of the undercooled austenite is less and approximately the same as in the steel No. 1. Thus, the temperatures of the bainitic and martensitic transformations beginning also differ (Fig. 4). Microhardness with increasing cooling rate varies from 3477 MPa (at 1 °C/s) to 5476 MPa (at 20 °C/s).

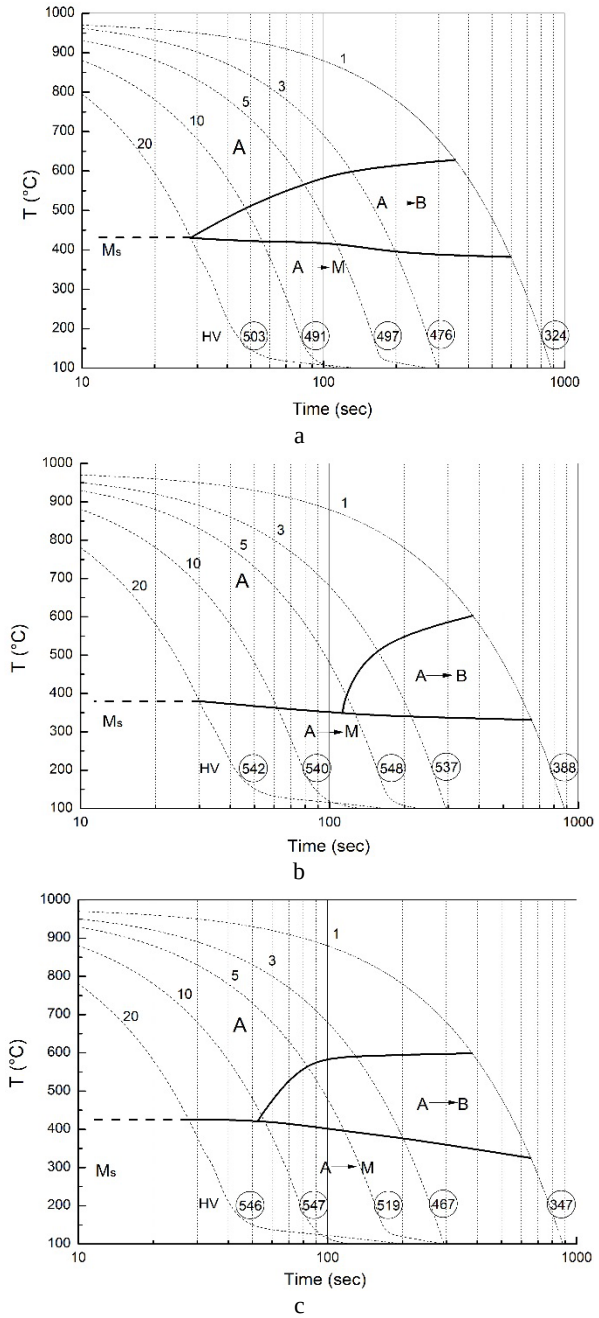


Fig. 4. Continuous cooling transformation diagrams of the undercooled austenite decomposition in the steel No. 1 (a), No. 2 (b), No. 3 (c)

4. Conclusion / Заключение

The complex of studies carried out showed that in medium carbon steel containing about 0.3 % of carbon, a microhardness of more than 5000 MPa can be obtained at cooling rates of 3 °C/s due to alloying with molybdenum in an amount of 0.7 % or at a cooling rate of 5 °C/s due to micro-alloying with niobium in an amount of 0.03 %, which ensures the formation of a martensite structure. The obtained results can be used to create a technology for the production of plate products from medium-carbon steel with increased strength characteristics.

5. Literature / Литература

1. Strategy of development of ferrous metallurgy in Russia for 2014-2020 and for the future up to 2030: the order of the Ministry of Industry and Trade of Russia from 05.05.2014 № 839. URL:http://www.consultant.ru/document/cons_doc_LAW_165502/.
2. Shakhpazov, E.Kh. Key areas of development of metallurgical technology to meet the growing requirements for the quality of steel. – Electrometallurgy, 2011, No. 2, P. 2-12.
3. Ulewicz, R., M. Mazur, O. Bokuvka. Structure and mechanical properties of fine-grained steels. – Transportation Engineering, 2013, Vol. 41/2, P. 111-115.
4. Chukin, M.V., V.M. Salganik, P.P. Poletskov, S.V. Denisov, A.S. Kuznetsova, G.A. Berezhnaya, M.S. Gushchina. Main types and application of nanostructured high-strength sheet products. – Vestnik of Nosov Magnitogorsk State Technical University, 2014, № 4, P. 41-44.
5. Gliner, R.E. Developments in the field of production of high-strength sheet steel in Sweden. – Rolled Products Manufacturing, 2009, № 10, P. 11-18.
6. De Moor, E., P.J. Gibbs, J.G. Speer et al. Strategies for third-generation advanced high-strength steel development. – Iron and Steel Technology, 2010, № 11, P. 133-144.
7. Gorynin, I.V., V.A. Malyshevsky, E.I. Khlusov. Nanostructured structural steels are the breakthrough direction of metal consuming industries. – Innovations, 2010, No. 4, P. 103-107.
8. Chukin, MV, V.M. Salganik, P.P. Poletskov, G.A. Berezhnaya, M.S. Gushchina, A.S. Kuznetsov. Analysis of technical requirements for nanostructured high strength plate steels. – Processing of solid and laminar materials, 2014, No. 2 (41), P.19-28.
9. Stalheim, D.G., R. Glodowsky. Production of fine-grained as-rolled structural plate steels. – Iron and Steel Technology, 2010, № 10, P. 78-84.
10. Pontremoli, M., L. Weber, F. Dilg and others. High-strength steels for thick sheets, pipes and profiles. – Chernye Metally (Ferrous metals), 2006, № 4, P. 58-66.
11. Salganik, V.M., P.P. Poletskov, G.A. Berezhnaya, M.S. Gushchina, D.Yu. Alexeyev. Evaluation of the conjuncture of the world market and the areas of application of nanosized high-strength sheet products. – Modeling and development of metal forming processes: Magnitogorsk, Publishing house of Nosov Magnitogorsk. State. Tech. University, 2015, Issue. 21, P. 39-45.
12. Mok, P.J., K. Overhagen, W. Stelmacher. Development of technology for the production of long products. – Chernye Metally (Ferrous metals), 2010, № 11, P. 30-39.
13. Dudeckaya, L.R., A.N. Glushakov. Investigation of the effect of microalloying with molybdenum and niobium on the hardenability and mechanical properties of structural cemented steels 20ХН3А and 20ХГНМ. – Vestnik of Sukhoi State Technical University of Gomel, 2013, № 2 (53), P. 47-52.
14. Rybakov, A.A., T.N. Filipchuk, V.A. Costin. Features of microstructure and impact strength of welded joints of pipes made of high-strength steel, micro-alloyed niobium and molybdenum. – Automatic welding, 2015, No. 3-4, P. 17-24.

TRANSFORMATION OF HETEROPHASE NON-METALLIC INCLUSIONS "HIGH-MELTING PHASE SURROUNDING WITH LOW-MELTING COVER" IN STEELS UNDER LASER ACTION

ТРАСНФОРМАЦИЯ ГЕТЕРОФАЗНЫХ НЕМЕТАЛЛИЧЕСКИХ ВКЛЮЧЕНИЙ «ТУГОПЛАВКАЯ ФАЗА, ОКРУЖЕННАЯ ЛЕГКОПЛАВКОЙ ОБОЛОЧКОЙ» В СТАЛЯХ ПРИ ЛАЗЕРНОМ ВОЗДЕЙСТВИИ

Prof.. Dr. Sci. Gubenko S.
National Metallurgical academy of Ukraine
Dnepropetrovsk, Ukraine
sigubenko@gmail.com

Abstract. Melting and crystallization of heterophase non-metallic inclusions "high-melting phase surrounding with low-melting cover" was investigated. It was shown that under laser action the initial structure of inclusion-steel matrix boundaries transits into unstable equilibrium high-energy condition that cause development of the dissipation processes connecting with aspiration of system inclusion-matrix to the state with minimum of free energy. In the result of the system heterophase inclusion-matrix transits to the state of unstable equilibrium which determines structure and properties of laser-quenched interphase boundary. Processes of melting, fusion and dissolution of non-metallic inclusions "high-melting phase surrounding with low-melting cover" and also of the melting of steel matrix play the great role in transformation of interphase inclusion-matrix boundaries under laser action.
KEYWORDS: HETEROPHASE NON-METALLIC INCLUSIONS "HIGH-MELTING PHASE SURROUNDING WITH LOW-MELTING COVER", STEEL, STRENGTHENING, LASER TREATMENT

1. Introduction

Except homophase non-metallic inclusions of oxides, nitrides, sulphides, silicates there are different heterophase inclusions in steels having various nature and structure [1]. The first one are inclusions "high-melting phase (ph2) surrounding with low-melting cover (ph-c1)" with interphase boundary ph-c1↔ph2. These inclusions influence on the character of strengthening during laser quenching. In the process of laser treatment different phases of these non-metallic inclusions are fully or partly melted down or are remained hard [1, 2]. Distribution of temperature on the surface of specimen influence on the process of interaction between inclusions and steel matrix [3]. In spite of short-term treatment the energy of laser radiation turns out sufficient for melting of the high-melting phase ph-2 and low-melting cover ph-c1, and also for the development of mass transfer processes which lead to enrichment of steel matrix with the elements of inclusions and also transfer of matrix elements to the surface zone of inclusions. Areas of steel matrix near non-metallic inclusions are the strongly oversaturated solid solution [1, 2]. In steel matrix near non-metallic inclusions the relaxation processes including speed local shear-rotational deformation and elements of return and recrystallization are occured. The character of steels strengthening depends on the types of heterophase non-metallic inclusions and steel matrix, speed transformations which flow in steel matrix. The goal of this investigation was to research the processes of melting, dissolution, crystallization of heterophase non-metallic inclusions "high-melting phase surrounding with low-melting cover" in hyper-nonequilibrium conditions and the influence of non-metallic inclusions on the peculiarities of structural changes in steel matrix and its strengthening under laser treatment.

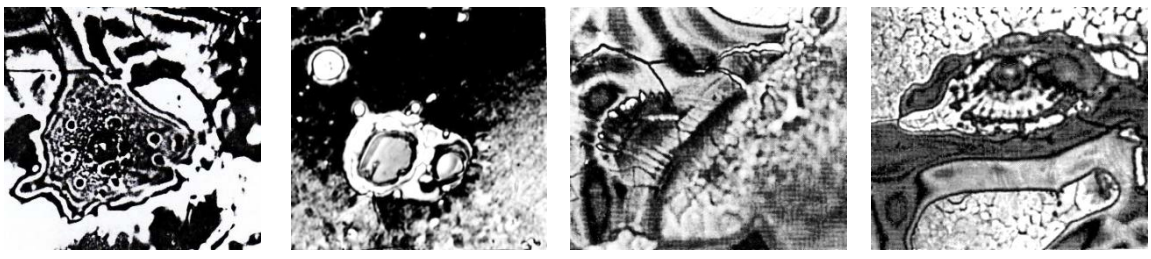
2. Materials and Procedures

Specimens made of steels R7, 08Yu, 08T, 08Kp, 08Ch18N10T,ShCh15, NB-57, 12GS, E3, 60G were irradiated by laser in GOS-30M installation with an excitation voltage of 2,5kV and pulse energy of 10, 18, 25 and 30 J at heating rate of 10^5 ºC/s and cooling rate of 10^6 ºC/s with the action time of (1,0, 2,5, 3,6, 4,2 and 6,0)$\cdot 10^{-3}$ s. Non-metallic inclusions were identified by metallographic, X-ray micro spectral and petrographic methods [1]. Distribution of elements, microhardness and nanohardness of steel matrix near non-metallic inclusions were determined.

3. Results and discussion.

Investigation of high-speed melting and crystallization of heterophase inclusions discovered variety of processes happening in inclusions and steel matrix near inclusions when in the moment of melting micro metallurgical bath is formed and melting of inclusion phases and steel matrix are interacted. Melting of inclusions and both interphase boundaries inclusion-matrix ph-c1↔m and inside inclusions ph-c1↔ph2 connects with formation of heavy disordered areas on surface of inclusions (nucleus of melting) and abnormal mass transfer as the process of melting of homophase non-metallic inclusions.

Both phases of inclusions "high-melting phase surrounding with low-melting cover" in the moment of laser action are melted but the behavior of their phases is differ with degree of melting. Low-melting sulphide or silicate cover is melted fully, high-melting phase of oxide or nitride is melted partly or fully (Fig.. 1, a, b).



a b c d

Figure 1. Dissolution and melting of heterophase non-metallic inclusions "high-melting phase surrounding with low-melting cover" under laser action; x500

On the surfaces of both phases mutual saturation was discovered and interphase boundaries inside inclusions are not legible. The interaction between interphase boundaries ph-c1↔m and steel matrix is similar to interaction for homophase inclusions. But low-melting cover of inclusion has interaction with both steel matrix and high-melting phase of inclusion, so it can to dissolve different atoms on the both sides and it can to accelerate process of dissolution or melting if solubility of elements in sulphide or silicate is sufficiently great. On surface of high-melting phase of oxide or nitride saturating with elements of low-melting cover the heavy disordered areas are formed which pass into liquid low-melting phase. Since in the conditions of laser action the relaxation processes in surface layers of both phases of inclusion "high-melting phase surrounding with low-melting cover" are not have time for happen the time for the achievement of quasiequilibrium conditions on both interphase inclusion-matrix boundaries ph-c1↔m and interphase boundaries inside inclusions ph-c1↔ph2 is increased considerably. Inner stresses in surface layers of both phases of inclusion control the development of melting process which happens in limited volume owing to preservation of contact between phases of inclusion and also between low-melting cover and steel matrix. Elementary act of stresses relaxation causes activation and drawing in considerable number of atoms of both phases of inclusion to the process of disordered similar melting.

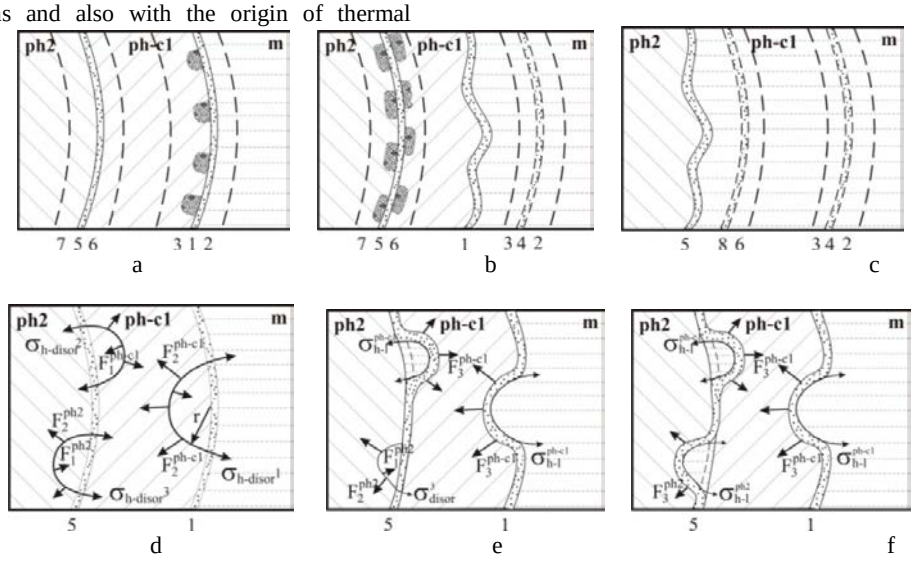
In the moment of laser melting of inclusions "high-melting phase surrounding with low-melting cover" origin the high degree of nonequilibrium of liquid phases (both phases of inclusion and steel matrix) and bifurcation instability of melt. This ensures gradient of vibration pressure on both interphase boundaries inclusion-matrix ph-c1↔m and inside inclusions ph-c1↔ph2 (fully or partly liquid) which checks convective and abnormal flows of mass transfer. Considerable stresses appearing in thin surface layers of both phases of inclusion and steel matrix in the result of local heat flashes of laser radiation together with action of reactive forces of recoil by ejection from zone of treatment of liquid allows to high-temperature deformation of liquid interlayers continuing under crystallization during rapid cooling.

After high-speed melting of inclusions "high-melting phase surrounding with low-melting cover" happens the hyper-nonequilibrium crystallization connecting with formation of microphases, nanophases and sometimes of amorphous phases.

It was shown the formation of gradient and composite zones in steel matrix near non-metallic inclusions take place [1, 2]. Peculiarities of the structure of saturated zones in steel matrix near heterophase non-metallic inclusions depends on their type. All heterophase non-metallic inclusions promote the heterogeneous strengthening of steel matrix. That connects with its microalloying from inner sources – the different phases of non-metallic inclusions and also with the origin of thermal Amorphous cover forms on the base of silicate or sulphide phase. Evidently silicate compositions have mostly display tendency for amorphization. After laser quenching from liquid state in low-melting cover zone with columner shape of grains and liquation is formed (Fig. 1, c, d). Sequence of heavy distortion areas on the surfaces of phase-cover ph-c1 and phase ph2 and also of the movement of both interphase boundaries ph-c1↔m and ph-c1↔ph2 under process of melting one can to present with next image (Fig. 2).

On the surface of phase-cover ph-c1saturating with elements of steel matrix from one side and also saturating with elements of phase ph2 from other side the heavy disordered areas (the areas of melting) are formed (Fig. 2, a, b). Position of both interphase boundaries is changed owing to their melting (Fig. 2, b, c) in dependence on character of mass transfer between both phases of inclusion and phase-cover ph-c1 and steel matrix. Low-melting phase-cover ph-c1 is rapidly melted and it is become the liquid medium in which the high-melting phase ph2 is melted under transition of disordered areas into liquid phase-cover ph-c1. The phase-cover 1 is saturated with elements of phase ph2. Process of melting of the inclusions "high-melting phase surrounding with low-melting cover" is corresponded with the change of distribution of forces near heavy disordered areas in the surface layers in both phases of inclusion (fig. 2, d - f). Action of liquid steel matrix causes the change of surface tension of the phase-cover ph-c1 that breaks equilibrium shape of boundary ph-c1↔m. Action of liquid phase-cover 1 causes the change of surface tension of the high-melting phase ph2 and that breaks equilibrium shape of the boundary ph-c1↔ph2.

Evidently grain boundaries of the both phases of inclusion are melted more quickly than body of grains. That will cause the transition of complexes of former grains (micrograins, nanograins) into liquid state (Fig. 2, g, h). These complexes of phase-cover 1are become the component of structure of liquid steel matrix and liquid layer on the boundary of phases of inclusion containing both complexes of phase of inclusion has complicated structure. Evidently more complicated processes happen in phase-cover 1 that causes with its contact with steel matrix and phase 2 having different chemical composition and structure. Complicated distribution of stresses in phase-cover 1 causes the moment stresses as in the moment of speed melting and both speed crystallization that causes convective mixing of layers of liquid phase. stresses, big density of crystalline defects and localization of relaxation processes having high-speed character. The interaction between phases of non-metallic inclusions and steel matrix promote the formation of complicated composite zones in the areas of saturating. Such zones consist of microstructural, nanostructural and amorphous elements.



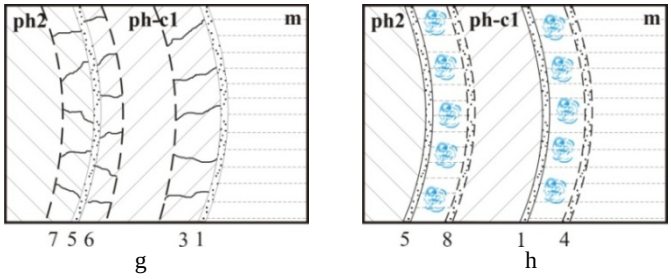


Figure 2. Schemes of laser melting of inclusions "high-melting phase surrounding with low-melting cover": $F_1^{ph\text{-}c1}$, F_1^{ph2}, $F_2^{ph\text{-}c1}$, F_2^{ph2}, $F_3^{ph\text{-}c1}$, F_3^{ph2} – forces of surface tensions on the interphase boundaries, $\sigma_{h\text{-}l}$ – stresses on boundary between hard heavy distortion area of inclusion and liquid steel matrix, $\sigma_{h\text{-}disor}$ - stresses on boundary between disordered area and hard inclusion, 1 – inclusion-matrix boundary, 2 – zone of steel matrix saturation with elements of inclusion, 3 – zone of saturation of phase-cover ph-c1 of inclusion with elements of steel matrix, 4 – initial position of inclusion-matrix boundary, 5 – interphase boundary inside inclusion, 6 – zone of saturation of phase-cover ph-c1 with elements of phase ph2, 7 – zone of saturation of phase ph2 with elements of phase-cover ph-c1, 8 – initial position of interphase boundary inside inclusion

Near inclusions "high-melting phase surrounding with low-melting cover" formation of saturated zones of steel matrix is controlled with the phase-cover ph-c1 which is the source of alloying of steel matrix (Fig. 3). Phase ph2 of inclusion do not takes part in the formation of saturated zones in steel matrix. In the results near these inclusions the composite liquation zones of a few types are formed: the cascade type that bears witness about formation of layers composite zones near such inclusions; "spot" type with heterogeneous distribution of elements of phase-cover ph-c1 and steel matrix; dispersed type that connects with formation of "satellite" particles; complicated layer-dispersed composite with cascade distribution of chemical elements. Characteristic sign of saturated zones is bond of their formation with behavior of the phase-cover ph-c1 in the moment of laser action and with ability of their elements for the speed mass transfer to steel matrix.

Analysis of oversaturated steel matrix areas near non-metallic inclusions "high-melting phase surrounding with low-melting cover" was shown that their structure is heterogeneous. There are a few versions of their structure revealing by heat etching under laser action. It may be one zone, or two zones, or three zones (Fig. 4). By that in non-metallic inclusions surface zone may be absebt or may be one zone or two zones.

Results of distribution of nanohardness of steel matrix were shown that its value (H^i_n) near non-metallic inclusions "high-melting phase surrounding with low-melting cover" (one oversaturated zone or first zone) is more bigger then far from non-metallic inclusions (Table 1). Its value depends from chemical composition and structure of steel defining degree of strengthening by laser action. In the first (or sole) oversaturated zone values of (H^i_n) in 1,41…1,86 times bigger (coefficient K_i) then in steel matrix far from inclusion. These results are closed to resulrs obtaining in [1, 2]. In the second and third oversaturated zones values of nanohardness lower then in the first zone but exceeds values of H_n far from non-metallic inclusions accordingly in 1,2…1,59 and 1,1…1,35 times. Thus cascade of nanohardness values by removal from non-metallic inclusions "high-melting phase surrounding with low-melting cover" was observed. Value of nanohardness of steel matrix in all oversaturated zones near non-metallic inclusions "high-melting phase surrounding with low-melting cover" and value of coefficient K_i depends from condition of non-metallic inclusion "high-melting phase surrounding with low-melting cover"and steel matrix in the moment of laser action. Values of H^i_n and K_i are maximum by fusion of non-metallic inclusions and steel matrix, they are decreased by fusion of steel matrix near hard non-metallic inclusion and they are minimum in the cases of hard condition of non-metallic inclusion and steel matrix.

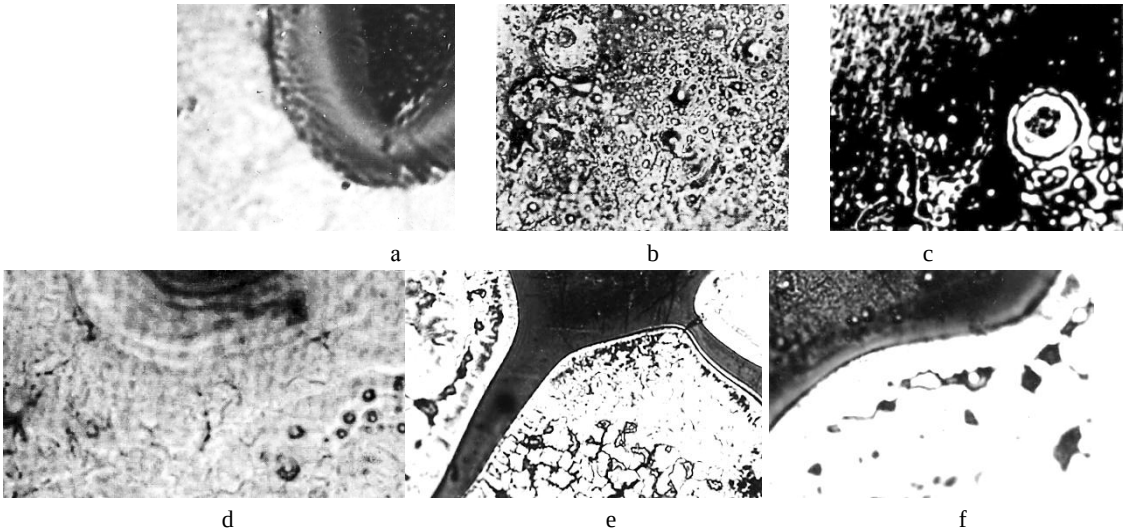


Figure 3. Zones of interaction between heterophase non-metallic inclusions and steel matrix under laser action: a – $FeS+MnO{\cdot}Al_2O_3$, b – $(Fe,Mn)S+Al_2O_3$, c - $MnO{\cdot}SiO_2+MnO{\cdot}Al_2O_3$, d - $MnO{\cdot}SiO_2+Al_2O_3$, e - $MnO{\cdot}SiO_2+Al_2O_3$, f – «satellite» inclusions; x500x6

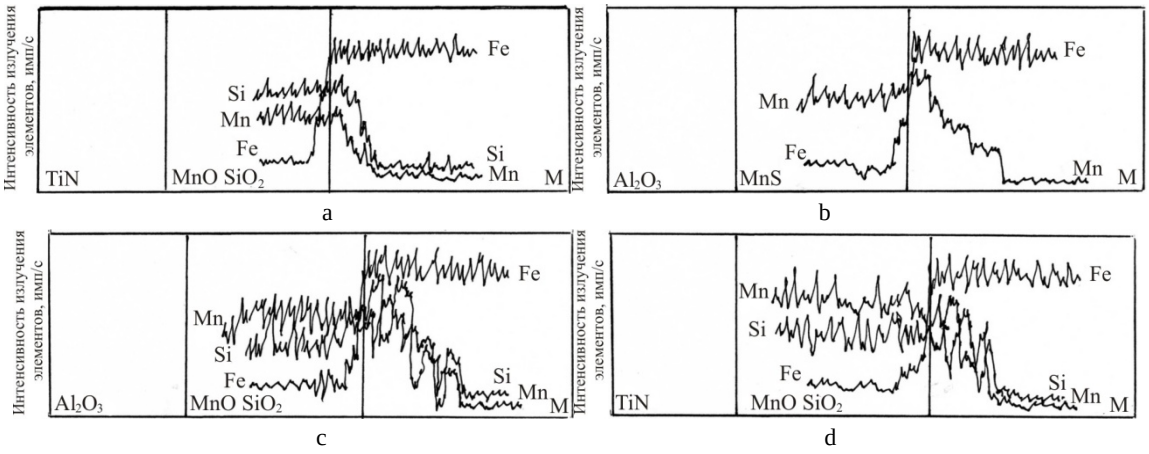


Figure 4. Distribution of chemical elements in inclusions "high-melting phase surrounding with low-melting cover" and oversaturated zones of steel matrix after laser treatment

This connects with phenomemom of maximum satiration of liquid steel matrix by fusion or full melting of non-metallic inclusions [1]. In cases of fusion of oxides, sulphides, silicates in the moment of laser action nanohardness of steel matrix near non-metallic inclusions bigger then near hard non-metallic inclusions and values of coefficient K_i in all oversaturated zones increase. Saturation of steel matrix by elements of non-metallic inclusions and their fix in solid solusion promotes increase of H^i_n and K_i values. Degree of steel matrix saturation in the second and third zones less then directly near non-metallic inclusions (in the first zone) that is confirmed by difference of H^i_n and K_i values.

Table 1.

Values of nanohardness of steel matrix near near non-metallic inclusions "high-melting phase surrounding with low-melting cover" (H^i_n) and far from them H_n under impuls energy 25J and action time $3{,}6 \cdot 10^{-3}$ s

Inclusion ph-c1 – ph2, steel	Condition of inclusion in the time of laser action	Condition of steel matrix in the time of laser action	H_n, x 10, МПа	H^i_n, x 10, МПа in zones		
				1	2	3
$FeS+Al_2O_3$, (Fe,Mn)S+ $MnO \cdot Al_2O_3$, 08Yu	liquid	liquid	286	531 (1,86)	-	-
				524 (1,83)	429 (1,5)	372 (1,3)
$MnO \cdot SiO_2$+ $MnO \cdot Al_2O_3$, 60G	liquid	liquid	620	1054 (1,7)	776 (1,25)	-
		hard		868 (1,4)	-	-
$MnO \cdot SiO_2$+ $MnO \cdot Al_2O_3$, $FeO \cdot SiO_2$+ Al_2O_3,NB-57	liquid	liquid	748	1190 (1,59)	890 (1,19)	-
				1346 (1,8)	980 (1,31)	823 (1,1)
TiN+TiCN, 08T	hard, fusion	liquid	280	483 (1,73)	-	-
				518 (1,85)	361 (1,29)	-
$FeO-TiO_2$+ TiCN, 08T	fusion	liquid, hard	280	470 (1,68)	346 (1,24)	-
				423 (1,51)	-	-
$FeO-MnO+ SiO_2$, 08kp	liquid / fusion	liquid hard	260	444 (1,7)	335 (1,29)	-
				382 (1,47)	-	-

Dependence of nanohardness of the first (or sole) oversaturated zone of steel matrix near non-metallic inclusions "high-melting phase surrounding with low-melting cover" has non-monotonic view for all laser action time (Table 2). This evidence about existence of certain ranges of laser beam energy values that correspond to maximum strenghtening of local layers of steel matrix.

Table 2.

Influence of laser beam energy on nanohardness of steel matrix near inclusion (Fe,Mn)S+ $MnO \cdot Al_2O_3$ in steel 08Uy under different time of action

τ_{imp}, $\cdot 10^{-3}$, s	W_{imp}, J			
	10	18	25	30
1,0	432	495	520	464
3,6	465	520	524	486

Main factor of laser strengthening of local areas of steel matrix is its microalloying from inner sources - non-metallic inclusions “high-melting phase surrounding with low-melting cover”. Creation of cascade of oversaturated zones near these inclusions by formation of local liquational strengthened areas is formation of layers composite near non-metallic inclusions. Structure of these zones maybe single-phase (oversaturated solid solusions) but often dispersal microphases and nanophases – “satellite” particles are observed (see Fig. 3). Chemical composition of “satellite” particles connects with initial inclusion but slightly differs from it thanks to participation of elements of steel matrix in their formation [1, 2]. Process of “satellite” particles formation is connected with abnormal mass transfer in the moment of inclusions and steel matrix melting then in steel matrix areas enriching by elements of phase ph-c1 of inclusions and also containing of complexes (clusters) of former nano-graines of phase ph-c1 are formed. Local areas of the type of metallic emulsion smelts are formed. They are “freezed” by abrupt cooling and clusters of former nano-graines of phase ph-c1 of non-metallic inclusions are crystallized into “satellite” particles. And also process of “satellite” particles formation maybe connects with decrease of solubility of elements of phase ph-c1 of non-metallic inclusions in areas of enrichment of liquid or hard steel matrix by abrupt cooling. In the result in steel matrix near initial inclusions composite structure with dispersal particles are formed. Appearance of “satellite” particles promotes formation of dispersal composite layers or by presence in steel matrix it promotes formation of zones with combine layers-dispersal structure near non-metallic inclusions “high-melting phase surrounding with low-melting cover”. Obviously variation of regime of laser action will allows to regulate structure of these composite systems.

4. Conclusions.

Peculiarities of formation of contact interaction zones in steel matrix in the conditions of abnormal mass transfer from inner sources (non-metallic inclusions “high-melting phase surrounding with low-melting cover”) by laser treatment are connected with origin of liquational strengthened zones representing different types of composite layers. Gradiental zones with cascade and “spot” distribution of elements and nanohardness, dispercal zones with different types of strengthening micro- and nanophases, “tunnel” zones, and also zones with combine structure were formed.

5. Literature.

1. Губенко С.И. Неметаллические включения в стали. – Днепропетровск: АРТ-ПРЕСС, 2005, 536с. (Губенко С.И., Парусов В.В., Деревянченко И.В.)
2. Губенко С.И. Неметаллические включения в стали. Киев, Наукова думка. 2016, 528с. (Губенко С.И., Ошкадеров С.П.)
3. Денисенко О.І. Розподіл температури одновимірного зразка в умовах місцевої термообробки / О.І. Денисенко, В.І. Цоцко, І.М. Спиридонова, Б.Г. Пелешенко // Фізика і хімія твердого тіла. – Т.9. – № 1 (2008). – с. 181-184.

SCHEME OF TREATMENT AND ITS EFFECT ON THE STRAIN HETEROGENEITY AND STRUCTURAL CHANGES IN BILLETS OF LOW-CARBON STEEL

СХЕМА НАГРУЖЕНИЯ И ЕЕ ВЛИЯНИЕ НА НЕОДНОРОДНОСТЬ ДЕФОРМАЦИИ И СТРУКТУРНЫЕ ИЗМЕНЕНИЯ В ЗАГОТОВКАХ ИЗ НИЗКОУГЛЕРОДИСТОЙ СТАЛИ

V.I. Semenov[1, 2], G.A. Aleshin[2], A.G. Raab[2], N. Tontchev[3], V. Kamburov[3], E. Yankov[4]
[1]Institute of Strategic Studies, Ufa, Russia
[2]Ufa State Aviation Technical University, Ufa, Russia,
[3]Todor Kableshkov Higher School of Transport, Sofia, Bulgaria
[4]University of Ruse Angel Kanchev, Ruse, Bulgaria

Annotation: *The paper presents the results of numerical modeling of the conventional drawing and free torsion processes of rods made of low-carbon steel using the "DEFORM-3D" software package. The heterogeneity of the strain intensity distribution in the investigated processes revealed in the model basically corresponds to real physical experiments with similar parameters of the structural heterogeneity. A mutual correspondence of the ductility diagram to the character of the structural changes in the samples deformed by free torsion is established, and the limiting values of the ductility margin, the excess of which leads to the development of fracture processes.*

KEYWORDS: SEVERE PLASTIC DEFORMATION, MATHEMATICAL MODELING, DRAWING, FREE TORSION, MICROSTRUCTURE, STRAIN HETEROGENEITY, MICROHARDNESS, DUCTILITY DIAGRAM.

1. Introduction

Severe plastic deformation (SPD) is one of the most effective ways to enhance the complex of physicomechanical properties of metallic materials by refining the structure to ultrafine-grained (UFG) and nanocrystalline (NC) states. For the formation of UFG and NC structures, as a rule, complex deformation schemes are used: high pressure torsion, equal-channel angular pressing, screw extrusion, etc. [1-3].

Despite the differences in the loading conditions, all these schemes combine one thing - the structure refinement occurs due to active shear deformation of the metal under constrained conditions under the joint action of compression and tension. Further development of SPD methods involves the creation of combined loading schemes with the obligatory inclusion of the shear component of the deformation.

The most known and widespread scheme of pure shear is free torsion [4]. The combination of this scheme with the reduction scheme used for drawing can be promising for dispersing the structure, and as a result, increasing the complex of mechanical properties.

In this connection, the present paper aims to study the effect of two different loading schemes, conventional drawing and free torsion, on the change in the intensity of deformation and the transformation of the structure corresponding to these changes occurring in low-carbon steel with the selected treatments, as well as establishing the relationship between these changes and mechanical properties.

To solve this problem, it is proposed to estimate the intensity distribution of plastic deformation using numerical simulation, which will allow comparing the results of calculations with the observed changes in structure and properties.

2. Material and methods of research

Low-carbon steel Fe-0.1C in the as-received condition - a calibrated rod with a diameter of 10 mm in accordance with RF standard 10702-78 – was used as the material for investigation. When developing a numerical model, the rheological properties of low-carbon steel Fe-0.1C were selected according to the recommendations in [5].

To implement the procedure of numerical simulation, the standard software package "DEFORM-3D" was used.

In order to carry out the simulation in"DEFORM-3D" software package, 3D models were previously created in the software product "Compass-3D".

2.1. Accepted assumptions to the drawing model

1) the material of the billet in the as-received state is isotropic and there are no initial stresses and strains in it;
2) the temperature of the deformation environment was assumed to be 20° C;
3) the tool is absolutely rigid, and the geometry of the tool is automatically recorded;
4) the material of the initial billet was assumed to be ductile;
5) for modeling, 100 steps were selected, taking into account the full passage of the billet in the dies and obtaining a stable result;
6) the billet is divided into 45,000 trapezoidal elements;
7) coefficient of friction between the billet and the tool according to Siebel is 0.12;
8) drawing speed – 0.95 mm/sec;
9) the number of transitions is 6;
10) the degree of deformation on one pass is 15 ... 20%.

2.2. Accepted assumptions to the free-torsion model

1) the tool is an absolutely rigid body;
2) the material of the initial billet was assumed to be ductile;
3) diameter of the initial billet is 10 mm, length 250 mm;
4) the number of finite elements is 35,000;
5) the simulation was carried out in 180 steps with a time step of 1 sec. and a rotation speed of 12.5 rpm;
6) processing temperature is 20° C;
7) the number of revolutions is 16.

For in-situ tests, drawing through conical dies was used. Free torsion of the samples was carried out on a lathe with cantilever fixation of both ends of the billet in a rotating and stationary cartridge.

Rods from low-carbon steel Fe-0.1C were subjected to two types of deformation treatment [6, 7] - conventional drawing and shear deformation by free torsion. In the process of research, the effectiveness of the deformation effect on the structure was compared with conventional drawing and free torsion. Loading schemes are chosen in such a way that in the future it will be possible to analyze the structural and strength changes in the realization of two different types of deformation - compression with shear (when drawing) and shearing (with free torsion).

Traditional drawing was carried out in several passes in a drawing mill with a force of 30 kN with a step-wise reduction in diameter from 10 mm to 7 mm. Torsional deformation (pure shear) was carried out on a lathe with a variable speed of rotation, changing the speed from 10 to 30.

The value of the deformation by drawing was calculated from the formula

$$\varepsilon = [(S_o - S_1)/S_o] \times 100\%, \quad (1)$$

where S_o – cross-sectional area of rod before drawing, S_1 – after drawing [6-8]

The degree of shear deformation intensity (in the physical experiment) at torsion was determined as

$$\Lambda' = \operatorname{tg} \varphi, \quad (2)$$

where φ – angle of twist of the original generator [7], i.e. the angle between the tangent to the generator and the projection of the axis of the rod to the tangent plane (Fig. 1).

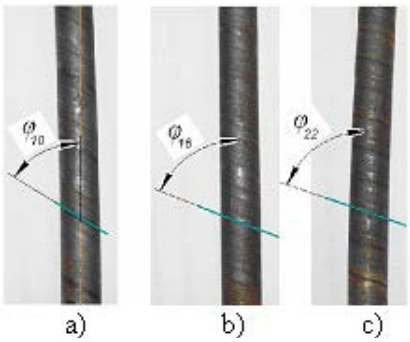


Fig. 1. *Scheme for determining the twist angle and the view of the rods after deformation by free torsion: φ - angle of twisting of the rod: a) - 10 revolutions; b) 16 revolutions; c) 22 revolutions.*

It should be noted that the quantity Λ', calculated from formula (2), characterizes the intensity of the accumulated strain directly in the surface layer of the rods. In the volume of rods, the change in Λ 'can be represented in the form $\Lambda' = \frac{\varphi D}{2l}$ [9], where *D* is the diameter, *l* is the length of the working part of the rod.

The number of passes for drawing (n_d) and the number of revolutions at torsion (n_{rev}), as well as the diameters and degrees of deformation of the rods are given in Table 1.

Table 1. *Deformation regimes of rods from low-carbon steel Fe-0.1C*

Simple drawing			**Torsion (Ø = Ø$_o$)**		
n_d	**Ø**, mm	ε %	**n_{rev}**	**φ**	**Λ′**
1	9.6	7	10	57°	1,5
2	9.4	12	16	68°	2,5
3	8.0	36	22	70°	3,5
4	7.7	42			
5	7.0	51			

The initial diameter of the rods is ***Ø$_0$ = 10 mm***, ***$t_{def.}$ = 20° C***. ***Ø*** - diameter of rods after deformation, ε% - cumulative deformation at drawing.

To reveal the features of the microstructure of the material in the as-received and deformed states, metallographic analysis was performed on light, as well as scanning and transmission electron microscopes. Mean size of grains, features of cellular and dislocation structure of ferrite were determined, the nature of the location of microcracks was studied, and the size and distribution of Fe_3C particles were estimated [10]. In addition, the microhardness HV was measured at a load of 1 N and a holding time of 10 sec in the cross-section of the rods before and after deformation. The error of measurements of these values did not exceed 12%.

3. Results of experiments and their discussion.

On the basis of the obtained results of mathematical modeling, the deformation intensity Λ by the diameter of the rod was determined, for the sake of clarity, presented in a graphical form in Fig. 2. The graph shows a slight change in the exponent Λ from the periphery to the center of the sample. Thus, one can testify to the "softness" of such a deformation scheme as simple drawing.

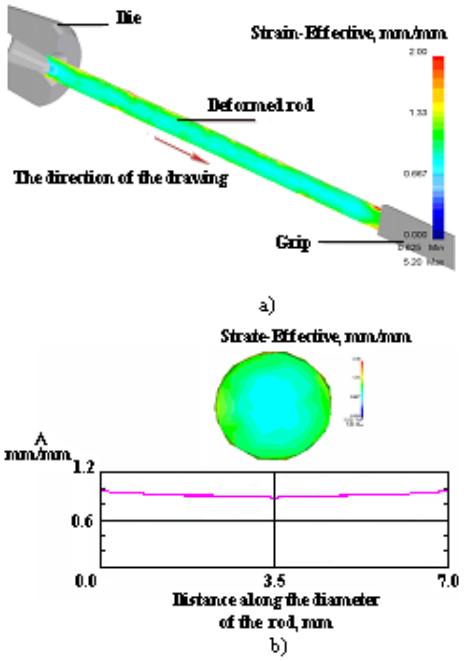


Fig. 2. *Mathematical modeling of the distribution of deformation intensity Λ when drawing rods from low-carbon steel Fe-0.1C, the fifth passage: a) general view of the deformable rod, steady-state stage, longitudinal section; b) the change in Λ along the diameter of the rod in the cross section.*

Fig. 3 shows the distribution of the intensity of the accumulated strain along the surface, and also in the cross-section of the rod after free torsion. As follows from this figure, the degree of deformation Λ increases nonlinearly from the value Λ ≈ 0.5 at the center to Λ ≈ 2.3 in the peripheral region of the rod, which is a characteristic feature of the development of shear deformation [7]. A similar character of the inhomogeneous distribution of Λ in the radial direction was observed by the author of [11] with free torsion of cylindrical samples from a titanium alloy Ti-6Al-4V

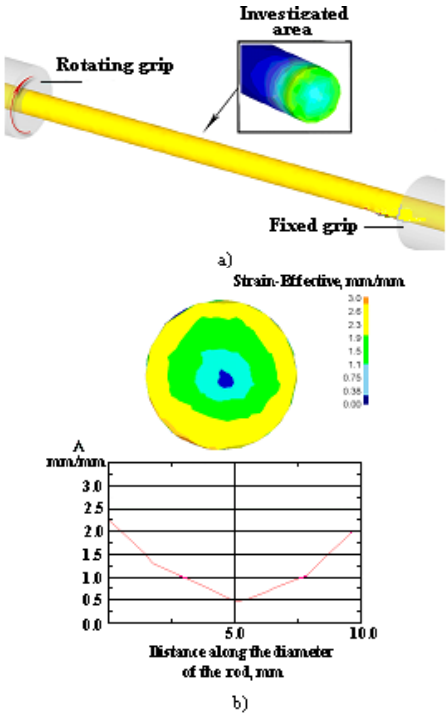
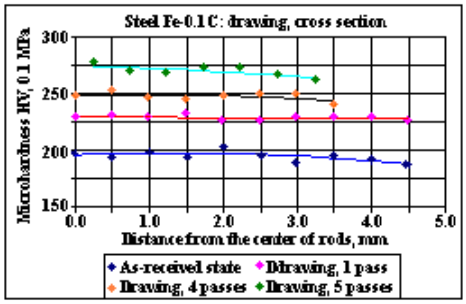


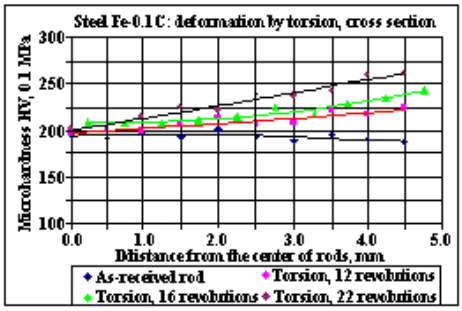
Fig. 3. *The pattern of the distribution of the strain intensity of Λ in the cross section of the sample after free torsion (16 revolutions): the general view (a) and the cross section (b) of the deformable rod.*

For the analysis and interpretation of the results obtained in the numerical model, field experiments on simple drawing and free torsion were carried out according to the method described above, observing the processing regimes adopted in the model.

In order to reveal the peculiarities of plastic deformation in the volume of deformed rods, the microhardness HV was measured by the diameter of the cross-section of the rods. Graphs of variation of HV along the radius of the cross-section of deformed rods are shown in Fig. 4.



a)



b)

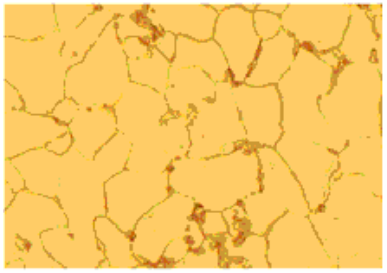
Fig. 4. *Changing of microhardness of low-carbon steel Fe-0.1C on the diameter of the cross-section of the rod after deformation processing: a) by drawing; b) by free torsion*

As can be seen from the presented graphs, the values of microhardness in the as-received rods of low-carbon steel Fe-0.1C are approximately the same in the central and peripheral areas of the rods. After simple drawing with an increase in the degree of deformation (the number of passes) the values of HV grow almost uniformly throughout the cross section of the rods (Fig. 4a). This indicates a relatively homogeneous character of the deformation by simple drawing along the entire volume of rods, which is confirmed by the results of structural studies. The data presented correspond basically to the results of modeling and indicate a correlation between the intensity of deformation and mechanical properties.

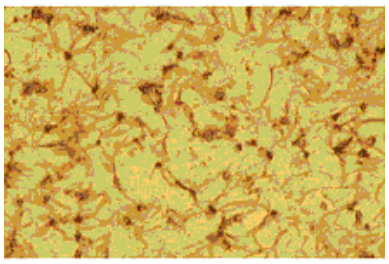
A more heterogeneous character of the change in microhardness is observed with torsional deformation (Fig. 4b). Thus, in the central regions of the rods after torsion, the values of microhardness remain at the level of the as-received samples. At the same time, at the periphery they reach a value close to the values of HV after deformation by simple drawing by 51%. Such a picture of the change in microhardness in the central and peripheral regions of the rods correlates with the results of [12] on torsion with the simultaneous expansion of rods from low-carbon steel Fe-0.1C and is directly related to the heterogeneity of purely shear deformation occurring during torsion [11].

The change in microhardness due to an increase in the intensity of deformation is confirmed by metallographic studies. Fig. 5-6 show photographs of the microstructure of rods from low-carbon steel Fe-0.1C in the as-received state and after deformation treatment.

As can be seen in Fig. 5a, basically equiaxed grains of ferrite with comparatively rectilinear boundaries and average sizes of $d_{av} \approx$ 12-13 μm are observed throughout the cross-sectional area of the bars. Rounded, often stretched into chains, particles of degenerate Fe_3C perlite of indefinite shape with dimensions $d_{Fe3C} \approx$ 0.2-3.0 μm are randomly distributed along the boundaries of the ferrite grains (Fig. 5).



a)



b)

Fig. 5. *Microstructure of low-carbon steel Fe-0.1C, cross-section, central areas of rods: a) the as-received state; b) deformation by drawing, 5 passes; x1000*

Table 2 shows the values of the microstructure parameters in the cross sections of these rods.

Table 2. *Average size of grains in rods from low-carbon steel Fe-0.1C in the as-received and deformed states*

Type of processing	d_3, μm, cross-section
As-received state	12.7
Drawing, 5 passes	7.5
Torsion deformation, 16 revolutions, central part of the rod	12.0

When studying the structure in the cross section of deformed rods after 5 deformation passes by simple drawing, it is established that the structure of the alloy is relatively uniform, the grains (ferrite) are non-equiaxed, strongly deformed, often curved, the boundaries are tortuous, the grain sizes are $d_3 \sim$ 7.5 μm (Fig. 5b). In general, the microstructure in the central and peripheral areas of the rods is identical. The nature of the distribution and the dimensions of the particles of perlite practically have not changed.

In alloy samples subjected to torsional deformation, a different picture is observed. In the central part of a rod deformed by free torsion, the dimensions of the ferrite grains, as well as the perlite particles, practically did not change (Table 2), although chaotically distributed deformed grains of ferrite are present in the structure. At the same time, in the peripheral parts of the rods the structure is represented mainly by deformed ferrite grains with curved boundaries, similar to the one shown in Fig. 6a. In addition, in the peripheral regions of the samples near the lateral surface of the rods, after only 16 revolutions, single microcracks are observed, mainly at interphase boundaries.

Electron microscopic studies have shown that disoriented cells are observed over the entire volume of rods in deformed ferrite grains after drawing. They are, as a rule, elongated in the direction of drawing, their dimensions are ≈ 0.3-0.5 μm wide and ≈ 1-3 μm in length. In samples subjected to free torsion by 16 revolutions, elongated cells are also observed in the peripheral regions, but they have a noticeably greater misorientation than after drawing. This is evidenced by the presence not only of azimuthal smear, but also of spot reflexes on electron diffraction patterns. In addition, the cells in the peripheral parts of the samples after torsion are smaller than the cells after drawing - their width does not exceed 0.2-0.3 μm, and the length is usually not more than 0.5-1 μm (Fig. 6).

Despite the peripheral region, in the microstructure of the central part of the samples, after torsion, slightly disoriented arbitrary

shaped cells are observed (Fig. 6a). These results indicate a lower intensity of the accumulated strain in the central region of the samples during torsion, which correlates with the data on the measurement of microhardness and modeling results.

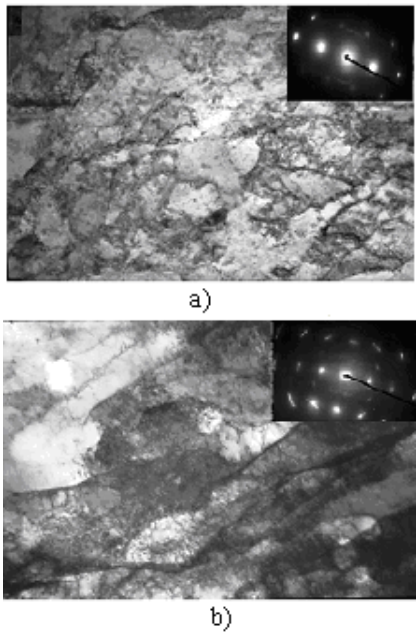


Fig. 6. *Electron microscopic images of the structure of samples from low-carbon steel Fe-0.1C, deformed by free torsion: a) the central region of the rod, the axis of the zone [111]; b) the peripheral region of the rod, the axis of the zone [110]; x29000.*

In order to determine the margin of ductility during torsional deformation, a ductility diagram of low-carbon steel Fe-0.1C in the as-received state was constructed (Fig. 7). In addition to the basic regime (n = 16), torsion experiments were performed with a smaller (n = 10) and a larger number of revolutions (n = 22).

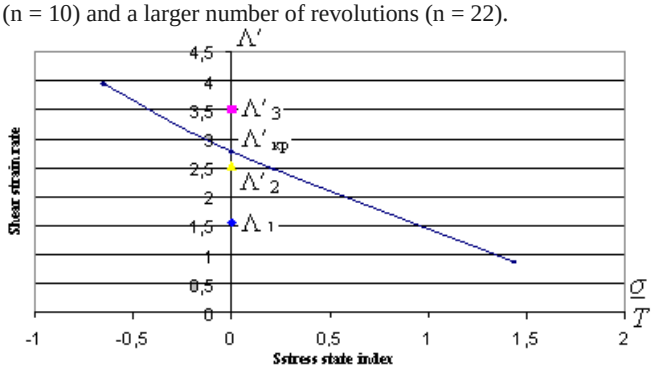


Fig. 7. *The diagram of ductility of low-carbon steel Fe-0.1C in the as-received state and the values of the accumulated strain during torsion: Λ'1 ≈ 1.5 (n = 10 rev.); Λ'2 ≈ 2.5 (n = 16 rev.); Λ'3 ≈ 3.5 (n = 22 rev.); Λ'cr ≈ 2.8*

As is known [7], the ductility diagram allows us to estimate the level of accumulated strain and determine the margin of the ductility reserve of the investigated material during deformation treatment. In Fig. 7 on the ordinate axis, the points are the value of the accumulated deformation for each number of revolutions during torsional deformation.

According to this diagram, the margin of ductility during torsion of rods from low-carbon steel Fe-0.1C is exhausted at a critical strain degree $\Lambda'_{cr} \approx 2.8$. The values of the strain degrees $\Lambda'_1 \approx 1.5$ (n = 10 rev.) and $\Lambda'_2 \approx 2.5$ (n = 16 rev.) are below the value Λ'_{cr} and do not exhaust the margin of ductility. Accordingly, at these strain degrees, microcracks practically do not form and do not develop. However, at $\Lambda'_3 \approx 3.5$ (n = 22 rev.), a well-developed network of microcracks is observed in the alloy structure (Fig. 8), since $\Lambda'_3 > \Lambda'_{cr}$, which leads to the destruction of the sample with further torsion.

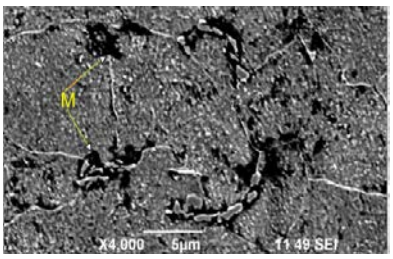


Fig. 8. *Deformation by torsion, 22 revolutions, the central part of the rod, SEM, x4000, M - microcracks at the interface boundaries*

As noted above, the establishment of direct dependence of the modeling parameters of the deformation processes of alloys and the structural changes that occur in them will allow us to realize new approaches to the development and management of technological processes of deformation processing of metallic materials for grinding the structure and forming the targeted set of their physico-mechanical properties.

As can be seen in Fig. 2 and 3, the strain intensity distribution Λ calculated by modeling is ~ 0.8 after simple drawing. For the degree of deformation by drawing ε ≈ 51% (respectively, for $Ø_0$ = 10 mm and $Ø_1$ = 7 mm), the value of the logarithmic stretching is $e = \ln S_o / S_1 \approx \ln 78.5 / 38.5 \approx \ln 2.04 \approx 0.71$. The closeness of the values of Λ and e for the process of drawing testifies to a certain correspondence between the data obtained by modeling and in a physical experiment.

Obtained in a physical experiment, Λ after 16 revolutions of free torsion (Table 1) reaches a value of 2.5, which is close to the value Λ '≈ 2.3. It should be noted that the change in the strain intensity (Figures 2 and 3) also mainly correlates with the character of the change in microhardness along the radius of the cross section of deformed rods, the values of which are shown in Fig. 4.

Both in the model and in the real experiment it was established that deformation of the rod by free torsion leads to a significant structural heterogeneity and a gradient of mechanical properties from the center of the rod to its surface.

On the basis of the obtained results, it was proposed to study the shear drawing process to be able to improve the methods of deformation processing of long-length products and significantly increase their operational properties [13, 14]. This scheme, presumably, will allow realizing more fully the advantages of simple drawing and free torsion.

4. Conclusions:

1. Various types of cold deformation processing of rods from low-carbon steel Fe-0.1C were performed - traditional drawing and free torsion. A significant heterogeneity of the structural changes and the nature of the distribution of the intensity of plastic deformation under the given types of deformation processing of the alloy are revealed.
2. It is shown that deformation by simple drawing leads to a practically homogeneous structure refinement and, accordingly, to a uniform change in microhardness in the bulk of the billet. At the same time, under deformation by free torsion, a substantially heterogeneous, so-called gradient structure is formed.
3. The mutual correspondence of the ductility diagram of low-carbon steel Fe-0.1C and the nature of the structural changes in the samples deformed by free torsion is established. The marginal values of the ductility, the excess of which leads to the development of fracture processes, are established.
4. It is shown that the results of modeling of simple drawing and free torsion, basically, correspond to a real physical experiment with similar strain parameters. This testifies to the correctness of the applied approaches and the prospects of the mathematical modeling method for the development and improvement of new technological processes for metal working with pressure.

The publication was prepared within the framework of the state task of the centre for oil and gas technologies and new materials SASI ISR RB for 2017

ACKNOWLEDGEMENTS: **The authors acknowledge gratefully financial support by the RFBR through project № 17-08-00720.**

5.Rreferences

[1]. Valiev R.Z., Alexandrov I.V. Bulk nanostructured metallic materials: preparation, structure and properties. – M.: IKC "Akademkniga", 2007. – 398 p. (in Russian).
[2]. Kaibyshev O.A., Utyashev F.Z. Superplasticity, refinement of the structure and processing of hard-deformable alloys. – M.: Nauka, 2002. – 438 p. (in Russian).
[3]. Beygelzimer Ya.Yu., Varyukhin V.N., Orlov D.V., Synkov S. G. Screw extrusion – process of deformation accumulation. – Donetsk: Firm "TEAN", 2003. – 87 p. (in Russian).
[4]. Borodin M.A. Resistance of materials. – M.: Drofa, 2001. – 288 p. (in Russian).
[5]. Marochnik steels and alloys / V.G. Sorokin, A.V. Volosnikova, S. A. Vyatkin, etc., Moscow: Mashinostroenie. 1989. 640. (in Russian).
[6]. I.L. Perlin, M.Z. Ermanok. The theory of drawing. – M.: metallurgy, 1971, 447 p. (in Russian).
[7]. Kolmogorov V.L. Mechanics of metal forming // UPI. 2001. P. 836. (in Russian).
[8]. A.N. Levanov, V.L. Kolmogorov, S.P. Burkin, B.R. Kartak, etc. Contact friction in the processing of metals by pressure. – M.: "Metallurgy", 1976. – 416 p (in Russian).
[9]. Verbilo D.G. Peculiarities calculate the true curves of loading in torsion. Problems of strength, No. 3, 2011 Pp. 110 -123. (in Russian).
[10]. Saltykov S.A. Stereometric metallography. – M.: "Metallurgy", 1976. – 273 p. (in Russian).
[11]. Berdine V.K. The formation of microcrystalline structure in titanium VT6 alloy during hot deformation of two-component loading // Vestnik USATU. Industrial and manufacturing engineering. – Ufa: USATU, 2011. Vol 15, No. 4 (44). P. 175-180. (in Russian).
[12]. Pashinskaya E.G., Tishchenko I.I., Stolyarov V.V., Kralik M.A. Peculiarities of plastic deformation of mild steel under impact loading combined torsion with tension. "Inzhenerna Mechanika. Naukow notatki". - Lutsk: LTU, Vol. 25, part II. 2009.- Pp. 182-189. (in Russian).
[13]. Patent No. 2347633 of the Russian Federation, the IPC 21 to 1/00. A method of obtaining ultrafine-grained semi-finished products by drawing with shift./ G.I. Raab, A.G. Raab, Publ. 27.02.2009. - Bull. No. 6. (in Russian).
[14]. Chukin M.V., Raab, A.G., Semenov V.I., Aslanyan I.R., Raab G.I. The use of full factorial experiment in the process of drawing with shear//Vestnik MGTU im. G.I. Nosova, Vol. 40, No. 4. 2012. P. 33-38. (in Russian).

NANOCOMPOSITE MATERIALS BASED ON THERMOPLASTIC BLENDS FOR THE TECHNOLOGICAL EQUIPMENT WITH A LONG SERVICE LIFE

НАНОКОМПОЗИЦИОННЫЕ МАТЕРИАЛЫ НА ОСНОВЕ СМЕСЕЙ ТЕРМОПЛАСТОВ ДЛЯ КОНСТРУКЦИЙ ТЕХНОЛОГИЧЕСКОГО ОБОРУДОВАНИЯ ПОВЫШЕННОГО РЕСУРСА

Senior lecturer Antonov A.[1], Assoc. Prof. cand. eng. Avdeychik S.[2], Senior lecturer Sarokin V.[3], Prof. Dr. Eng. Struk V.[4], Assoc. Prof. cand. eng. Vorontsov A.[5], Assoc. Prof. cand. eng. Mikhailova L.[6]
Faculty of Innovative Technologies of Mechanical Engineering [1,3,4,5,6] – Yanka Kupala State University of Grodno, Belarus, Molder, ltd [2] – Grodno, Belarus,

Abstract: *The composite materials based on polymer and oligomer blends with different thermodynamic compatibility have been developed. It is shown that for polymer and oligomer blends of products formed as result of the thermogasdynamic synthesis of fluorine-containing compounds, the ability of oligomeric matrix to multiply deformation and alternating transfer is the most important. In polymer-polymer systems formed in a melt by various technologies the most important factor is the structure of the boundary layers determining the parameters of the stress-strain and tribological characteristics of the composites. The effect of physical compatibilization during the introduction of nanoscale metal-containing and carbon-containing particles into the blend compositions has been established. This effect promotes the thermodynamic compatibility and resistance to the action of thermal-oxidative medium on composites.*
KEYWORDS*: NANOCOMPOSITE MATERIALS, BLENDS, COMBINATION, STRUCTURE*

1. Introduction

In the nomenclature of functional polymer composite materials the important place have polymer and oligomer blends. The combination of a binding agent (matrix) with a polymer or oligomer modifier leads to required performance parameters achievement that can provide a given resource of products in specific application conditions [1 – 4]. The most significant problem of achieving stable parameters of the structural characteristics of polymer blends determining the load-speed and temperature range of application of products in static and dynamic designs of units and aggregates with various functionalities is overcoming the thermodynamic incompatibility of polymer and oligomer components. The thermodynamic incompatibility is due to the features of the composition, structure of the macromolecule, difference in the rheological, thermophysical and other characteristics.

In this regard, it is reasonable to investigate scientific approaches to formation of polymer blends with given performance characteristics by means of increasing thermodynamic compatibility using the nanostate phenomenon. Therefore, physicochemical and structural transformations during combination of polymer and oligomer components with close molecular structure and using nanoscale functional modifiers with various formula and structure have significant scientific and practical interest.

2. Research methods

The interphase processes in systems obtained by combining thermoplastic polymer and oligomer components under various technology impact, physicochemical and tribochemical transformations during the processing of composites and the using of products from them in metal-polymer constructions with various functionality are considered.

As components of the blend composite materials we used the most common in materials science and technology of polymer materials thermoplastic polymers and oligomers: aliphatic polyamides – PA6, PA6.6, (Grodno Chimvolokno JSC, Belarus) PA66/6 Grilon TSS/4, PA12 Grilamid L20 (EMS-CHEMIE AG, Switzerland), PA11 Rilsan (Arkema, France), polyolefins – polypropylene (PP), low-density polyethylene (LDPE), high-density polyethylene (HDPE) produced by Polymir JSC, Belarus, polyesters – polyethylene terephthalate (PET), polybutylene terephthalate (PBT) primary (Mogilev Chimvolokno JSC, Belarus) and regenerated (Belvtorpolymer JSC, Belarus), polyacetals – copolymer of formaldehyde with dioxolane (POM copolymer), fluorine-containing compounds – polytetrafluoroethylene F-4 and F-4M (Galogen JSC, Russia), fluorinated oligomers "Foleoks" (Federal State Unitary Enterprise "Institute of synthetic rubber", Russia), products of thermogas dynamic synthesis of PTFE under the brand name "Forum" (Institute of chemistry Far East Branch of the Russian Academy of Science, Russia).

For the control of structure and operating characteristics parameters of the composites and products thereof we used the dispersed, including nano-sized particles of carbonaceous – colloidal graphite preparation C-1 (CGP C-1), ultradispersed diamond (UDD), carbon nanotubes (CNT) produced by CJSC "Sinta" and the A. V. Luikov Heat and Mass Transfer Institute of National Academy of Science of Belarus, silicon (clay, tripoli) and metal (copper formate) compounds produced by original technology of manufacturers.

The combination of the components was carried out by extrusion technology using a twin-screw extruder, thermomechanical mixing in the material cylinder of injection molding machine Battenfeld HM series (WittmannBattenfeld GmbH, Germany) and the deposition of particulate matter in fluidized layer on a solid substrate.

The physical and chemical processes at the interface in the blend composites and metal-polymer systems were investigated using modern methods of analyses: IR spectroscopy (Tensor-27), X-ray diffraction (Dron 3.0), differential thermal analysis DTA (Thermoscan 2), atomic force analysis (AFM), scanning electron (SEM) and optical (OM) microscopy using with original equipments (SEM microscope Mira, Tescan, AFM microscope NT-206, metallographic inverted microscope MDS). Energy state of the components was investigated by thermally stimulated currents spectroscopy (TSC-analysis).

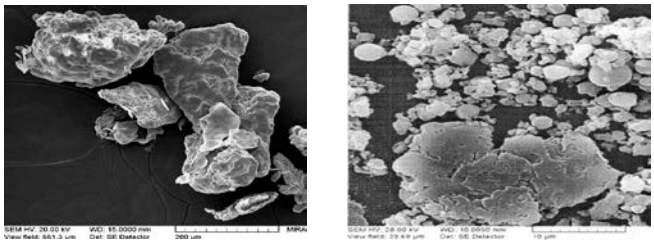
The parameters of stress-strain, tribological, adhesion characteristics of composite materials and coatings was determined by standard techniques on the specialized equipment – tensile-testing machine Z010 Zwick, tribometer FT-2. The rheological parameters of components and blends were examined by melting flow rate meter IIRT-119.

3. Results and discussions

A complex analysis of the composition and structure of the products of the thermogasdynamic synthesis of fluorine-containing compounds, which are produced under the trademark "Forum", have been conducted [5].

Morphological analysis of industrial powder products PTFE F-4 (F-4M) and UPTFE (Forum), conducted by SEM (Fig. 1), indicates the characteristic areas that assume a different structure of particles obtained by thermogasdynamic synthesis (TGD-synthesis).

The developed morphology of PTFE particles is due to the features of synthesis from the gaseous monomers (tetrafluoroethylene) in the presence of polymerization catalysts at certain temperatures and pressures in the reaction volume. The pronounced spherical shape of the particles of UPTFE and their high plastic deformability indicate their polyfraction structure. We made an assumption that the UPTFE have polyfraction structure including oligomer (low-melting) fractions with a melting temperature of 333 – 730 K. The polyfraction structure is due to processes of ablation.



a **b**

Figure 1. – The characteristic morphology of industrial PTFE (F-4) (a) and UPTFE (Forum) particles (b). SEM method

The carried out researches of features of UPTFE structure allowed to offer a model composite system consisting of a set of oligomer fractions and nanoscale polymer particles with different habit – whisker, lamellar, spherical. The adequacy of the proposed model is confirmed by studies of re-deformation and alternating transfer processes during the relative axial displacement of substrates from inert materials (silicate glass). The presence in the UPTFE of oligomer fraction acting as a matrix ensures its fixing and repeated deformation in the microroughness of the substrate and the plasticizing effect of surface layers of the industrial PTFE (F-4 and F-4M) dispersed particles. During the processing such particles by the products of sublimation of UPTFE at temperatures of 473 – 573 K for 0.1 – 0.5 hours or during mixing with UPTFE under mechanochemical activation are formed the facilities for improving of the components compatibility and monolithization at a temperature of 623 – 643 K with the formation of a low-defect structure. The presence of oligomer and polymer components in the modifier promotes the effect of increasing the strength parameters by 1.1 – 1.2 times and the wear resistance by 1.3 – 1.5 times for the industrial polytetrafluoroethylene F-4 and F-4M [5].

Taking into account the variety of the functionality and design of the technological equipment components, shut-off and control valves and automotive components were considered the features of combining components with different potentials to interfacial interaction: aliphatic polyamide blends (PA6, PA6.6, PA66/6, PA11, PA12), polyamide and polyester blends (PET, PBT), primary and regenerated polyolefins and thermoplastic elastomers, fluorine-containing compounds (UPTFE).

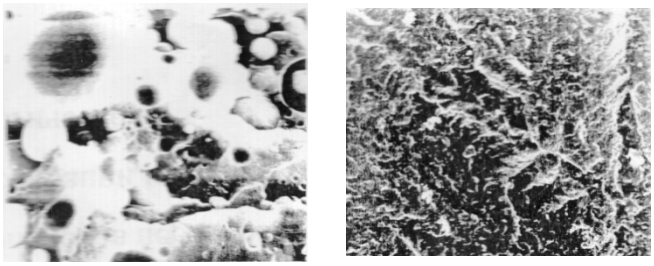
During the thermomechanical combination of polyesters (PET and PBT) and polyamides in the material cylinder of the injection molding machine the heterophase structures with pronounced phase separation are generate due to differences in molecular structure, rheological and thermophysical characteristics. It was found that the introduction into the composite PET (5 – 10 wt. %) and PA6 of 5 – 20 wt. % dispersed particles of layered silicates (mica, talc) contributes to an increase wear resistance by 1.3 to 1.5 times and adhesion strength by 1.2 to 2.4 times of the coatings [6].

The features of the structure and performance characteristics of polymer blends based on components with high thermodynamic compatibility – aliphatic polyamides and polyolefins are investigated [7].

The introduction to the matrix polyamide (PA6, PA6.6, PA66/6) of modifiers (PA12, PA6) allows to realize the advantages of each component of the blends for the attainment of the technically significant effect of increasing the strain-stress characteristics (Table 1). An important feature of polymer blends based on aliphatic polyamides is the high homogeneity of the structure caused by the formation of interphase layers from close-structure macromolecules (Fig. 2).

In contrast to blends with different molecular structure of components (PA6 – PET, PA6 – PBT, PA6 – POM copolymer) the blends of aliphatic polyamides (PA6, PA6.6, PA66/6, PA12) do not have a pronounced interface.

During the introduction to composite material of the nano-sized particles (UDD, CNT, CGP C-1) the values of the Young's modulus (E) parameters are increase from 2207.6 – 2647 MPa to 2797.8 – 2984.7 MPa and tensile strength (σ) from 51.9 – 107.3 MPa to 109.7 – 115.1 MPa. Thermo-mechanically combined polyamides is reasonable to use as binding of structural and tribotechnical materials.



a **b**

Figure 2 – The characteristic morphology of the composite materials: PA6 – POM copolymer (a) and PA6.6 + PA6 (b). Samples are obtained in a liquid nitrogen. Content of components is 50 : 50 wt.%

During combining of polyolefins (PP, HDPE, LDPE) the composites with high phase homogeneity and controlled rheological characteristics are formed. The effect is also to be achieved by using the regenerated components. This effect makes it possible to obtain materials for products with various functionality.

The tribotechnical and protective characteristics of rotaprint coatings based on a fluorine-containing polymer-oligomer blends with a thickness of 5 – 10 μm formed on the components of metal-polymer systems are investigated. It has been established that the presence of an oligomer component in the UPTFE composite coating provides the necessary level of adhesion and the ability to re-deform. These characteristics reduce the intensity of corrosion-mechanical wear. In the friction zone the separating layer with the properties of alternating transport is formed. This layer outperforms and has better anti-wear action than the thin films of fluorine-containing oligomers "Foleoks", metal phosphates and titanium nitride layers.

The effectiveness of the anti-wear action of rotaprint coatings of UPTFE is improved by modifying the composition of 0.01 – 0.1 wt. % nano-sized particles of carbon-containing components that have the function of reinforcement additive. Polymer-oligomer composites based on UPTFE are effective when used as rotaprint coatings for splined joints of cardan shafts and sealing units of shut-off and control valves.

The composite materials based on blends of aliphatic polyamides (PA6, PA6.6, PA12) and (PA6, PA11) have been developed. They are used as structural and tribotechnical materials for friction units of automotive components and technological equipment. The modifying of matrix thermoplastics (PA6.6, PA6) by the thermodynamic compatible components (PA11, PA12) in combination with nanoscale particles provides an increase of strain-stress characteristics. At the same time, the variation of the modifying polyamide content makes it is possible to control the parameters of rheological characteristics and hydrophobicity. An important performance property of the developed construction materials based on polyamide blends is high resistance to the action of thermal-oxidative environment. This property is caused by the action of nanosized particles as a non-chain stabilizer [8].

The developed composite materials based on the regenerated polyolefins (PP, HDPE, LDPE) produced by JSC "Belvtorpolimer" are not inferior to the primary materials (produced by Stavrolen, Ltd) at the parameters of strain-stress characteristics and have higher impact toughness and frost resistance (243 – 233 K).

Table 1 – *Parameters of strain-stress characteristics of composite materials based on aliphatic polyamides*

Materials	E, MPa	σ, MPa	ε, %
PA6	2318,1	65,19	3,8
PA6.6	2647,1	77,70	4,0
PA66/6	2207,6	69,36	4,3
PA12	1226,1	56,35	250
PA6.6(94 wt.%)+PA6(5 wt.%)+PA12(1 wt.%)	2571,1	77,71	4,3
PA6.6(90 wt.%)+PA6(5 wt.%)+PA12(5 wt.%)	2525,2	75,58	5,9
PA6.6(84,5 wt.%)+PA6(10 wt.%)+PA12(5 wt.%)+CGP C-1(0,5 wt.%)	2984,7	78,84	3,9
PA6.6(84,5 wt.%)+PA6(10 wt.%)+PA12(5 wt.%)+CNT(0,5 wt.%)	2797,8	54,19	2,1
PA6.6(84,5 wt.%)+PA6(10 wt.%)+PA12(5 wt.%)+UDD(0,5 wt.%)	2850,5	77,80	3,8

4. Conclusions

The structure and performance characteristics of composite materials based on blends of thermoplastic polymer and oligomer components obtained by various technologies have been studied. The composite materials based on blends of aliphatic polyamides (PA6, PA6.6, PA66/6, PA12, PA11), polyolefins (PP, HDPE, LDPE) and fluorine-containing compounds (UPTFE, PTFE) with high parameters of strain-stress, adhesion, tribotechnical characteristics for the manufacture of products and coatings for technological equipment, automotive components, shut-off and control valves.

The structure and composition features of thermal treatment products of block polytetrafluoroethylene (PTFE) in a protective environment at the temperature range 623 – 673 K have been studied. The presence of oligomer and polymer components in the heat treatment products (UPTFE) forming a polyfraction blend of ablation products and recombination of gaseous fractions of the thermal degradation of the block semifinished product of UPTFE was established by the DTA, IR spectroscopy, AFM and SEM methods. Polymer-oligomer blends of heat-treated products of polytetrafluoroethylene have the ability to repeatedly re-deform without destroying and subliming oligomer fractions. These blends can be used as components for tribotechnical materials and coatings and processing additives for processing of polymer blendes based on thermoplastic primary and regenerated (PA6, PA6.6, PET, PBT, PP, HDPE) matrices.

The features of the structure and parameters of strain-stress and tribological characteristics of the composite materials obtained by technologies of thermomechanical combining in a twin screw extruder, processing in injection molding machine with a screw plasticator and deposition of powdered fractions by the heat treatment at the melting temperatures of granular and powdered thermoplastic components with close structure of the molecular chain – polyamides (PA6, PA6.6, PA66/6, PA12, PA11) and polyolefins (PP, HDPE, LDPE). Using IR spectroscopy, DTA, ACM and SEM methods it was found that in polymer-homologue blends which have a different thermophysical and rheological characteristics in comparison to blends of thermodynamically incompatible polymers (PA6 – PET, PA6 – PBT, PA6 – HDPE) is formed heterophase structure with high homogeneity and strength due to the formation of transition layer with a few defects as a result of the mutual diffusion of macromolecules. Under the modifying of polymer blends by nanoscale particles of carbon and silicon containing compounds (UDD, CGP C-1, CNT) in an amount of 0.001 – 1.0 wt. % the formation of boundary layers is intensified due to the formation of physical adsorption bonds between the macromolecules of the combined components.

The structural and tribotechnical materials based on blends of primary and regenerated thermoplastics of the polyamide (PA6, PA6.6, PA66/6, PA12), polyesters (PET, PBT) and polyolefins (PP, HDPE, LDPE) containing nanosized particles of carbon (CGP C-1, UDD, CNT), silicon (clay, talc, mica), metal-containing (copper) modifiers at doping (0.001 – 1.0 wt. %) concentrations with parameters of deformation-strength characteristics by 1.1 – 1.2 times exceeding the parameters of the matrix thermoplastics have been developed. The developed composites based on polymer blends are effective for manufacturing structural elements for automotive components and metal-polymer belt conveyors used in various industries.

References

1. Berlin, A. A., Volfson, S. A., Enikolopian, N. S., Negmatov, S. S. (1990). Principles of polymer composites. Moscow: Khimiya, 240 p.
2. Kuleznev, V. N. (2013). Polymer blends and alloys. St. Petersburg: Nauchnye osnovy i tekhnologii, 216 p.
3. Ermakov, S. N. (2001). Development of composite materials based on thermoplastics using the method of compatibilization: Synopsis of Candidate (candidate of chemical sciences) dissertation research, Moscow, 16 p.
4. Bogdanovich, S. P. (2006). Tribotechnical composite materials based on compatibility aliphatic polyamide and polyolefin blends: Synopsis of Candidate (candidate of tech sciences) dissertation research, Gomel, 22 p.
5. Struk, V. A., Tsvetnikov, A. K., Antonov, A. S., Avdeychik, S. V., Ovchinnikov, E. V., Gorbatsevich, G. N., Shcherba, V. Ya. (2009). Mechanochemical aspects of technology of fluoroplastic composites formation and application. Proceedings of the National Academy of Sciences of Belarus. Series of physical-technical sciences. Vol. 3, 28 – 33 pp.
6. Antonov, A. S., Kondrashova, G. S., Skaskevich, A. A. (2013). Influence of fillers on the tribotechnical properties of blend compositions based on thermoplastics. Vesnik of Yanka Kupala State University of Grodno. Series 6. Engineering Science. Vol. 4, 36 – 42 pp.
7. Antonov, A. S., Ishchenko, M. V., Burtsev, A. N., Struk, V. A. (2016). Composite materials based on thermoplastic blends. Mining mechanical engineering and machine-building. Vol. 3, 48 – 56 pp.
8. Avdeychik, S. V, Struk, V. A., Sarokin, V. G., Antonov, A. S. (2016). The features of nanodimension realization for polymer matrix composites. Nanomaterials and Nanostructures – XXI Century. T. 7, Vol. 2, 37 – 44 pp.

EFFECT OF HOT PLASTIC DEFORMATION ON DECOMPOSITION OF MAGNESIUM SOLID SOLUTION CONTAINING RARE-EARTH METALS

Prof. Rokhlin L.L., PhD. Lukyanova E.A., PhD. Dobatkina T.V., Korolkova I.G., Ovchinnikova O.A.
Institution of Russian Academy of Sciences A.A. Baikov Institute of Metallurgy and Material Science RAS, Russia

Abstract: *In the work effect of the rare-earth metals (REM) on structure of the decomposed Mg supersaturated solid solution after hot deformation was investigated. Investigation indicated Mg solid solution decomposition during hot deformation with precipitation of the RE-rich particles preferably on the Mg grain boundaries and boundaries between originated blocks. Precipitations on the grain and block boundaries prevent recovery, recrystallization, the grain growth, and increase plasticity of alloys.*
KEYWORDS*: MAGNESIUM ALLOYS, RARE-EARTH METALS, PLASTIC DEFORMATION, SOLID SOLUTION DECOMPOSITION, STRUCTURE.*

1. Introduction

Polycrystalline magnesium and magnesium-based alloys are characterized by low plasticity during plastic deformation at near-room temperatures [1]. This is explained by the fact that the deformation of hexagonal close-packed crystal lattice is realized via sliding along single type of atomic planes, i.e., the basal sliding is realized. Other deformation mechanisms for the magnesium crystal lattice, in particular, twinning and pyramidal-plane sliding, are also possible, but their role is minor. Grain boundaries in magnesium and magnesium solid-solution prevent the development of basal sliding. This results in the fact that the crystal lattice in grain areas adjacent to boundaries becomes substantially more distorted than that of grain body. With increasing deformation temperature plasticity of magnesium and its alloys increases and this phenomenon can be explained by recovery processes and recrystallyzation. In the present study, we report results of investigation of the decomposition effect of the supersaturated magnesium solid solution, containing the rare-earth metals (REMs) on the structure-formation of magnesium solid-solution grains during hot plastic deformation and plasticity.

2. Materials and methods

The studies were performed using pure magnesium and magnesium alloys containing neodymium, yttrium, samarium, gadolinium, and dysprosium, which exhibit the substantial solubility in solid magnesium and a decrease of the solubility with decreasing temperature. The magnesium alloys with the aforementioned REMs are inclined to dispersion hardening [2]. The alloys were prepared by melting and cast then into a metallic mould. The obtained ingots were subjected to hot pressing to form rods 10 mm in diameter (the reduction of area is 90%). Samples were prepared from these rods and subjected to quenching to obtain the supersaturated solid solution. After heat treatment and plastic deformation (which includes the compression and tension), the test portion of samples was cut, and the structure was revealed using chemical polishing in a concentrated nitric acid. Simultaneously, the chemical polishing allows us to reveal the microstructure of samples; thus, the samples were not subjected to additional etching. In some cases, the mechanical polishing and etching in the 0.5% nitric-acid solution in alcohol were performed in order to reveal precipitates during solid solution decompositions. In addition to the optical microscopy, a number of structure investigations were performed using transmission electron microscopy (TEM). The foils for this study were prepared by thinning in 20% nitric acid in ethyl alcohol and rinsed clean ethyl alcohol. A JEM-200A transmission electronic microscope operating at 150 kV was used.

3. Results and discussion

In Fig.1a the structure of the pure magnesium is presented. The sample was previously annealed at high temperature 535ºC so, that the large grains were obtained. In the micrograph only two grains are seen and one of them is rounded by other. The sample was deformed then at room temperature and one can see significant distortion of the crystal lattice in area near the grain boundary, which is more, than the lattice distortions in the grain bodies, as could be expected in according to [3]. With increasing deformation temperature, recovery processes occur first of all within these areas with highly distorted crystal lattice, which are accompanied by the formation of blocks, and the recrystallization starts. In accordance with the more intense deformation near the grain boundaries in these areas the more and smaller blocks can be distinguished (Fig.1b).

The following data on the structure of REM-containing magnesium alloys subjected to hot deformation were obtained. The presence of REMs in the alloys was found to lead to the precipitation of disperse particles from the supersaturated magnesium solid solution, which are located at grain boundaries. As a result, the development of recovery and recrystallization processes within areas adjacent to grain boundaries decelerates. Figures 2a and 2b obtained by TEM demonstrate the decomposition of supersaturated magnesium solid solution at grain boundaries and blocks formed near them. One can see the larger precipitates to be disposed on the grain boundary and the smaller precipitates to be disposed on the block boundaries. In both cases the precipitates detain movement of dislocations and retain by this the grain growth. Optical micrographs in Figures 2c and 2d show the initiation of blocks and recrystallization nuclei at boundaries of the deformed grains remaining them extended form and consisting of the blocks. The subsequent increase in the deformation temperature is accompanied by the development of recrystallization as the small grains mainly along boundaries of initial large partially deformed grains (Fig. 2e). At high deformation temperatures, the recrystallization occurs completely (Fig. 2f). During hot deformation under creeping conditions, the presence of disperse REM-containing particles favors the formation of stepped grain boundaries (Fig. 2g).

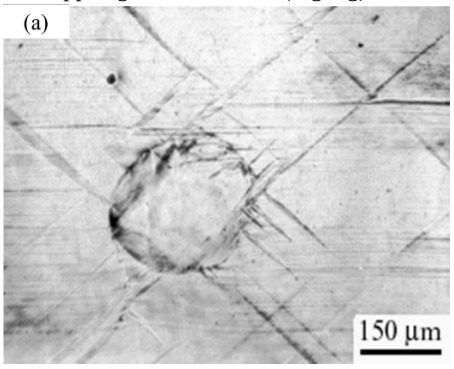


Fig. 1. *Microrelief of magnesium samples subjected annealing at 535ºC and (a) 5% tension at 20°C and (b) 5% tension at 350°C, block-formation.*

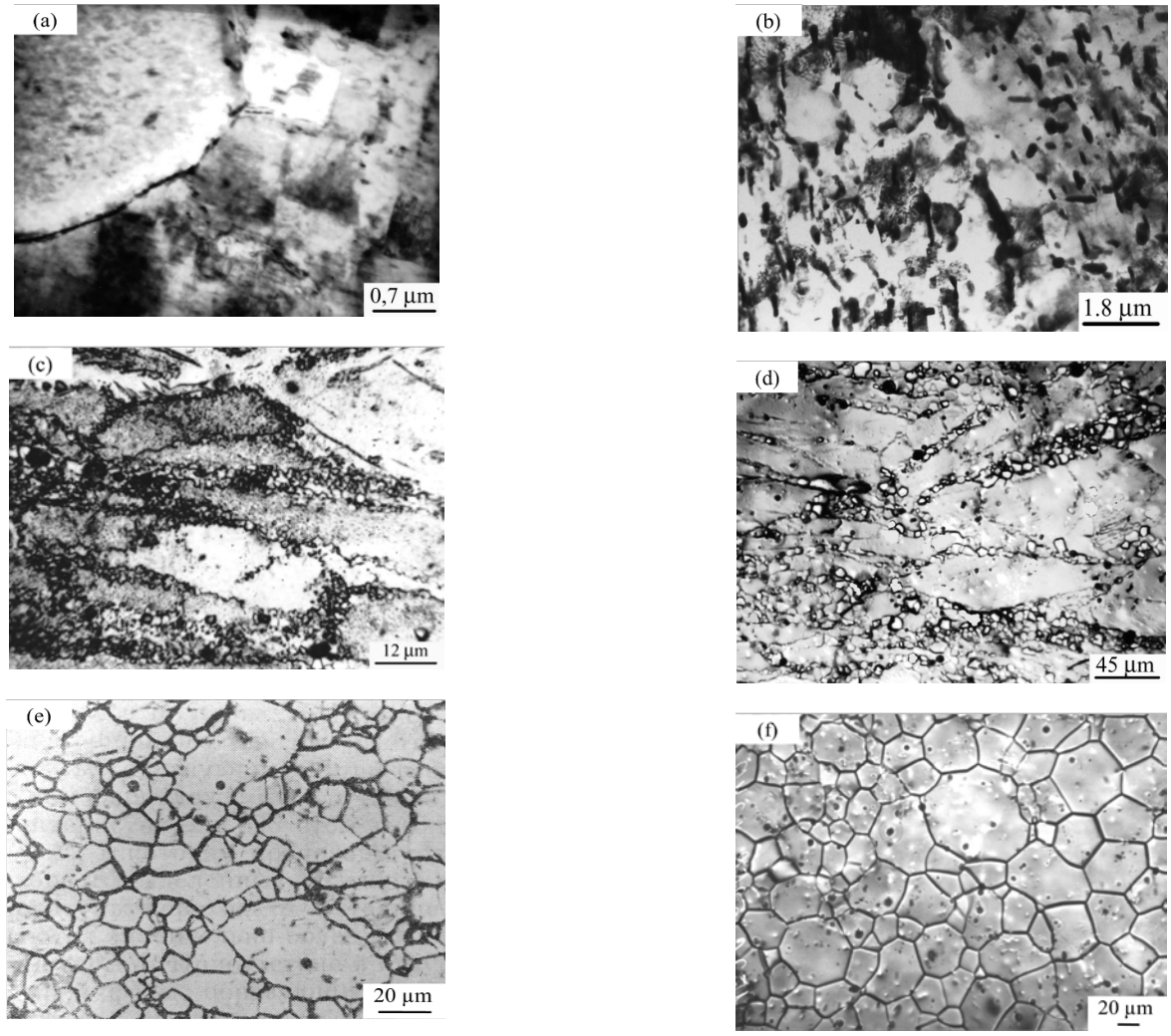


***Fig. 2**. Microstructure of alloys subjected to different treatments: (a) Mg-2.8%Sm, 90% extrusion at 420°C (disperse precipitates at block boundaries, TEM); (b) Mg-5.6%Sm, quenching, 40% upsetting at 450°C (disperse precipitates at block boundaries, TEM); (c) Mg-3.2%Nd, 90% extrusion at 350°C (nuclei of recrystallization at grain boundaries); (d) Mg-6%Gd (quenching, 40% compression at 400°C (onset of recrystallization at grain boundaries); (e) Mg-2.2%Y, compression at 400°C; (f) Mg-11.1%Gd, compression at 450°C; and (g) Mg-3.2%Nd, quenching, creeping at 300°C for ~ 100 h (stepped grain boundaries).*

The deceleration of recovery and recrystallization processes, which takes place owing to the presence of disperse REM-containing particles, favors the increase in the temperature of the onset of failureless deformation of magnesium alloy. This fact can be seen from the table, which indicates the temperature of the onset of failureless deformation of the alloys to increase with increasing REM content in the alloys. This occurs owing to increasing content of particles, which impede the dislocation motion, ensuring the formation of blocks and recrystallization. Thus, we observe the correlation between the temperature of the onset of failureless deformation and the temperature of the onset of recrystallization.

***Table**. Results of compression tests for magnesium and magnesium REM-containing alloys*

REM content, wt %	Temperature of solution treatment before quenching or annealing		Temperature of the onset of failureless deformation, °C	Temperature of the recrystallzation onset, °C
	Operation	Temperature, °C		
-	Annealing	435	150-175	200-250
3.2 Nd	Quenching	500	300-325	400-450
5.6 Sm	Quenching	520	300-325	350-400
11.1 Gd	Quenching	520	300-325	450-500
21.5 Gd	Quenching	520	450-475	450-500
19.1 Dy	Quenching	540	300-325	400-450
12.7 Y	Quenching	550	300-350	400-450

4. Conclusions

1. Hot plastic deformation of magnesium and its alloys is accompanied by substantial crystal-lattice distortion within areas adjacent to grain boundaries.

2. The decomposition of magnesium solid solution during hot deformation leads to the precipitation of disperse REM-containing phase particles on grain boundaries.

3. Disperse REM-containing particles precipitated from the magnesium solid-solution decelerate the recovery and recrystallization processes and, thus, increase the temperature of possible substantial failureless deformation of magnesium alloys.

4. Precipitated disperse REM-containing particles favor the formation of stepped grain boundaries during hot deformation under creeping conditions.

5. References

1. The reference-book on the structural materials / Ed. Arzamasov B.N., Soloveva T.V. -M., MGTU im. N.E.Baumana, 2005, 640s. (in Russian).

2. Rokhlin L.L. Magnesium Alloys Containing Rare-Earth Metals. -London – NewYork, Taylor and Francis, 2003, 245 p.

3. Kaibyshev O.A., Valiev R.Z. The grain boundaries and properties of metals. –M., Metallurgia, 1987, 214 s. (in Russian).

PRODUCTION OF POWDER POROUS MATERIALS FROM MECHANICALLY ACTIVATED ALUMINUM OXIDE

ИЗГОТОВЛЕНИЕ ПОРОШКОВЫХ ПОРИСТЫХ МАТЕРИАЛОВ ИЗ МЕХАНИЧЕСКИ АКТИВИРОВАННОГО ПОРОШКА ОКСИДА АЛЮМИНИЯ

Prof., Dr. Eng., Cor. Member of NAS of Belarus Ilyushchanka A.[1, 2], Cand. Eng., Docent Kusin R.[3], Cand. Eng., Docent Letsko A.I.[2]
Charniak I.[2], Zhehzdryn D.[2], Ilyukevich A.[2]
State research and production powder metallurgy association [1], State Scientific Institution "Powder metallurgy institute"[3], Belarusian state agriculture technical university [3] - Minsk, Republic of Belarus
E-mail: alexil@mail.belpak.by, 19081877@mail.ru, nil23niipm@tut.by, irinacharniak@tut.by, varchavskaia@mail.ru

Abstract *The results of the development of a process for the production of powder porous materials (PPM) based on a granular mechanically activated aluminum oxide powder have been presented. The dynamics of the particle size change of alumina powder depending on the time of mechanical activation by means of a high-energy mill of planetary type has been studied. The development results of permeable materials based on granular mechanically activated oxide ceramic powder have been presented. The developed PPMs are applied for liquid and gas filtration, production of calibration elements for control and measuring devices and equipment.*

KEYWORDS: POWDER POROUS MATERIALS, MECHANICAL ACTIVATION, NANO-SIZED AND ULTRA-DISPERSED POWDERS OF ALUMINUM OXIDE, PROPERTIES

1. Introduction

An important direction of powder metallurgy is the production of porous powder materials (PPM); their efficiency and field of application are determined by the presence of an interconnected pore system. Modern methods of controlling the pore structure in a wide range provide such properties as permeability for liquids and gases, the ability to delay various inclusions, to muffle noise, etc.
In most cases of practical application strict requirements are imposed to porous powder materials on the entire range of properties, primarily to the fineness of filtration and pass-through function [1]. The work quality of the PPM is determined mainly by the fineness of the filtration, which depends on the size of the pores – the smaller they are, the higher the fineness of the filtration. At the same time, the smaller the particles size of the powder from which the filter material is made, the greater the probability of obtaining the material practically impermeable [1]. PPM production technology includes traditional for powder metallurgy operations of charge preparation, molding (with and without pressure) and sintering. The properties of PPM depend on the properties of the initial powders and the technological process for their production. Metal and ceramic powders with particles of various shapes and sizes from nanometers to millimeters are used for their production. Porous materials are produced from powders of bronze, corrosion-resistant steel, titanium, aluminum. Powders of oxides, carbides, silicides and other high-melting compounds are widely used for PPM production.
One of the important directions of porous powder materials is the development of nanomaterials and nanotechnologies. The creation of devices based on oxide ceramics for the filtration of liquids, gases and other purposes is of great interest for research and finds a wide application in various production fields [2-5].
The objective of this work is to develop a process for the production of powder porous materials based on a granular mechanically activated alumina powder.

2. Results and discussions

Mechanical destruction of the powder was carried out in the delivery condition using a high-energy mill of the planetary type "Pulverisette 6" Fritsch (Germany) in order to produce a permeable alumina-based material. When treating powders in high-energy mills, mechanical energy is transferred to the treated substance. As a result, dispergation by milling (particle size reduction) occurs (activation) with a formation of a new surface of particles with a much larger total area per unit mass. The main technological parameters of the mechanical activation of powders affecting the properties of nanosize and ultrafine ceramic powders are the number of rotations of the planetary disk and the treatment time. Mechanical activation of alumina powder was carried out for 10-30 min at the speed of rotation of the planetary disc 550 min^{-1}. The surface morphology of the experimental powder samples was examined on a high-resolution scanning electron microscope "Mira" of "Tescan" company (Czech Republic). The research equipment is shown in Figure 1.



Fig. 1 *Scanning electron microscope of high resolution "Mira-3" of "Tescan" company (Czech Republic)*

Figure 2 shows the images of alumina powder particles in the delivery condition prior to mechanical destruction.
It should be noted that Al_2O_3 powder after milling is characterized by a high tendency to agglomeration and has a complex multilevel structure. Primary ultradispersed and nano-sized particles are combined into agglomerates with the size from 0.5 to several micrometers; it is possible to separate individual nano-sized grains (particles) in their structure.

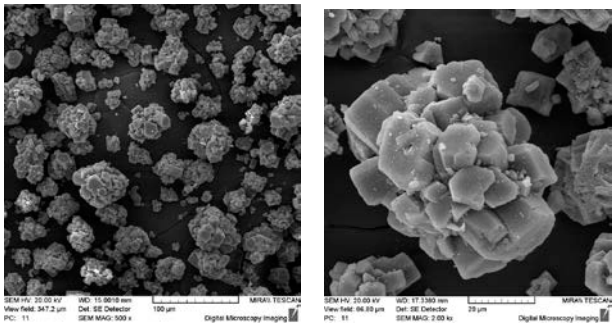
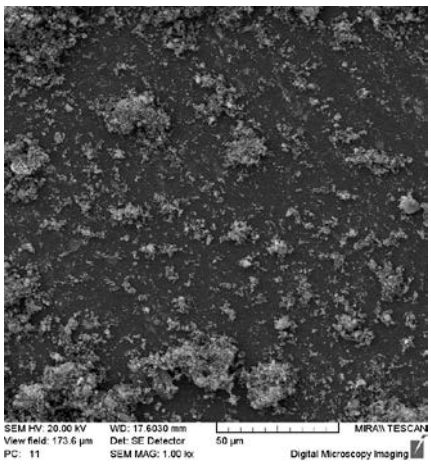
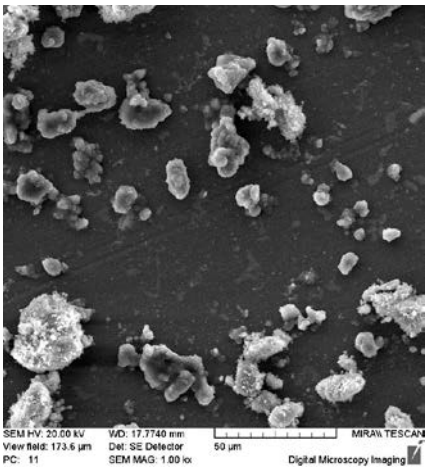


Fig. 2 *Morphology of the surface of alumina powder particles (Al_2O_3), × 500 prior to mechanical destruction*

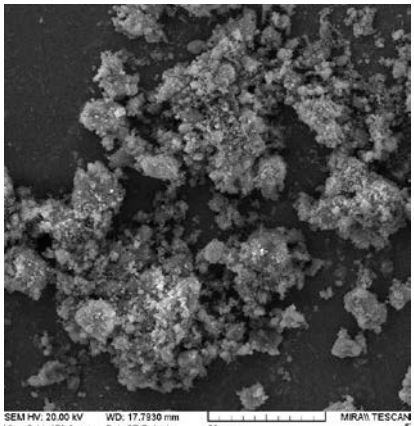
These agglomerates, in turn, are combined into larger (from 10 to 100 μm) secondary aggregates and agglomerates. Considering the difficulty in determining the real particle size of the agglomerate type, and also the fact that it is not possible to completely separate all individual particles during the dispersion process, the size of the primary particles and the maximum (typical) size of the agglomerates was used for comparative assessment visually defined from the SEM micrographs of the powder (Figure 3).



a)



b)



c)

Fig. 3 *Dynamics of the particle size change of aluminum oxide powder depending on the milling time: a) 10 min.; b) 20 min.; c) 30 min., ×1000*

Quantitative stereological analysis of powder samples after mechanical destruction was carried out with the help of the software complex of image processing and analysis "Autoscan". The particle size distribution of the powders is shown in Figure 4.

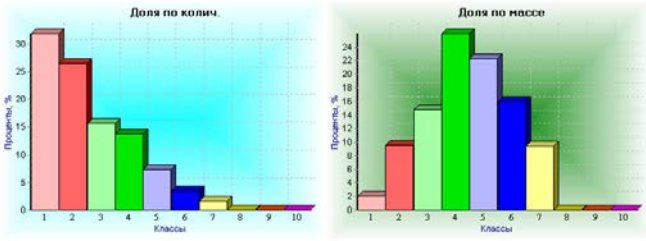


Fig. 4 *Particle size distribution in Al_2O_3 powder after mechanical destruction in a planetary mill for 20 min.: 1 – (0-1,2) μm; 2– (1,2-2,4) μm; 3 – (2,4-3,6) μm; 4 – (3,6-4,8) μm; 5- (4,8-6) μm; 6 – (6-7,2) μm; 7– (7,2-8,4) μm; 8 – (8,4-9,6) μm; 9 – (9,6-10,8) μm; 10 – (10,8-12) μm*

As can be seen from the histogram of the particle size distribution after mechanical activation of the alumina powder, the presence of particles smaller than one micron is 30%.

Mechanically activated aluminum powders were used to produce permeable materials. The technology of PPM production included the following stages: mechanical activation of the powder, charge preparation, pressing, sintering. Mechanical activation of aluminum oxide powder particles was carried out using a high-energy planetary-type mill "Pulverisette 6" of Fritsch company (Germany) for 30 minutes with a rotation speed of 520 min^{-1} of a planetary disk. The particle size of the milled alumina powder was from 50 to 200 nm. The prepared sample weight of aluminum powder was mixed with a 5% solution of polyvinyl alcohol. The obtained mass was dried in a drying cabinet CHBC 4,5.4.5/34-1 at a temperature of 80 °C at constant stirringThe formation of tubular filter materials with a diameter of 12-60 mm and a length of 50-500 mm was carried out by radial isostatic pressing on the isostat ИСПР И1. Sintering of porous materials was carried out in a laboratory oven Netzsch 1700 in air at 1350 °C for one hour.

The samples of permeable materials based on a granular mechanically activated alumina powder are shown in Figure 5.



Fig. 5 *The samples of permeable materials based on a granular mechanically activated alumina powder*

A liquid pollutant (model solution) was used to determine the retention capacity of the developed material. Fertilizer of "HUMO+" was used as a pollutant. The permeable material was placed in a special tooling and sealed. The test liquid pumped by the air source was passed through the permeable material into the tank for filtrate collecting. The filtrate sample was taken and examined for fineness of purification using Laser Diffraction Particle Size Distribution Analyzer Malvern Mastersizer 2000 with an automatic dispersion and delivery module of the HydroS sample. The particle size measuring range of the Laser Diffraction Particle Size Distribution Analyzer Malvern Mastersizer 2000 is 0,02-2000 μm. The fineness of the purification was determined as the maximum particle size found in the filtrate. The device for determining the fineness of purification is shown in Figure 6.



Fig. 6 *Laser Diffraction Particle Size Distribution Analyzer Malvern Mastersizer 2000 with an automatic dispersion and delivery module of the HydroS sample for determining the fineness of purification*

The histogram and diagram of particle size distribution illustrate that the filtrate contains particles ranging in size from 0,02 to 0,3 μm (Figures 7 and 8).

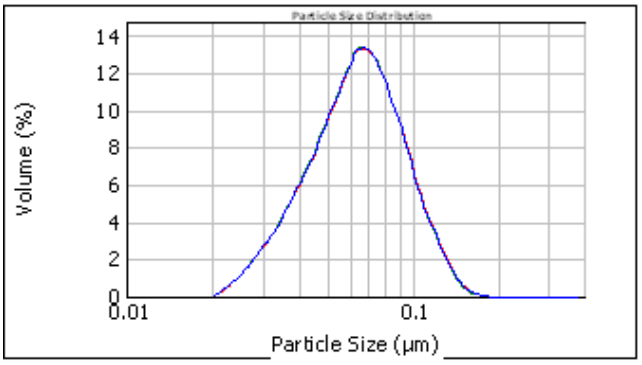


Fig. 7 *The histogram of the particle size distribution contained in the filtrate*

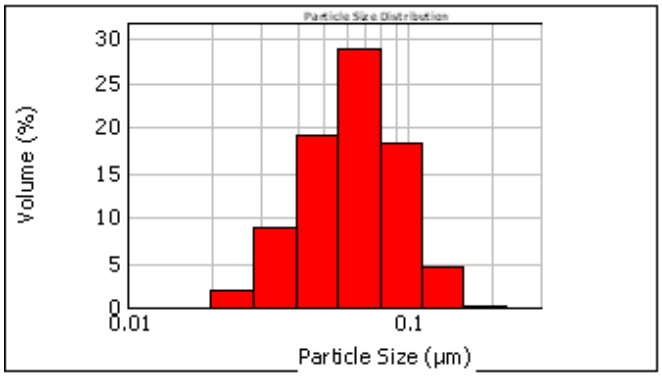


Fig. 8 *Particle size distribution diagram*

The pore size was determined in accordance with GOST 26849-86 by the method of liquid displacement (ethyl alcohol) from the pores; the permeability coefficient is according to GOST 25283-93.
An analysis of the tests has showed that the permeable material based on a mechanically activated alumina powder has an average pore size from 0,55 to 0,8 μm; a permeability coefficient is $(0,55\text{-}0,75)\times10^{-13}$ m^2, and a particle size range contained in the filtrate is 0,02-0,3 μm.

3. Conclusion

The development results of permeable materials based on mechanically activated aluminum oxide powder have been presented. The dynamics of the particle size change of powders depending on the time of milling has been studied. The analysis of the tests showed that the permeable material based on a mechanically activated powder based on aluminum oxide has an average pore size of 0,5-0,9 μm; a permeability coefficient is $(0,55\text{-}0,85)\times10^{-13}$ m^2. Permeable porous materials based on alumina can be produced in the form of a pipe, a disk, a cylinder, depending on the requirements of the design and are used for filtering liquids and gases, for calibration elements of control and measuring devices and equipment.

References

1 Vityaz, P.A. Filtering materials: properties, applications, manufacturing technology [Text] / P.A. Vityaz, V.M. Kaptsevich, R.A. Kusin / Research Institute of PM with Pilot Production – Minsk. – 1999 – P. 304.
2 Azarov, S.M. Porous aluminosilicate ceramics [Text] / S.M. Azarov, Ya.Ya. Piatsiushyk, T.A. Azarova, A.I. Ratko, O.P. Reut, D.V. Makarchuk. – Minsk: Kovcheg, 2009 – 258 p.
3 Azarov, S.M. Problems of production of effective porous materials from aluminosilicate and silicate raw materials [Text] / S.M. Azarov, Ya.Ya. Piatsiushyk, T.A. Azarova // Powder Metallurgy: Rep. collection of scientific papers / Editorial staff: P.A. Vityaz [and others]. – Minsk, 2013. – Issue. 36. – P. 98-104.
4 Sokol, V.A. Peculiarities of the use of porous aluminum oxides [Text] / V.A. Sokol, V.A. Yakovtseva, D.L. Shimanovich / Reports of BSUIR / Minsk, BSUIR, 2012. – No. 2 (64). – P. 21-27.
5 Grigoriev, M.V. Investigation of the mechanical properties of corundum ceramics with varying porosity and crystallite sizes [Text] / M.V. Grigoriev, S.N. Kulkov / Journal of Sibirian Federal University. Engineering & Technologies / - 2011. – No. 4 . – P. 113-120.

EFFECT OF OXYGEN AND NITROGEN CONTENTS ON THE STRUCTURE OF THE Ti-6Al-4V ALLOY MANUFACTURED BY SELECTIVE LASER MELTING

ВЛИЯНИЕ КИСЛОРОДА И АЗОТА НА СТРУКТУРУ СПЛАВА Ti-6AL-4V, ПОЛУЧЕННОГО МЕТОДОМ СЕЛЕКТИВНОГО ЛАЗЕРНОГО СПЛАВЛЕНИЯ

Prof. Kazantseva N. Dr.of Sci.[1], Prof. Krakhmalev P. PhD.[2], Yadroitsev I. PhD.[3], Fefelov A. PhD.[4], Merkushev A. [4], Ilyinikh M. [4], Vinogradova N. PhD. [1], Ezhov I. PhD Student [1], Kurennykh T. PhD. [1]
Institute of Metal Physics, Ekaterinburg, Russia[1]
Karlstad University, SE-651 88, Karlstad, Sweden [2]
Central University of Technology, Free State, Department of Mechanical and Mechatronic Engineering, Private Bag X20539, Bloemfontein 9300, South Africa[3]
Regional Engineering Center of laser and additive technology, Ekaterinburg, Russia[4]
kazantseva-11@mail.ru

Abstract: *TiAl6V (ELI) has the low density, low elastic modulus and high strength. Biocompatibility of this material allows one to adapt it to human implant production and successfully use in the manufacture of surgical implants. Spherical argon-atomized Ti6Al4V (ELI) (45 μm) powder from TLS Technik was used for study. The chemical composition complies with the ASTM F-136 (grade 5), ASTM B348 (grade 23) standard for surgical implant applications. Two machines from two scientific centers (Russia and South Africa) were used for the manufacturing of the alloys. Analysis of the oxygen and nitrogen contamination in SLM alloys was done with Van de Graaff accelerator with 2 Mega Volts. It is found that the oxygen concentration in both samples is about 0.2 wt. % and decreases with the increasing of the sample depth; the nitrogen concentration is about 0,02 wt%. X-Ray results show an absence of beta (BCC) phase in both samples. TEM studies found the metastable martensitic structure and silicon nitride Si3N4.*

KEYWORDS: TITANIUM ALLOY, SLM, 3D PRINTING, MICROSTRUCTURE, OXYGEN, NITROGEN

1. Introduction

Oxidation is a central problem in manufacturing of the titanium alloys [1]. Oxygen and nitrogen are strong alpha stabilizers in titanium Ti6Al4V alloys and effect on the rate of martensitic $\beta \rightarrow \alpha'$ transformation [2]. Oxygen enriching layer with hard alpha phase is generated by oxidation process. The depth of the alpha case layer in the titanium Ti6Al4V ingots may achieve up to 250 μm [3]. The prevention of alpha case forming is important metallurgical problem. Contents of nitrogen and oxygen effect on the lattice expansion of Ti–6Al–4V alloys [4]. In [5] was demonstrated that these interstitial elements increased the strength and hardness with increasing concentrations and decreased the ductility of the alloys. Nitrogen having the greatest effect followed by oxygen and carbon [5].

Additive technology is a novel surface engineering technique, which allows us to obtained alloys with high density (about 99.9%) as cast materials [6]. However, increase in the initial oxygen content in the powder led to higher porosity in the 3D manufactured components [7].

The main purpose of this work is to study the effect of the oxygen and nitrogen contents on the structure of the Ti-6Al-4V alloys manufactured by the selective laser melting.

2. Experimental

Spherical argon-atomized Ti6Al4V (ELI) (45 μm) powder from TLS Technik was used for study. The chemical composition complies with the ASTM F136 (Grade 5) standard and ASTM B348 (Grade 23) for surgical implant applications. The difference between Ti6Al4V ELI (grade 23) and Ti6Al4V (grade 5) is the reduction of oxygen content to 0.13 % (maximum) in grade 23. Nitrogen content in grade 5 (ELI) is less than 0.05 % and in grade 23 is less than 0.03 %. Two machines from two scientific centers (Russia and South Africa) were used for the manufacturing of the alloys. Horizontal samples were produced by the EOSINT M280 machines (EOS GmbH) equipped with an Ytterbium fiber laser operating at 1075 nm wavelength (IPG Photonics Corp.). The laser beam had a TEM00 Gaussian profile and 80 μm spot diameter. In accordance with standard process parameters for a Ti6Al4V alloy, a powder layer thickness of 30 μm, and a back-and-forth scanning by strips with the hatch distance of 100 μm was applied. The substrate and powder material was similar in chemical composition. Argon was used as the protective atmosphere; the oxygen level in the chamber was 0.07–0.12%. Method of nuclear microanalysis was used to determine the oxygen concentration. Van de Graaff accelerator with 2 Mega Volts was used. The beam diameter was 1 mm. Transmission electron microscopy (TEM) was done with JEM 200CX microscope in the Centre of collective use of the Institute of Metal Physics. X-ray diffractometer DRON-3 with Cu kα radiation was used for study.

3. Results and Discussion

We did not found the beta phase lines in the diffraction patterns of both samples. The diffraction lines of HCP alpha phase and a weak diffraction line in the position of the strongest diffraction line of the orthorhombic martensitic α′′-phase were found in X-ray diffractograms of both samples.

Figures 1-2 shows the results of the nuclear microanalysis of the surface studying of the samples. Increasing of the oxygen concentration in the surface layer (0.5 μm) is connected with the preparation of the samples (polishing). One can see that oxygen concentration in both samples is about 0.2 wt. % and decreases with the increasing of the depth from the surface of the sample (Fig.1).

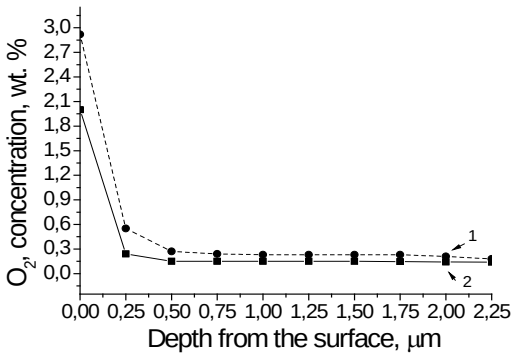


Fig.1 *Oxygen concentration in the samples obtained by nuclear microanalysis: 1- grade 23; 2- grade 5*

Unlike oxygen behavior, nitrogen concentration increases with the increasing the depth from the surface (Fig.2). The same behavior was found for bulk Ti-6Al-4V samples, where authors studied the dependence of the oxygen and nitrogen concentration on the specimen thicknesses at 1000°C [8].

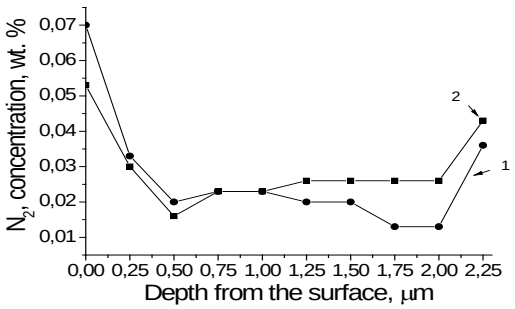


Fig.2 *Nitrogen concentration in the samples obtained by nuclear microanalysis: 1- grade 23; 2- grade 5*

The diffusivity of oxygen being greater than nitrogen and a thick layer of TiO_2, not TiN, forms on the surface, because of the lower diffusion rate of nitrogen in titanium [9]. Titanium nitrides are formed when nitrogen is absorbed from the nitrogen-enriched atmospheres [10]. It was shown also that titanium nitride is the most suitable to protect the surface of medical implants [11].

In our case, the nitrogen and oxygen concentrations of both samples are within the normal range for medical grade alloys.

TEM studies of both samples showed the martensitic structure without any β precipitations (Fig.3).

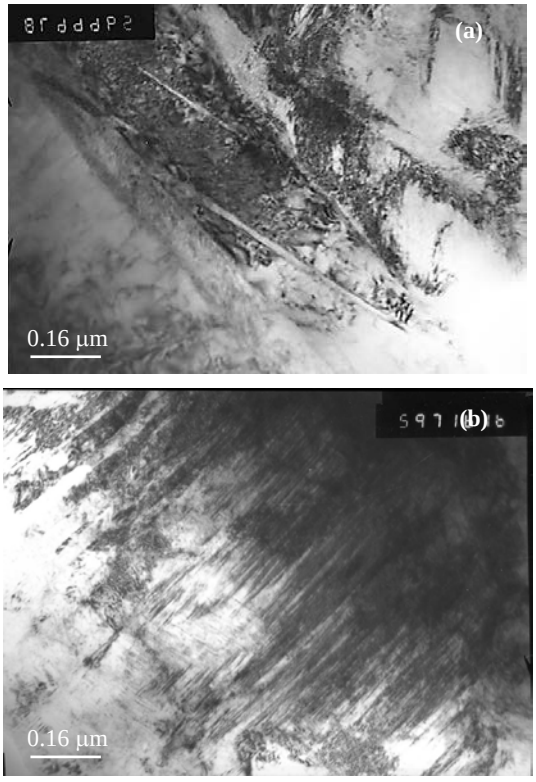


Fig.3 *TEM structure of the SLM samples: a- grade 5; b- grade 23*

Thin precipitations of silicon nitride Si_3N_4 were found in the sample 1 (grade 5), (Fig.4). These precipitations look like thin needles may be seen inside the HCP region. The morphology of the precipitations is typical for silicon nitride Si_3N_4 [12]. The Si_3N_4 regions are very small and rare in occurence. Because, we suppose that the silicon contamination may be remained from the powder.

Small silicon conten in the titanium alloys may be retained from its manufactoring, because silicon is contained in titanium ore such as sphene ($CaTi\text{-}SiO_5$). Rutile (TiO_2) also contains hundredths of a percent of silicon, leucoxene ($Fe_2O_3 \cdot nTiO_2$) may contain up to 10% of silicon as impurities. Generally, silicon in titanium alloys is favoral element. Special adding of silicon in titanium alloys gives a good biocompatibility. Silicon in titanium alloys acts as beta stabilizer, suppresses the formation of the ω-phase and promotes decrease the elastic modulus [13].

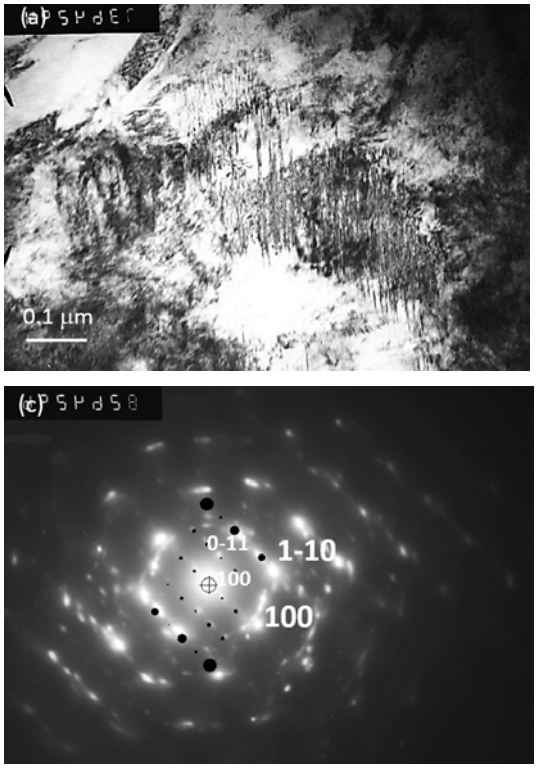


Fig.4 HCP area with silicon nitride Si_3N_4: a- the bright-field image; b- SAED patterns to (a), zone axis $[011]Si_3N_4//[001]hcp$

4. Conclusion

The effect oxygen and nitrogen concentrations on microstructure in two different SLM Ti6Al4V samples (grade 5 and grade 23) was investigated in this study. Structures of the samples manufactured with two different machines used the same regimes are found to be close to each other. It was found that the oxygen and nitrogen contents in both samples are within the normal range for medical grade.

Acknowledgments

This work is based on the research supported by the South African Research Chairs Initiative of the Department of Science and Technology and National Research Foundation of South Africa (Grant №97994), the Collaborative Program in Additive Manufacturing (Contract №CSIR-NLC-CPAM-15-MOA-CUT-01), and Russian Fund of Basic Research No 17-03-00084.

References

1. D. Poquillon, C. Armand, J. Huez, Oxidation and Oxygen Diffusion in Ti–6al–4V Alloy: Improving Measurements During Sims Analysis by Rotating the Sample, Oxid Met. 79 (2013) 249–259.
2. H. Miura, Y. Itoh, T. Ueamtsu, K. Sato, The influence of density and oxygen content on the mechanical properties of injection molded Ti-6Al-4V alloys, Advances in Powder Metallurgy and Particulate Materials.1 (2010) 46-53.

3. A.M. Bauristhene, K. Mutombo, W.E. Stumpf, Alpha case formation mechanism in Ti-6Al-4V alloy investment castings using YFSZ shell moulds, Journal of the Southern African Institute of Mining and Metallurgy. 113 (2013) 357-361.
4. R. Montanaria, G. Costanza, M.E. Tata , C. Testani "Lattice expansion of Ti–6Al–4V by nitrogen and oxygen absorption", *Materials characterization*, Vol.59, pp.334 – 337, 2008.
5. W.L.Finlay and J.A.Snyder, "Effects of three interstitial solutes (Nitrogen, Oxygen and Carbon) on the mechanical properties of high-purity alpha titanium", *Journal of Metals*, Vol.188, pp. 277-286, 1950.
6. P. Krakhmalev, G. Fredricsson, I.Yadroitseva, N. Kazantseva, A. Du Plessis, I.Yadroitsev, "Deformation Behavior and Microstructure of Ti6Al4V Manufactured by SLM", *Physics Procedia*, vol. 83, pp. 778 – 788, 2016.
7. Austin T. Sutton, Caitlin S. Kriewall, Ming C. Leu and Joseph W. Newkirk "Powder characterisation techniques and effects of powder characteristics on part properties in powder-bed fusion processes", *Virtual and physical prototyping*, Vol. 12, No. 1, pp.3–29, 2017.
8. Moorhouse B. Controlling the interstitial element concentration in Ti-6Al-4V using calciothermic reduction, Thesis (PhD), Imperial College London, 2013.
9. Aaron P. Broumas, Nick M. Degnan, Michael L. Meier, "*Oxygen diffusion into titanium*", Department of Chemical Engineering and Materials Science University of California, Davis , 2002.
10. J. R. Cuthill, W. D. Hayes, and R. E. Seebold "Nitriding Phenomena in Titanium and the 6Al-4V Titanium Alloy", *Journal of research of the National Bureau of Standards-A. Physics and Chemisry*, Vol. 64A, No. 1, pp.119-125, 1960.
11. I. M. Pohrelyuk, O. V. Tkachuk, and R. V. Proskurnyak "Corrosion Behaviour of Ti-6Al-4V Alloy with Nitride Coatings in Simulated Body Fluids at 36°C and 40°C", *Hindawi Publishing Corporation ISRN Corrosion*, Vol. 2013, pp.1-7, 2012.
12. Bin Li, Jun-hong Chen, Jin-dong Su, Ming-wei Yan, Jia-lin Sun, and Yong Li Э "Morphology of α-Si3N4 in Fe–Si3N4 prepared via flash combustion", *International Journal of Minerals, Metallurgy and Materials*, Vol. 22, No 12, pp.1322-1327, 2015.
13. Kim Han-Sol, Kim Won-Yong, Lim Sung-Hwan, "Microstructure and elastic modulus of Ti—Nb—Si ternary alloys for biomedical applications" *Scripta Mater.*, Vol. 54, No. 5. Pp. 887—891, 2006.

ELASTIC PHASE TRANSITION IN METALS: THE PRESSURE EFFECT

ДЕФОРМАЦИОННЫЕ ФАЗОВЫЕ ПЕРЕХОДЫ В МЕТАЛЛАХ: ЭФФЕКТ ДАВЛЕНИЯ

Dr. Krasilnikov O.M.[1], Prof, Dr. Vekilov Yu.Kh[1,2], PhD Lugovskoy A.V.[2], PhD Belov M.P.[2]

[1] Department of Theoretical Physics and Quantum Technologies, [2] Material Modeling and Development Laboratory - National University of Science and Technology "MISIS", Leninskiy prosp. 4, 119049, Moscow.
e-mail: omkras@mail.ru

Abstract: *At high pressures (the pressure is comparable with the bulk modulus) the crystalline lattice may become unstable relative to the uniform shear deformations, and as a result the low symmetric crystalline structures will appear (the so called "elastic phase transitions"). The order parameters at these transitions are the components of the finite deformations tensor. The stability of the high-pressure phases is defined by the nonlinear elasticity of the lattice (the third, fourth etc. order elastic constants). Here the different cases of stability loss at hydrostatic pressure of the cubic and hexagonal structures are considered. The relation between the second, third and fourth order elastic constants is given, which defines the possibility of the first order deformation phase transition. The jump of the order parameter and the height of the potential barrier are defined by the third and fourth order elastic constants. As an example, the experimentally observed elastic phase transition in vanadium at P≈ 69 GPa from bcc to the rhombohedral phase is analyzed, and the possible structural transitions in bcc Mo and W at P≥700 GPa are considered. The stability of the Ru in the pressure interval 0÷600 GPa is also analyzed. The necessary values of the different order elastic constants for Mo, W and Ru are calculated in the framework of the density functional theory using VASP (Vienna Ab initio Simulation Package).*

1.Intoduction

The experimental data show that in metals at the pressures usually the phase transitions in the closed packed structure take place [1]. But the high pressure phases (the pressure is comparable with the bulk modulus) frequently become less symmetrical, with a lower packing density [2]. It is occured because with the pressure increasing the crystalline lattice becomes unstable relative to the small uniform shear deformations. As a result, the phase transition takes place in the spontaneously deformed state with a lower symmetry. Almost the all phase transitions in solids are accompanied by the elastic deformations. In most cases, the deformation is not the order parameter, and is connected with it only by the striction interaction. In our case the deformation is the order parameter, and such transitions were called "the elastic phase transitions". At these transitions the number of atoms in the unit cell is conserved, the point group symmetry of the new phase is subgroup of the point group of the parent structure, the translation symmetry is conserved. The critical phenomena at the elastic phase transitions are suppressed [3], and the Landau theory of the phase transitions can be used with the finite deformation tensor components as the order parameters.

2.Lattice stability and the elastic phase transitions.

According to the Landau theory of the phase transitions, the thermodynamical potential can be decomposed in to power series over the order parameter components. The Gibbs free energy *G* is the thermodynamic potential at given *T* and *P*. The structural transitions are accompanied by small, but finite deformations of the crystalline lattice, for taking into account the nonlinear effects it is convenient to choose the finite strain tensor components η_{ij} as the order parameters. Decompose *G* near the equilibrium state at given *T* and *P* over η_{ij} (Lagrangian strain tensor). Let us the spontaneous deformations η_{ij} are isothermal. Then, the change $\Delta G = G(P,T,\eta) - G(P,T,0)$ on the unit volume will be

$$\Delta G / V_0 = (1/2)\tilde{C}_{ijkl}\eta_{ij}\eta_{kl} + (1/6)\tilde{C}_{ijklmn}\eta_{ij}\eta_{kl}\eta_{mn} + (1/24)\tilde{C}_{ijklmnpq}\eta_{ij}\eta_{kl}\eta_{mn}\eta_{pq} + \ldots \quad (1)$$

(the summation is from 1 to 3). In the expression (1) the linear contribution is absent because the system is in equilibrium state. Here

$$\tilde{C}_{ijkl....} = (1/V_0)(\partial^n G / \partial\eta_{ij}\partial\eta_{kl})_0 \quad (2)$$

are the *n*-order isothermal effective elastic constants (EC) (n =2, 3, 4) at the given load and temperature *T*, which characterize the elastic properties of a loaded crystal [4]. In the absence of a load, $\tilde{C}_{ijkl..}$ coincide with the usual elastic constants $C_{ijkl..}$. The all equations of the elasticity theory with $\tilde{C}_{ijkl..}$ are the same as with the load as in the unloaded state. In particular, the stability conditions coincide with the Born conditions for unloaded crystal.

At the given *T* and *P* the system state will be stable if the quadratic form in (1) will be positively defined. As a result, for the usual *bcc*, *fcc* and *hcp* metallic structures we obtain the following stability conditions of relatively uniform shear deformation. For cubical symmetry are:

$$\tilde{C}_{11} - \tilde{C}_{12} > 0 \text{ (a)}; \quad \tilde{C}_{44} > 0 \text{ (b)} \quad (3)$$

For *hcp* structure they are following:

$$\tilde{C}_{11} - \tilde{C}_{12} > 0, \text{ (a)}; \quad \tilde{C}_{44} > 0, \text{ (b)}; \quad \tilde{C}_{66} = (\tilde{C}_{11} - \tilde{C}_{12})/2 > 0 \text{ (c)}. \quad (4)$$

Here $\tilde{C}_{\alpha\beta}$ are the second order effective elastic constants in Voigt notation.

With the pressure and temperature changes these conditions may be distorted, and as a result the structural transition will take place in spontaneously deformed state, which stability is defined by the nonlinear elasticity of the material (by anharmonic contributions of the third, fourth ets. order). In Table 1 the different cases of spontaneous deformation are given, when the lattice instability of crystals with the cubical and hexagonal symmetry is possible. In the present cases the decomposition of the thermodynamic potential (1) is following:

$$\Delta G(P,\eta,T)/V_0 = (1/2)q\eta^2 + (1/3)v\eta^3 + (1/4)w\eta^4 + \ldots. \quad (5)$$

The values of q, v и w are given in Table 1, where $\tilde{C}_{\alpha\beta..}$ are the isothermal elastic constants at the pressure *P*.

Table 1. *Elastic phase transitions under pressure in crystals with cubical (1, 2, 3) and hexagonal (4, 5, 6) structures*

№	Spontaneous deformation	q	v	w	The change of symmetry after transition
1	$-\eta_{11}=-\eta_{22}=$ $=0.5\eta_{33}=\eta$	$6(\tilde{C}_{11}-\tilde{C}_{12})$	$3(\tilde{C}_{111}-3\tilde{C}_{112}+$ $+2\tilde{C}_{123})$	$3(\tilde{C}_{1111}-4\tilde{C}_{1112}+$ $+3\tilde{C}_{1122})$	$\Gamma_c\to\Gamma_q$ $\Gamma_c^f,\Gamma_c^v\to\Gamma_q^v$
2	$\eta_{11}=-\eta_{22}=\eta$	$2(\tilde{C}_{11}-\tilde{C}_{12})$	$v\eta^3=0$ [1)]	$(\tilde{C}_{1111}-4\tilde{C}_{1112}+$ $+3\tilde{C}_{1122})/3$	$\Gamma_c\to\Gamma_0$ $\Gamma_c^f,\Gamma_c^v\to\Gamma_0^v$
3	$\eta_{12}=\eta_{13}=$ $=\eta_{23}=\eta/2$	$3\tilde{C}_{44}$	$3\tilde{C}_{456}$	$(\tilde{C}_{4444}+6\tilde{C}_{4455})/2$	$\Gamma_c,\Gamma_c^f,\Gamma_c^v\to$ Γ_{rh}
4	$\eta_{11}=-\eta_{22}=\eta$	$\tilde{C}_{11}-\tilde{C}_{12}$	$2(\tilde{C}_{111}-\tilde{C}_{222})/3$	$2\tilde{C}_{6666}/3$	$\Gamma_h\to\Gamma_o^b$
5	$\eta_{23}(\eta_{13})=\eta$	$\tilde{C}_{44}$	0	$2\tilde{C}_{4444}/3$	$\Gamma_h\to\Gamma_m$
6	$\eta_{12}=\eta$	$\tilde{C}_{11}-\tilde{C}_{12}$	0	$2\tilde{C}_{6666}/3$	$\Gamma_h\to\Gamma_o^b$

1) due to the deformation symmetry

Here also the possible variants of the structural transitions in *bcc*, *fcc* and *hcp* lattices due to the stability loss relative to the shear deformations are given, which were obtained by the theoretical group analyses of the Brave lattices symmetry. If the third order contribution in (5) is equal zero (cases 2, 5 and 6), then the second order phase transition can take place when the appropriate stability condition is distorted.

$$f(a,x)=a\cdot\frac{x^2}{2}-\frac{x^3}{3}+\frac{x^4}{4}, \quad (6)$$

where $f(a,x)=\Delta G/(V_0G_0)$, $x=(w/v)\eta$, $a=qw/v^2$ (7)

The coefficient a takes into account the 2, 3 and 4 order ECs changes with *P* and *T*. The equation (6) has the different maximums and minimums depending on its value (see Fig 1).The value of a for the first order transition is found from the solution of the system of equations $f(a,x)=0$ and $\partial f/\partial x=0$. As a result, $a=2/9$.For this value the function (6) has the two minimums corresponding $x=0$ and $x=2/3$ and the maximum at $x=1/3$ (see Fig 1, curve 3).The value of the potential barrier and the jump of the order parameter in this transition can be estimated from the relations (6) and (7). The result, we will get

$$\Delta G/V_0=(1/324)(v^4/w^3);\ \eta=2v/(3w) \quad (8)$$

Now we'll define the entropy change $\Delta S=-(1/V_0)(\partial\Delta G/\partial T)_P$ at the elastic phase transition between the two states connected by the deformation $\eta=(2v/3w)$. Substituting η in to the formula (5) for Gibbs potential and taking the derivative over the temperature, we'll find ΔS till the fourth order degree over the order parameter. With the known ΔS, we'll find the latent transition heat $\Delta Q=T\Delta S$. So, the height of the potential barrier, the order parameter jump ,the entropy change and the latent heat of transition are defined by the relations between the third and fourth order elastic constants, e.g.by the nonlinear elasticity of the crystalline lattice. It is seen from the expression for the parameter a (see (7)), that the first order phase transition can take place at rather big values of q (corresponding second order EC), if the value of v is approximately equal to w (the third order anharmonism contribution is comparable with the fourth order contribution).

Now will consider the equation (5) when the third order contribution is not zero (the cases 1, 3 and 4).The calculations of EC show that usually far from the loss of stability point, q and w are positive, but v is negative. The equation (5) contains the three parameters, which depend on *P* and *T*, but dividing the both parts of the equation on $G_0=v^4/w^3$,we will get the dimensionless equation with one coefficient [4]

If $0\langle a\langle(2/9)$, then $f(a,x)$ has besides the metastable minimum has the stable minimum at $x\rangle 2/3$ with the maximum $f(a,x)\rangle 0$ for x between these minima (Fig 1,curve 4). As a result, the first order phase transition close to the second order will take place, because the potential barrier height is decreased with decreasing of a.

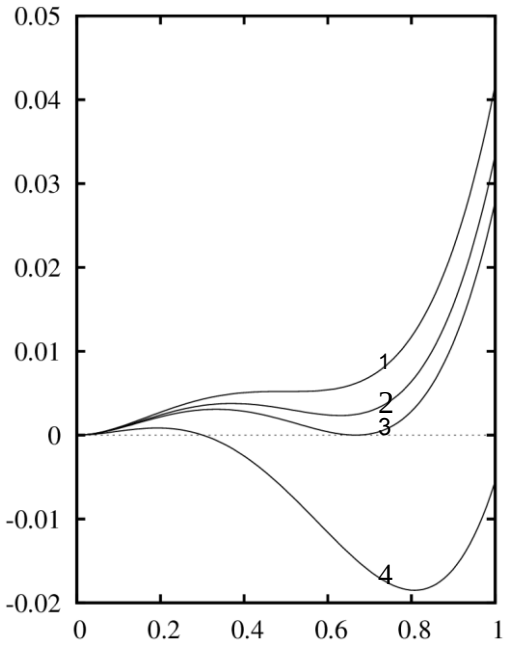


Fig 1.*The dimentionless Gibbs potential (6) at different values of* a *: 1.* a *=1/4, 2.* $a = 2.1/9$ *3.* $a = 2/9$ *.4.* $a = 1.4/9$.

The first order phase transition can take place at $0 \langle a \le \frac{2}{9}$, or for the elastic constants $0 \langle qw \le \frac{2}{9} v^2$

Thus, the data for the second-forth order EC at the different pressures are needed to analyze the elastic phase transitions. The experimental data for the different order elastic constants at the high pressures are practically absent. But the second and higher order EC at the different pressures can be obtained from the "first principles" calculations in the framework of DFT. We have described the calculation method of the second-forth order EC for cubical and hexagonal crystals in the papers [5,6].

3.**The EC of the refractory metals at high pressures.**

Vanadium. The structural phase transition under pressure from *bcc* to rhombohedral structure was found at $P = 69$ *GPa* and the room temperature [7]. The authors of [7] explain it by softening of EC $\tilde{C}_{44}$ ($\tilde{C}_{44}$ becomes negative in the investigated pressure range) and connect the absence of the volume jump with the second order transition. The softening of $\tilde{C}_{44}$ (it becomes negative) was found also in framework of the first principles calculations (see, for example [9]). It is possible to estimate from [9] the value of a (see (6) and (7)) at the different pressures (*T=OK*) near the phase transition point (50 - 70 *GPa*), using the results of the second - forth order ECs calculations. In a result, we have: at $P \approx 68$ *GPa*, the a becomes equal to the critical value 2/9, and the *bcc* structure (Γ_c^{ν}) can experience the structural transition to the rhombohedral phase (Γ_{rh}), (see Table 1, line 3).From (8) it is possible to obtain the jump of the order parameter

$\eta_{12} = \eta_{13} = \eta_{23} = \eta / 2 = (1/3)(|\nu| / w)$ =0.0075 at this transition. The small value of the order parameter means that it is the first order transition, close to the second order. The calculation results are in a good agreement with the experimental data [7].

Molybdenum. The effective EC of Mo in the pressure interval 0-1400 *GPa* (*T=0K*), which were obtained in our work [9], are given on Fig 2-4. It is seen on Fig 2, that $\tilde{C}'$ at P> 500 *GPa* is strongly softened (this is the precursor of the phase transition) and passes the zero at P= 1400 *GPa* ($V/V_0 \approx 0.42$).The *bcc* lattice at these experiences the phase transition to a tetragonal or orthorhombic structure (the stability condition (2b) is distorted). But according to [10, 11] the *bcc* molybdenum structure at $P \approx 700$ *GPa* (*T=0K*) becomes thermodynamically unstable and should transform in *fcc* or hexagonal phase. The estimations of the coefficient a (see (6)) show, that at these pressures its exceeds the critical value 2/9, when the first order phase transition can take place. The results of the stability criteria (3) and (4) calculations for f*cc* and *hcp* structures of molybdenum are given on Fig 3 and 4. It is seen that at the normal (atmospherically) pressure these structures are unstable relative to the shear deformations ($\tilde{C}_{44}$ ‹0 и $\tilde{C}'$ ‹0)). They are stabilized only at the high pressures: *hcp* at $P \ge 150$ *GPa*, *fcc* at $P \ge 300$. As can be seen from Fig. 3 and 4, from the point of view of resistance to homogeneous deformation of the hexagonal structure is more preferable. The small $\tilde{C}'$ value creates the small energetic barrier for this structural transformation. The transition will be of the first kind and occurs before a phonon mode in the original lattice becomes unstable. Thus, the structural transition in Mo in the *hcp* phase must occur before the EC $\tilde{C}'$ will become zero.

These considerations apply to tungsten. Elastic constants of 2 – 4 order in *bcc* – W and their analysis is given in [12]. EC $\tilde{C}'$ also demonstrates a tendency to soften, although at higher pressures.

Ruthenium. Elastic constants $\tilde{C}'$ and $\tilde{C}_{44}$ *hcp* Ru grow monotonically in the range of 0-600 *GPa* [6]. Thus, the *hcp* structure of ruthenium remains mechanically stable in the investigated pressure interval.

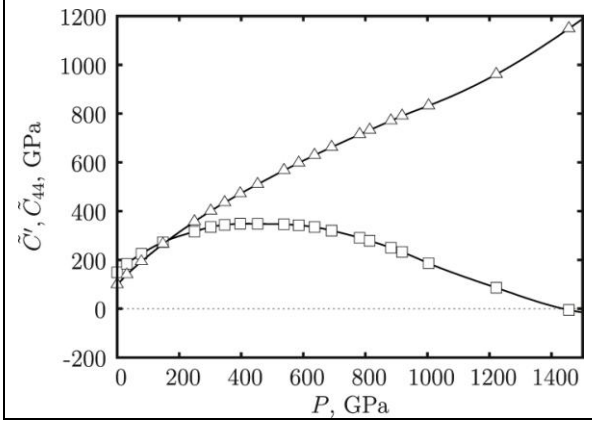


Fig.2 *The pressure dependence of the shear ECs of bcc Mo:* $\tilde{\tilde{C}}' = (\tilde{\tilde{C}}_{11} - \tilde{\tilde{C}}_{12})/2$ *-square ,* $\tilde{\tilde{C}}_{44}$ *- triangular*

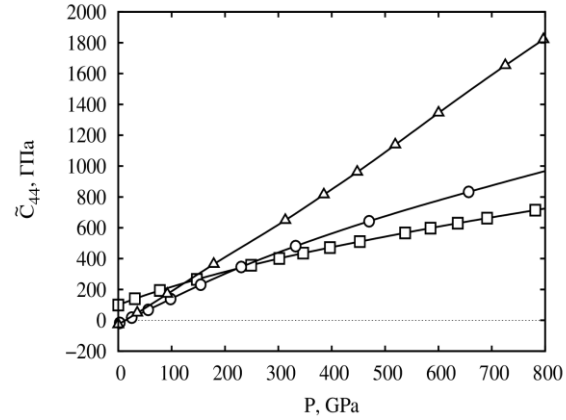


Fig.3. *The change of the EC* $\tilde{\tilde{C}}_{44}$ *under pressure in bcc, fcc and hcp molybdenum. The square – fcc, circle – fcc, triangular - hcp*

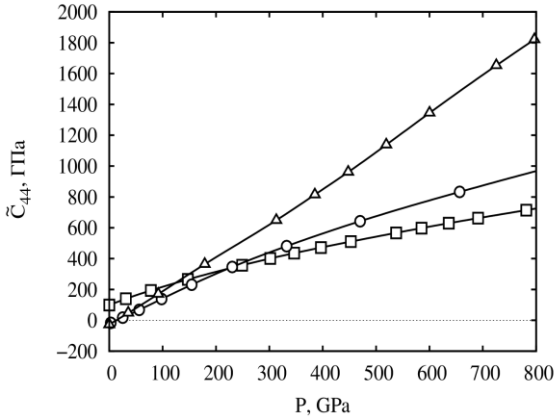


Fig.4. *The change of the EC* $\tilde{\tilde{C}}'$ *under pressure for bcc, fcc and hcp molybdenum. Square-bcc, circle - fcc, triangle – hcp structures.*

The work is executed at financial support of the Ministry of Education and Science of the Russian Federation (Grant No. 14.Y26.31.0005) and the Russian Foundation for Basic Research (grant 16-02-00699).

References

1.Bushman A V, Fortov V E *Phys. Usp. 26 465* (1983)
2. Maksimov E G, Magnitskaya M V, Fortov V E *Phys. Usp.* **48** 761 (2005)
3 Cowley R A *Phys. Rev B* **13** 4877 (1976)
4 Krumhansl J A and Gooding R J *Phys. Rev. B*. **35** 304 (1989)
5. Векилов Ю.Х., Красильников О.М., Луговской А.В. УФН т.185 (11), 1215 (2015)
6. Lugovskoy A.V.,Belov M.P., Krasilnikov O.M., Vekilov Yu. Kh. J. Appl. Phys. 116, 103507 (2014)
7. Ding Y et al. *Phys. Rev. Lett*. **98** 085502 (2007)
8. Krasilnikov O M et al. *J. Phys.: Condensed Matter*. **24** 195402 (2012)
9. Krasilnikov O M et al. *Comp. Matter. Sci*. **81** 313 (2014)
10 Belonoshko A B et al. *Phys. Rev. Lett.* **100** 135701 (2008)
11 Wang B., Zhang G.B., Wang Y.X. *J. Alloys and Compounds* **556** 116 (2013)
12 Vekilov Yu Kh, Krasilnikov O M, Lugovskoy A V, Lozovik Yu E *Phys. Rev. B* 94 104114 (2016)

INFLUENCE OF THERMAL-CYCLIC DEFORMATION AND HEAT TREATMENT ON THE STRUCTURE AND PHYSICAL PROPERTIES OF STEEL 10

ВЛИЯНИЕ ТЕРМОЦИКЛИЧЕСКОЙ ДЕФОРМАЦИИ И ТЕРМИЧЕСКОЙ ОБРАБОТКИ НА СТРУКТУРУ И ФИЗИЧЕСКИЕ СВОЙСТВА СТАЛИ 10

D.Sc. (Eng.), Prof. Prudnikov A., Ph.D. student Prudnikov V.
Siberian State Industrial University, Russia
E-mail: a.prudnikov@mail.ru, vladpr88@gmail.com

Abstract: *The results of the influence of preliminary thermal-cyclic deformation and subsequent annealing in the range of 100÷900 ºC with a step of 100 ºC on the microstructure, coercive force and linear expansion of hot-rolled sheet steel 10 are presented. It was found that the use of preliminary thermal-cyclic deformation results in increase in coercive force no more than by 8% in comparison with the steel sheet produced by an industrial technology. Decreasing feasibility in coercive force of the sheet steel produced with the use of thermal-cyclic forging almost by 3 times in comparison with the initial raw condition due to the subsequent annealing at 900ºC during 10 h. is shown. In addition, annealing in accordance with this mode reduces a temperature coefficient of linear expansion of a sheet steel on average by 6 % within the range of the test temperatures 50-450 ºC.*

KEYWORDS*: STRUCTURE, STEEL, DEFORMATION, ANNEALING, PHYSICAL PROPERTIES, THERMAL-CYCLING DEFORMATION, COERCIVE FORCE, LINEAR EXPANSION.*

1. Introduction

Vast majority of half-finished goods, details and structural elements of products from various materials is used in industry after the strengthening technologies – deformation, thermal or superficial chemical heat treatments. However, increasingly restrictive requirements to the modern equipment brought in to existence the complex technologies including combined use of various techniques for both structure formation and management and, therefore, properties of materials. The thermo-mechanical, mechanical-thermal and more difficult – deformation thermal cyclic treatment (DTCT) belong to such technologies. The technological modes of these types of processings combine different types of cold and hot deformation with heats, holding at the fixed temperatures and cooling in the wide range of speeds (in water, on air or in furnace). DTCT is distinguished by repeatability of processing cycles. At that, the number of processing cycles and their parameters (temperature of heating and cooling; temperature interval of deformation; a type and deformation ratio in the cycle; overall deformation ratio, etc.) are subject to vary over a wide range. DTCT is widely covered in the literature as a technology applied for hardening of ferrous and non-ferrous metals and alloys, including steels, cast iron and aluminum alloys [1-9]. Much lesser attention is given to a problem of improvement electric, magnetic, thermal and other physical properties of various materials. It is possible to refer works of authors [1, 10-12] to such publications. One of the perspective directions of the use of DTCT is giving to structural low-carbon steel the properties being near to properties of some groups of the magnetically soft materials, in particular, technically pure iron and electrical steel which are combined with advanced mechanical and technological properties. Besides, an additional reserve for improvement properties of low-carbon steel can serve the subsequent heat treatment having impact on its structure and the most important properties, such as electric, magnetic and thermal (specific electric resistance, electric conductivity, losses on magnetic reversal, the coercive force, coefficient of thermal expansion, etc.) for the magnetically soft materials. Therefore, the aim of this work was to study the effect of the preliminary thermal - cyclic forging and the subsequent annealing on the coercive force and linear expansion of sheet hot-rolled steel 10.

2. Material and methods

Low-carbon fine steel 10 was used as a material in the study. The steel was made at the Novokuznetsk Iron and Steel Plant JSC (Novokuznetsk, Russia). The chemical composition of experimental steel, in % (weight): C – 0,13; Si – 0,22; Mn – 0,42; P – 0,014; S – 0,018; Cr – 0,05; Ni – 0,04; Cu – 0,20; As – 0,06; Fe – the rest. A slab of steel 10 was subjected to hot cyclic forging through single-pass broaching by flat backups with blank turning at the forge-thermal shop of the West Siberian Metallurgical Plant (Novokuznetsk, Russia) using a hydraulic forging press with the load of 2000 ton-force. A hot cyclic forging technique is presented in this work [11], and its main characteristics and technique are given below. The heating temperature before forging was 1250 °C, the slab holding time in the furnace before forging was 2 hours. Forgings were cooling in the air to 200-300°C. There were 10 cycles of forging with a deformation ratio in each cycle 6 ÷ 8 %. Overall deformation ratio was 65÷68 % at the overall reduction ratio – 1.90.

Further the blanks were rolled to sheets 3 mm thick at the semi-continuous hot-rolling combination mill 810 according to the manufacturing process for hot-rolled sheet carbon steel 10. Before rolling the blanks were preheated in a gas furnace. The heating temperature of blanks for rolling was 1120÷1250 °C, and the holding time in the furnace was 2÷2,5 hours. The rolling finishing temperature for a sheet 3 mm thick was 800 - 860 °C. In further detail, technological mode of hot-rolled sheet carbon steel 10 is given in the work [2].

Annealing of the specimens cut from sheets was carried out in resistance furnaces SNOL 2.2, 5.2 / 12.5-I1. An optical microscope LaboMet-I1was was used to investigate the microstructure of the steel. High-temperature dilatometer DIL 402C with digital data processing and error of measurement of $0{,}1 \cdot 10^{-6}$ K^{-1} was used for determination the temperature coefficient of linear expansion (TCLE) of steel specimens at various temperatures. Determination the coercive force was carried out on KIFM-1 coercimeter with a probe-type magnetic-field sensor (demagnetization current of a magnetic conductor $8 \cdot 10^{-3}$ A) on rectangular sheet specimens 90×120 mm with a thickness of 3 mm. The measuring error was 4 A/m.

3. Results and discussion

One of the most important properties of the magnetically soft materials is the coercive force determining losses of energy on magnetization reversal of magnetic circuits elements. First of all, that belongs to cores of the magnetic conductors with difficult configuration, stators and rotors of high-frequency machines, throttles, transformers and other structural elements [13]. In this regard the size of coercive force has been determined for the hot-rolled steel 10 made by an industrial technology of rolling and with the use of preliminary DTCT. She was 214 A/m in the first case. If thermal-cyclic forging are used, she was 232 A/m. Such increase in coercive force due to the using modes of preliminary thermal-cyclic forging at production of sheet hot-rolled steel 10 can be explained with the changes occurring in its microstructure:

grains crushing of ferrite and pearlite colonies oriented along the rolling direction (first of all). This fact corresponds with results of the metallographic researches carried out in works [2, 6]. Such a fine crushing of structural components and, therefore, increase in extent of grain boundaries, where crystal structure imperfections (dislocations, vacancies, etc.) are gathered, is a reason for increasing in size of the coercive force in structure of the sheet steel 10 made with use of DTCT. Magnetic elements work often in the industry at the elevated and lowered temperatures, including widespread lamellar stacked cores with electrically insulated coating, the magnetically operated sealed switches (gerkon) and other products of this sort. Therefore, one of important characteristics for such products made from magnetically soft materials is a characteristic of thermal expansion – the temperature coefficient of linear expansion (TCLE). Performed impact studies of the mode of thermal-cyclic forging on linear expansion of steel 10 revealed that use of DTCT doesn't exert impact on true temperature coefficient of linear expansion. The size of its change after cyclic forging and rolling to a sheet doesn't exceed 5 % (fig. 1). However, it is possible to note a tendency of the coefficient increasing in the field of low test temperatures (to 300 °C) by 5 % in comparison with coefficient of hot-rolled steel made by an industrial technology and opposite change of TCLE values for more high test temperatures (300-450 °C).

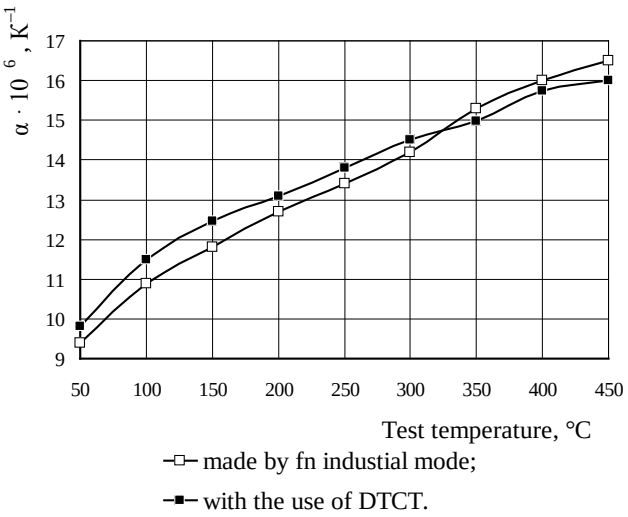


Fig.1 *– Influence of thermal -cycling forging on the linear expansion of hot- rolled sheet steel 10 (sheet thickness of 3mm)*

Further influence of the subsequent annealing during 10 h was investigated on physical properties of the sheet steel 10 (3 mm thick) subjected to DTCT. It is established that increase in annealing temperature from 100 to 900 °C with a step of 100 °C leads to a consecutive decrease in size of steel coercive force (fig. 2). Its intensive decreasing was noted at more high annealing temperatures, beginning from 600 °C. The minimum value of coercive force corresponds to annealing at temperature of 900 °C and is 83 A/m, that is nearly 3 times lower, than at specimens without heat treatment. Apparently, coercive force decrease of the sheet steel made with the use of DTCT can be attributed, with increase in annealing temperature, to general decreasing in stress level and defects of the crystal structure (vacancies, dislocations, etc.), which are formed in metal as a result of the used modes both of deformation and cooling and also significant growth in grain of ferrite and some reduction of a volume fraction of the pearlitic colonies.

Influence of the subsequent annealing temperature during 10 h on linear expansion of the sheet hot-rolled steel 10 subjected to DTCT is investigated in this work. Received curves of temperature dependence of true TCLE of the steel 10 made with thermal cyclic forging, after annealing at 600, 700, 800 and 900 °C are given in fig. 3.

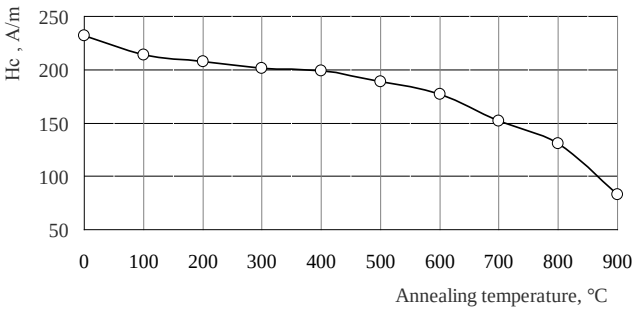


Fig. 2 *– Influence of heating temperature with cooling in the furnace on the coercive force of the steel 10 made with the use of DTCT*

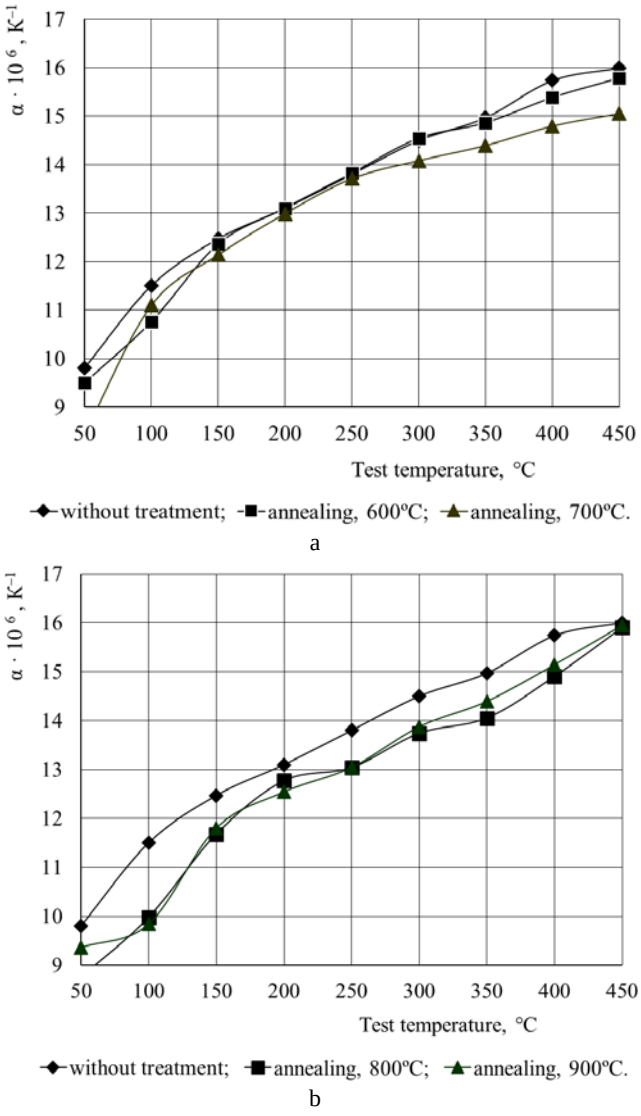


Fig. 3 *– Influence of annealing temperature at 600 and 700 ºC (a) and 800 and 900 ºC (b) (holding time 10 h) on linear expansion of the sheet hot-rolled steel 10 made with use of DTCT*

Graphic dependences of average coefficient according to test temperature intervals from annealing temperature (fig. 4) are constructed on the basis of the analysis of temperature dependence curves of true TCLE of the steel 10, made with use of thermal-cyclic forging after annealing during 10 h at 600, 700, 800 and 900 °C (fig. 4)

Obtained dependences allow to grains draw a conclusion about decrease in the steel 10 capability to thermal expansion after annealing at all studied temperatures; beside that, annealing of steel at 800 and 900 °C reduces TCLE more considerably.

This decrease averages are more than 6 % in all temperature interval of tests (to 450 °C). At that, annealing at 800 and 900 °C reduces most considerably the average value of TCLE in the field of low temperatures of 50-100 and 50-200 °C. So, this reduction makes 8 and 12 % after annealing at 800 °C, and 12 % respectively after annealing at 900 °C – 7 in comparison with thermally raw steel samples.

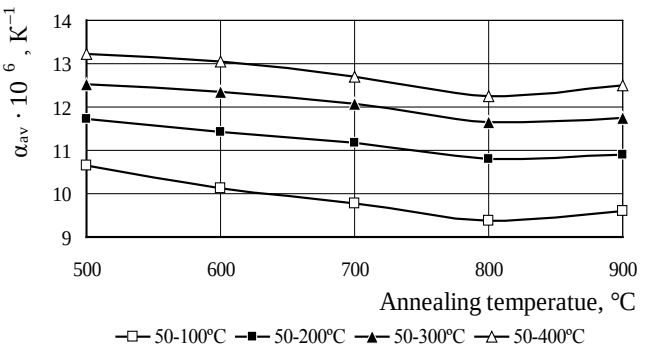


***Fig. 4** – Influence of annealing temperature on average TCLE in various intervals of test temperatures of the sheet hot-rolled steel 10 made with use of DTCT*

4. Conclusions

1. The use of thermal-cyclic forging for the production of sheet steel 10 (thickness of 3 mm) increases the size of its coercive force no more than by 8 % in comparison with the industrial mode and has no significant influence on its thermal expansion.

2. The subsequent high-temperature annealing (900 °C) during 10 h of the sheet steel 10 made with use of thermal-cyclic forging allows to reduce its coercive force by almost 3 times in comparison with stock material.

3. The most considerable decrease in TCLE for the steel 10 produced with use of DTCT is observed at the subsequent high-temperature annealing (800 and 900 °C) on average more than by 6 % in an interval up to 450 °C and average coefficient in low-temperature area (up to 100 and 200 °C) by 7-12 %.

5. References

1. Fedyukin, V. Thermocyclic processing of metals and details of cars. Leningrad, Mashinostroenie Publ., 1989, 255 p. (Fedyukin, V., M. Смагоринский).

2. Prudnikov, A. Influence of Thermal-Cyclic Deformation and Hardening Heat Treatment on the Structure and Properties of Steel 10. – Applied Mechanics and Materials, Vol. 788, 2015, pp. 187 - 193 (Prudnikov A., M. Popova, V. Prudnikov).

3. Taskin M. Diffusion boonding of fine grained high carbon steels in the super-plasticity temperature range.– J. of Engineering Mater. Sci., Vol. 12, 2006, pp. 362-367 (Taskin M., M. Orhan, S. Ozan).

4. Prudnikov, A. The complex effect of annealing and thermal cycling forging on the structure and properties of hypereutectic silumins. – Deformatsiya i razrushenie materialov, v. 2, 2014, pp. 14-20 (Prudnikov, A.).

5. Churakova, A. Mekhanicheskie svoistva splava TiNi, poluchennogo intensivnoi plasticheskoi deformatsiei i posleduyushchei termotsiklicheskoi obrabotkoi.– Vektor nauki TGU, No 3 (25), 2013, pp. 288-291 (Churakova A., Д. Гундеров).

6. Prudnikov, A. Hardening low carbon steel 10 by using of thermal-cyclic deformation and subsequent heat treatment.– Material science. Non-equilibrium phase transformations, I. 4, 2016, pp. 10-14 (Prudnikov, A., M. Popova, V. Prudnikov).

7. Gorbachev, S. Issledovanie raznozernistosti pri defformatsionno-termicheskoi obrabotke svarnykh soedinenii iz stali 20.– Neftegazovoe delo, No1, 2014, pp. 302-316 (Gorbachev, S., A. Щипачев, Р. Литфуллин).

8. Furuya, Y. Thermal Cyclic Deformation and Degradation of Shape Memory Effect in Ti-Ni Alloy.– Nondestructive testing and evaluation, vol. 8(1), 1992, pp. 541-554 (Furuya, Y.,Y. Park).

9. Prudnikov, A. Strukturno-tekhnologicheskie osnovy razrabotki pretsizionnykh siluminov s reglamentirovannym soderzhaniem vodoroda / Avtoreferat dissertatsii na soiskanie uchenoi stepeni doktora tekhnicheskikh nauk: 05.16.09 / NGTU, Novosibirsk, 2013. – 40 p (Prudnikov, A.).

10. Prudnikov, A. Assessment of impact of thermocyclic deformation and the subsequent heat treatment on electrophysical properties of low-carbonaceous steel.– Actual problems in machine building, v. 2, 2015, pp. 396-400 (Prudnikov, A., V. Popova, V. Prudnikov).

11. Prudnikov A.N. Otsenka struktury, svoistv i zagryaznennosti nemetallicheskimi vklyucheniyami deformatsionno-termotsiklicheski obrabotannoi stali 10 / A.N. Prudnikov, V.A. Prudnikov, E.V. Bogonos / Sb. materialov KhIKh Mezhd. nauchn.-prakt. konf. “Metallurgiya: tekhnologiya, innovatsii, kachestvo” – 15-16 noyabrya 2015 g. – Novokuznetsk, izd-vo SibGIU, 2015. – pp. 35-39.

12. Prudnikov, A. Piston deformable hypereutectic silumin. – Tekhnologiya metallov, v. 2, 2014, pp. 8-11 (Prudnikov, A.).

13. Kekalo I. Fizicheskoe metallovedenie pretsizionnykh splavov. Splavy s osobymi magnitnymi svoistvami. – M., Metallurgiya, 1989, 496 p. (Kekalo, I., В. Самарин).

PRESSURE DERIVATIVES OF ELASTIC CONSTANTS OF ALUMINUM ALLOY AMg6 AND NANOSTRUCTURED ALLOY n-AMg6. COMPARISON OF EXPERIMENTAL AND CALCULATED FROM THIRD-ORDER ELASTIC CONSTANTS DATA

ПРОИЗВОДНЫЕ ПО ДАВЛЕНИЮ УПРУГИХ ПОСТОЯННЫХ В АЛЮМИНИЕВОМ СПЛАВЕ АМг6 И НАНОСТРУКТУРИРОВАННОМ СПЛАВЕ n-АМг6. СРАВНЕНИЕ ЭКСПЕРИМЕНТАЛЬНЫХ И РАССЧИТАННЫХ ИЗ УПРУГИХ ПОСТОЯННЫХ ТРЕТЬЕГО ПОРЯДКА ДАННЫХ

Assoc. Prof., Dr. Prokhorov V.[1], Leading Res., Dr. Gromnitskaya E.[2],
Technological Institute for Superhard and Novel Carbon Materials[1], Moscow, Russia, Institute for High Pressure Physics Russian Academy of Sciences[2], Moscow, Russia,
E-mail: pvm@tisnum.ru, grom@hppi.troitsk.ru

Abstract: *Research results for the nonlinear elastic characteristics of the polycrystalline aluminum alloy AMg6 and AMg6/C_{60} nanocomposite (n-AMg6) have been described. The ultrasonic study of the elastic characteristics at pressures up to 1.6 GPa has been carried out using a high-pressure ultrasonic piezometer based on the piston-cylinder device. Pressure dependencies of the longitudinal and shear elastic waves velocities and densities of AMg6 and n-AMg6 were experimentally measured and the pressure derivatives of the second-order elastic constants were calculated. The results derived by this method have been compared with the results of studies of the nonlinear elastic properties of the test alloys using the Thurston–Brugger quasi-static method, where third-order elastic constants have been measured. The relationships between the pressure derivatives of the second-order elastic constants of these alloys and the Mg-content and nanostructuring were established.*

***KEYWORDS**: AMg6 ALLOY, AMg6/C_{60} NANOCOMPOSITE, SECOND- AND THIRD-ORDER ELASTIC CONSTANTS, PRESSURE DERIVATIVES OF THE ELASTIC CONSTANTS.*

1. Introduction

Nonlinear elastic characteristics, such as second-order elastic constants C_{ijkl} (SOECs) and its pressure derivatives, third-order elastic constants C_{ijklqr} (TOECs), are important physical parameters of materials. They describe the anharmonic properties of the crystal lattice, such as thermal expansion, ultrasound attenuation, and efficiency of the interaction of acoustic waves in solids. Nonlinear properties are also important in the nondestructive determination of structural characteristic and mechanical behavior of materials [1,2]. TOECs and pressure derivatives of SOECs are important parameters of the equation of state of materials [3].

Cast alloy AMg6 belongs to the Al–Mg–Mn system, containing 93.68% aluminum, 5.8–6.8% magnesium, and 0.5–0.8% manganese and other impurities [4,5]. It combines good strength and plastic characteristics at room and higher temperatures, and well-welded. This set of properties favored the wide application of this alloy in the aerospace industry, building, and automobile engineering, while the corrosion resistance in various media, including seawater, explains its successful use in shipbuilding. The alloy refers to strain hardening.

In recent, much progress has been made in nanostructuring of solids, leading to new, unusual combinations of properties, such as high strength and ductility combined with high hardness. So, equal channel angular pressing of AMg6 cast alloy allowed one in [6] to obtain the material with the average grain size of 400 nm with the significantly improved mechanical properties (the breaking point σ_B increased from 210 MPa of cast alloy to 440 MPa, and the elongation at break δ is twice augmented to 25% at room temperature). The higher values of mechanical characteristics in nanocomposite carbon-hardened AMg6 alloy prepared via grinding in a ball mill with subsequent extruding were acquired in [7]. The elongation at break in nanocomposite AMg6 was increased to 10.5–14.1% at higher hardness of 1.5–1.7 GPa.

In a series of our studies, we measured the elastic characteristics (SOECs and TOECs) of some of aluminum alloys (B95, D16, AMg6) and the B_4C ceramics [8-10], and investigated the effect of nanostructuring on TOECs values for aluminum alloys n-B95 [11-12] and n-AMg6 [13-14].

In this study we measured the SOECs pressure derivatives for the polycrystalline aluminum alloy AMg6 and the nanostructured n-AMg6 alloy. The experimentally determined TOECs of AMg6 and n-AMg6 alloys [14] are used to evaluate the SOECs pressure derivatives and are compared with the measured values.

2. Linear and nonlinear elastic properties

The linear elastic properties of the solids can be evaluated with the second-order elastic constants C_{ijkl} (SOECs). The measurements of the longitudinal $V_L = \sqrt{C_{11}/\rho}$ and shear $V_T = \sqrt{C_{44}/\rho}$ velocities in bulk acoustic waves (BAWs) and the density ρ_0 of the samples allowed us to determine two of them, the C_{11} and C_{44}, and calculate the Young´s modulus E, the bulk modulus B, the Poisson's coefficient σ and the Lame parameters λ, and $\mu = C_{44}$.

The SOECs for nanomaterials are almost equal to those of the appropriate initial microcrystalline objects. This conclusion is, however, valid for materials with the low interface fraction (the atom content at the interface to the amount of atoms in the bulk). At a crystallite size of less then 10 nm, when this fraction is dozens of percent, the elastic characteristic values are expected to additively reduce owing to the inner porosity in the nanomaterial. Obviously, the pronounced decrease in the elastic characteristics can be avoided by filling the voids of nanoparticle joints with a material possessing high elastic and strength properties (i.e., by forming a nanocomposite), whereas the formation of the chemical bounds between this material and the nanoparticle surface can also favor to the increase in the elastic moduli [15].

To characterize the nonlinear elastic properties of solids the third-order elastic moduli (for isotropic solids) and third-order elastic constants C_{ijklqr} (TOECs) are used. In the isotropic solid, 18 TOECs are nonzero. In this case, three constants C_{111}, C_{112}, and C_{123} are considered as independent; the others are their linear combinations [16]. Also three third-order modules were introduced for isotropic solid. As in the case of second-order modules, the third-order modules can be selected in various ways. Modules ν_1, ν_2, and ν_3 are most commonly used lately [17]. The relationship between them and TOECs is given in [9].

To determine the TOECs, the Thurston–Brugger quasi-static method is used [18]. To do this, relative changes in velocity of bulk

waves, depending on the applied uniaxial compression, were experimentally measured in the test samples. In this case, changes in the transit times of ultrasonic waves in the samples are measured as a function of the applied stress P and the derivatives $[\partial (\rho_0 W^2)/\partial P]_{p=0}$ are calculated. From the data obtained, TOECs are determined:

$$[\partial (\rho_0 W^2)/\partial P]_{P=0} = (2 \rho_0 W^2 F + G) \qquad (1)$$

where $W = l_0/t$ (P) is the "natural" velocity of BAW, ρ_0 is the density, $F = S_{jkab}M_aM_bU_jU_k$, $G = S_{ipab}C_{jrksip}U_jU_kN_rN_sM_aM_b$, S_{ipab} are the second-order compliance coefficients, U_k is the components of the polarization vector **U**, N_r are the components of the wave vector **N**, and M_i are the components of the unit vector **M** in the uniaxial compression direction.

The experiments on hydrostatic compression directly measure the pressure derivatives of SOECs C_{11} and C_{44}. For the calculation of 3 independent TOECs the measurements in hydrostatic conditions must be supplemented by measurements under conditions of uniaxial compression. However, to determine the three independent TOECs C_{111}, C_{112}, C_{123} in an isotropic solid, it is sufficient to carry out three independent measurements of the dependence of the BAW velocity on the uniaxial compression **P** with the following mutual arrangement of the unit vectors M, N, U:

$\mathbf{N} \parallel \mathbf{U} \perp \mathbf{M}$, $\mathbf{N} \perp \mathbf{U} \parallel \mathbf{M}$, $\mathbf{N} \perp \mathbf{U} \perp \mathbf{M}$.

The direction of uniaxial compression for all measurements must be perpendicular to the propagation direction of the elastic wave. The convolution for ρ_0, W^2, F, G in (1) for these cases is given in [9].

To increase the accuracy of measurements, they are often carried out for more than three combinations of directions of the unit vectors **M**, **N**, **U**.

Third order elastic modules and TOECs of aluminum alloys were studied by many authors for a long time [3].

In [9,13,14], linear and nonlinear elastic properties of samples of a polycrystalline industrial aluminum alloy AMg6, corresponding to GOST 4784-74 and a nanostructured n-AMg6 alloy obtained from it, were studied in detail. The results of these measurements are given in Table 1. The error value of TOECs in Tabl. 1 does not exceed 15%.

Table 1 *Average values of TOECs of AMg6 and nanostructured n-AMg6 (in GPa).*

Material	C_{111} (± 240)	C_{112} (± 120)	C_{123} (± 70)	$\nu_1=C_{123}$ (± 70)	$\nu_2=C_{144}$ (±20)	$\nu_3=C_{456}$ (±10)
AMg6	-3420	-1310	-860	-860	-230	-150
n-AMg6	-2770	-980	-680	-680	-150	-150

3. SOECs pressure derivatives

In the present work, using the data for the TOECs, we calculated the pressure derivatives of the SOECs. The results of calculations are presented in Table 2.

Table 2 *Average values of SOECs pressure derivatives of AMg6 and n-AMg6.*

Material	$\partial C_{11}/\partial P$	$\partial B/\partial P$	$\partial C_{44}/\partial P$
AMg6	27.4	20.7	5.0
n-AMg6	22.2	16.7	4.1

We note that among the known literature data on the SOECs pressure derivative values for aluminum alloys [3,19,20], the largest values are for those containing Mg [3].

The calculated values of the SOECs pressure derivatives for the polycrystalline aluminum alloy AMg6 and the nanostructured n-AMg6 alloy noticeably exceed the values of the literature and tabular data for other aluminum alloys that are close in composition to AMg6.

In order to verify our results of measurements of the TOECs, we conducted direct measurements of the pressure derivatives of the SOECs under conditions of quasi-hydrostatic pressure up to 1.6 GPa.

4. Materials and Experiment

Nanostuctured samples n-AMg6 were prepared from a commercial polycrystalline alloy by refinement and homogenization a mixture of small chips of the alloy with the addition of 0.3 wt.% fullerite C_{60} in a planetary mill AGO-3Y in-cycle work 60 min. The resulting product consists of 200-500 micron agglomerates of nanoparticles. The coherent scattering length (CSL) distribution in powdered samples showed the mean nanoparticle size ~ 40–60 nm.

The process was conducted in a protected Ar-atmosphere; additional studies confirmed the absence of oxygen and the corresponding insertion of aluminum oxidation.

Then, the milled nanopowder was pre-compacted in a cylindrical mold with a diameter of 180 mm at a temperature of 250 ^{0}C and a pressure of 200–300 MPa.

The resulting compact (preform) was subjected to extruding at a temperature of 300 ^{0}C with a reduction of cross-sectional area at least 4 times (in this case to a diameter of 90 mm). The recrystallization process is hindered by grain boundary modification with fullerite C_{60}; the latter plays the role of compacted samples' stabilizer. A general view of extruded billets and prepared samples for mechanical testing is shown in Fig. 1.



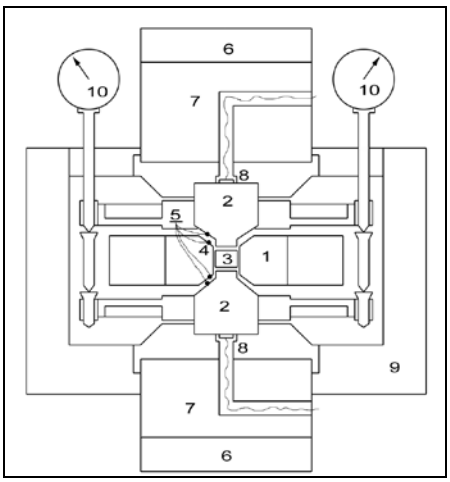
A) B)

Figure1 *General view of the samples n-AMg6/C_{60}:* A) *after extrusion;* B) *prepared test specimens*

For experiments under hydrostatic compression, the samples in the form of a disk with a diameter of ~16 mm and a height of ~6 mm were cut from the parent AMg6 and nanostructured n-AMg6.

The ultrasonic study of the pressure dependencies of elastic characteristics was carried out using a high-pressure ultrasonic piezometer based on the piston-cylinder device with the registration system of the transmitted and reflected sound built on the basis of the National Instruments PXI platform (Fig.2).

Changes in the ultrasonic signal paths were measured with 0.005 mm uncertainty using dial-type micrometer indicators. The volume of the samples under pressure was initially determined from the change in their length, and subsequently the equation of state was calculated by the recursive (with respect to density) integration of compressibility (reverse bulk modulus) with accuracy of the order of several %. The measurements of the changes in the transit times (to ±0.001μs) of longitudinal and transverse ultrasonic pulses were performed by the pulsed method using x-cut and y-cut LiNbO3 plates as piezoelectric sensors with carrier frequencies of 5MHz for transverse geometry and of 10 MHz for longitudinal one. The transit time was measured not only by time shift of the passed sound wave but also by the cross-correlation and autocorrelation method, when one could determine the absolute transit time of the sound wave in a sample. The estimated pressure uncertainty was 0.03 GPa [21].



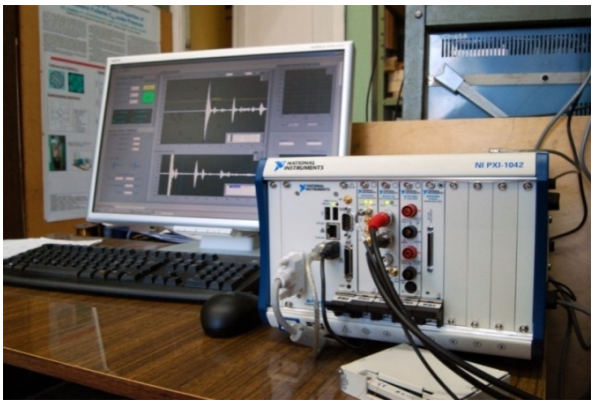
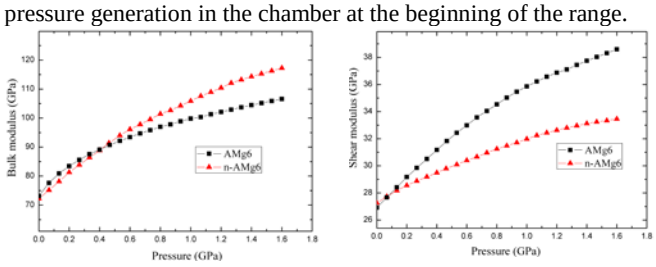


Figure 2 *High-pressure ultrasonic piezometer with the registration system built on the basis of the National Instruments PXI platform. 1 - high pressure cell, 2 - pistons, 3 - sample, 4 - fine copper foil, 5 – thermopairs, 6 - thermal isolation disk, 7 - steel tower, 8 - piesoelectric plates, 9 - thermal isolation tank, 10 - indicating gage.*

Corrections for the deformation of the chamber with the variation of pressure and temperature were determined in special experiments.

5. *Results and Discussion*

The obtained dependences of the elasticity characteristics on the pressure are shown in Fig.3. First of all, we note the pronounced nonlinear character of the dependence of the moduli on the pressure. Probably, this is due to the peculiarities of pressure generation in the chamber at the beginning of the range.



A) B)

Figure 3 *Pressure dependence of the elastic moduli of AMg6 and n-AMg6: A) B(P), B) G(P)*

In pressure ranges 0.2–0.8 GPa, $\partial B/\partial P$ is 26.7 and 33.6 for AMg6 and n-AMg6, respectively, but in pressure ranges 0.8–1.6 GPa $\partial B/\partial P$ is 11.3 and 18.9 for AMg6 and n-AMg6, respectively. Values $\partial G/\partial P$ in the indicated pressure ranges is 8.9 and 4.5 and 4.6 and 2.5 for AMg6 and n-AMg6, respectively.

In Table. 3 shows the average values of the pressure derivatives. The values for the range 0.8-1.6 GPa are shown in brackets.

Table 3 *Average values of SOECs pressure derivatives of AMg6 and nanostructured AMg6.*

Alloy	Mg(%)	$\partial C_{11}/\partial P$	$\partial B/\partial P$	$\partial C_{44}/\partial P$
AMg6[14]	5.8-6.8	27.4	20.7	5.0
AMg6 (Exp.)	7.08	25.1(18.8)	16.0(12.0)	6.8(5.1)
n-AMg6[14]	6.31	22	16.7	4.1
n-AMg6 (Exp.)	6.31	30.7(23.4)	25.8 (19.7)	3.6 (2.8)
D54S[19]	4.5	18.4	12.8	3.5
B53S[19]	2.8	9.7	6.0	2.1

The values of the pressure derivatives turned out to be significantly larger than those known from the literature for aluminum alloys [3]. According to the literature, it is clear that the Mg-containing aluminum alloys have the highest values of the SOECs pressure derivatives, in comparison with others.

In [19], the pressure derivatives of aluminum alloys D54S (Mg-4.5%, Mn-0,8%, Cr-0.1%) and for B53S (Mg-2.8%, Mn-0,8%, Cr-0.1%) were measured. Comparison with these data indicates the presence of dependence of SOECs pressure derivatives on the Mg-content. Our study shown that SOECs pressure derivatives of aluminum alloys belonging to the Al–Mg system increase monotonically with increasing content of Mg in the alloy.

The SOECs pressure derivatives calculated by TOECs and measured in this work agree well with each other with the exception of the $\partial B/\partial P$. According to the data computed from the TOECs values, the SOECs pressure derivatives of the n-AMg6 alloy are reduced. In our experiments, the values of the $\partial B/\partial P$ getting larger when nanostructuring. But the values of $\partial B/\partial P$ and $\partial C_{11}/\partial P$ measured in the pressure range 0.8-1.6 GPa are in good agreement with those calculated from the TOECs for both AMg6 and n-AMg6.

This can be explained as follows. In [14], the TOEC was measured at uniaxial pressure from 3 to 6 MPa. As can be seen

from Fig.3, at a low hydrostatic pressure (< 0.2 GPa), the $\partial B/\partial P$ for n-AMg6 is smaller than for AMg6.

6. Conclusion

The pressure derivatives of the second-order elastic constants of AMg6 and n-AMg6 were experimentally determined using a high-pressure ultrasonic piezometer based on the piston-cylinder device. Pressure dependencies of the longitudinal and shear elastic waves velocities and densities and constants were measured at pressures up to 1.6 GPa. The results derived by this method have been compared with the results of studies of the nonlinear elastic properties of the test alloys using the Thurston–Brugger quasi-static method, where third-order elastic constants have been measured. There is a good agreement of the pressure derivatives, obtained by direct measurements under hydrostatic pressure and calculated from TOECs defined by uniaxial loading method.

It is established that nanostructuring leads to a decrease in values of pressure derivatives of all the SOECs.

The values of the pressure derivatives of the SOECs increase monotonically with increasing content of Mg in the alloy.

7. Acknowledgments

This work was supported by the Ministry of Education and Science of the Russian Federation (project of the state assignment, task No. 3562); the work was done using the Shared-Use Equipment Center “Research of Nanostructured, Carbon and Superhard Materials” FSBI TISNCM. The authors acknowledge Evdokimov I., Pozdnyakov A., Perfilov S. for many assistance in samples preparation and useful discussions.

8. References

1. Zarembo, L. K., Krasil’nikov, V. A. Introduction to Non-Linear Acoustics. Moscow: Nauka, 1966, 519 p. (in Russian).

2. Rudenko, O.V. Giant nonlinearities in structurally inhomogeneous media and the fundamentalsof nonlinear acoustic diagnostic techniques. Phys. Usp., Vol.49, 2006, p.69–87.

3. Francevich, I.N., Voronov, F.F., Bakuta, S.A. Elastic Constants and Elastic Moduli of Metals and Nonmetals. Kiev: Naukova Dumka, 1982, 288 p. (in Russian).

4. Brostrem, V. A., N’Bushe, Construction Materials: A Handbook, Ed. by Arzamasov, B. N. Moscow: Mashinostroenie, 1990, (in Russian).

5. Babichev, A. P., Babushkina, N. A., Bratkovskii, A. M. in Handbook of Physical Quantities, Ed. By Grigoriev, E. S., Meilikhov, E. Z. Moscow: Energoatomizdat, 1991; Boca Raton, Florida, United States: CRC Press, 1997.

6. Valiev, R. Z., Aleksandrov, I. V. Bulk Nanostructured Metal Materials: Preparation, Structure and Properties. Moscow: Akademkniga, 2007, 398 p. (in Russian).

7. Lvova, N., Evdokimov, I., Perfilov, S. Comparative studies of nanostructured aluminum alloys by destructive and nondestructive testing. Adv. Mater. Res. Vol.1119, 2015, p. 9-13.

8. Prokhorov V., Kulibaba V., Korobov A., Stavrev S., Kolev S. Preparation and microstructure, elasticity and hardness investigation of Al-alloy/nanodiamond composite. Machines, Tecnologies, Materials. 2011; 11: 40-2.

9. Volkov, A.D., Kokshaiskii, A.I., Korobov, A.I., Prokhorov, V.M. Second- and third-order elastic coefficients in polycrystalline aluminum alloy AMg6. Acoustical Physics, Vol.61, 2015, p. 651–656.

10. Blank, V. D., Prokhorov, V. M., Sorokin, B. P., Kvashnin, G. M., Telichko, A. V., Gordeev G. I.. Second-order and third-order elastic constants of B_4C ceramics, Physics of Solid State, Vol. 56, 2014, p. 1574-578.

11. Korobov, A. I., Prokhorov, V. M., Mekhedov, M. Second-Order and Third-Order Elastic Constants of B95 Aluminum Alloy and B95/Nanodiamond Composite. Physics of Solid State, Vol.55, 2013, p.8-11.

12. Korobov, A. I., Prokhorov, V. M. Nonlinear acoustic properties of the B95 aluminum alloy and the B95/nanodiamond composite. Acoustical Physics, Vol.62, 2016, p. 681–687.

13. Prokhorov, V., Korobov, A., Kokshaiskii, A., Perfilov, S., Volkov, A. Effect of nanostructuring on the elastic properties of aluminum alloy AMg6. AIP Conference Proceedings**,** Vol. 1685, 2015**,** 080008; 4 p.; doi: 10.1063/1.4934461

14. Korobov, A.I., Kokshaiskii, A.I., Prokhorov, V.M., Evdokimov, I.A., Perfilov, S.A., Volkov, A.D. Mechanical and nonlinear elastic characteristics of polycrystalline AMg6 aluminum alloy and n-AMg6/C_{60} nanocomposite. Physics of the Solid State, Vol.58, 2016, p.2472–2480.

15. Prokhorov, V.M., Blank, V.D., Bagramov, R.H., Perfilov, S.A., Pivovarov, G.I. Nanostructured metal-nanocarbon composites: Production and studying of structural and mechanical properties. AIP Conference Proceedings**,** Vol. 1569, 2013, p.389-393.

16. Sirotin, Yu. I., Shaskol’skaya, M. P. Fundamentals of Crystal Acoustics, Moscow: Nauka, 1975, 680 p. (in Russian)

17. Toupin, R. A., Bernstein, B. J. Acoust. Soc. Am., Sound waves in deformed perfectly elastic materials. Acousto-elastic effect. Vol. 33, 1961, p.216-225.

18. Thurston, R. N., and Brugger, K. Third-order Elastic Constants and the Velocity of Small Amplitude Elastic Waves in Homogeneous Stressed Media. Phys. Rev., Vol. 133, 1964, p. A1604–1610.

19. Smith, R. T., Stern, R., Stephens, R. W. B. Third-Order Elastic Moduli of Polycrystalline Metals from Ultrasonic Velocity Measurements. J. Acoust. Soc. Am., Vol. 40, 1966, p. 1002-1008.

20. Muir, D. D., Michaels, Th. E., Michaels J. E. One-sided liquid coupled ultrasonic method for recovery of third order elastic constants. AIP Conference Proceedings**,** Vol. 1096, 2009, p.1275-1282.

21. Stal’gorova, O.V., Gromnitskaya, E.L., Dmitriev, D.R., Voronov, F.F. Ultrasonic piezometer for the 0–2.0 GPa pressure and 77–300 K temperature range. Instruments and Experimental Techniques, Vol. 39, 1996, p.880–883.

RESIDUAL STRESSES AND FRACTURE TOUGHNESS BORIDE CERAMIC COMPOSITES WITH MONOCRYSTALLINE MATRIX

[1]Soloviova T.O., [1]Loboda P.I., [2]Karasevska O.P., [1]Samsonik I.V.
[1]National Technical University of Ukraine "KPI", Peremohy Av. 37, 03680 Kyiv, Ukraine
[2]Institute Metal Physics. G.V. Kurdyumov Sciences of Ukraine, blvd.Acad. Vernadskogo 36, 03680 Kyiv, Ukraine

E-mail: tsolov@iff.kpi.ua

Abstract: *X-ray diffraction analysis studies the formation of a stress-strain state of single-crystal composites LaB_6-TiB_2 obtained under identical conditions by crucible-free float zone melting (FZM). The composites were obtained using monocrystalline LaB_6 substrate seeds with <100>, <110> and <111> orientations. It is shown that indentation-induced deformation in the composite materials obtained by FZM is distinct from the deformation expected in their equilibrium state. This difference arises in part from residual thermal strains in both phases of the composites in a FZM -grown state. Interplay between residual thermal deformations and external mechanical deformation results in a complex distribution of dilatational strain in the LaB_6 matrix and TiB_2 fibers and differs in composites of different orientations. Reversal sign of the stress-strain state (e.g., alternating tensile/compressive/tensile in central part of the cross-section area) is observed predominantly in the matrix LAB_6 and the TiB_2 fibers of the composite with the orientation <111>. In the composite with the orientation <100>, this change in the deformation sign was not observed. The size and spread of cracks after indentation-induced deformation shows a decrease in microhardness in FZM -grown composites of <111> significantly more (40%) than in composites with a orientation of <100> (10%) compared with an equilibrium state.*

Keywords: BORIDE COMPOSITE, FRACTURE TOUGHNESS, DIRECTIONAL SOLIDIFICATION, RESIDUAL STRESSES, EUTECTIC ALLOY, MONOCRYSTALLINE STRUCTURE

1. Introduction

Progress of the technologies for receiving composite materials by directionally solidification including floating zone method (FZM) allowed significantly improved the mechanical properties of single crystals and composites [1-4]. The FZM process are characterized by significant temperature gradients along and perpendicular to the direction of movement of the melting zone and cause residual stresses (RS) in the matrix and fibers of composite. Previous studies [4,8 -10] also show that the strength and plasticity of the directionally solidified LaB_6–MeB_2 (Me–Ti, Zr, Hf) eutectics depends on the crystallographic orientation of the matrix phase (LaB_6). On the mechanical characteristics of composites with a reinforcing phase in the form of fibers, the decisive influence is the interface boundary, that is, the strength of the adhesion of fibers with the matrix. Under the interface boundary in this case, it is understood not only the geometric [5] surface of the separation between fibers and the matrix, but also adjacent to it areas, which are affected by the influence of physicochemical and thermomechanical processes occurring in the stages of formation of the composite.

It is believed [11] that for the mechanical characteristics of composites with a reinforcing phase in the form of fibers, the decisive influence is the interface boundary, that is, the strength of the adhesion of fibers with the matrix. Under the interface boundary in this case, it is understood not only the geometric surface of the separation between fibers and the matrix, but also adjacent to it areas, which are affected by the physicochemical and thermomechanical processes occurring at the composites stages formation. The morphology of the phases formed during the FZM depends on a number of factors, but the most important is the ratio of the rate of their origin and growth, which in turn depends to a large extent on the thermal conditions and the supercooling at the crystallization front. Under the interface boundary in this case, it is understood not only the geometric surface of the separation between fibers and the matrix, but also adjacent to it areas, which are affected by the physicochemical and thermomechanical processes occurring at the composites stages formation.

The technological experimental parameters of the FZM process: the velocity of the melting zone, the temperature gradient values, the shape of the crystallization front provides conditions for the formation of nucleus (nucleation) of different orientations. Growth of grains with crystallographic orientation [001] according to the model [12] there is an advantage, since they occur at the slightest supercooling. Under the same conditions of crystallization, composites with different orientations of the seeds will have different conditions in terms of the competitive growth of the nucleus at the crystallization front. As a result of the directionally FZM method the thermal RS occur in both phases and are described by the stress tensor [13]. With a uniform action of external forces, internal stresses are described by a symmetrical stress tensor with only diagonal terms. The non-coincidence of the directions of preferential growth and the maximum temperature gradient leads to the fact that the stress tensor becomes asymmetric, i.e. shear, tangential stresses are present in the material. The sign of the acting force (RS) on the environment on the composite side is opposite to the sign of the external force (temperature gradient) acting on the composite.

The RS sign determines their effect on fracture propagation with an additional mechanical effect on the composite. Investigation the crack spread under the indent is the main testing in LaB_6-based ceramics to characterize a stress-strain state [9, 14-17]. Internal RS measurements have already been performed in ceramic eutectics using either X-ray or neutron [9, 17–21] diffraction techniques.

The aim of the experiment was to establish the interrelation between cracks propagation and stress-strain state of LaB_6-TiB_2 composites obtained on the seeds with different orientations by the FZM method.

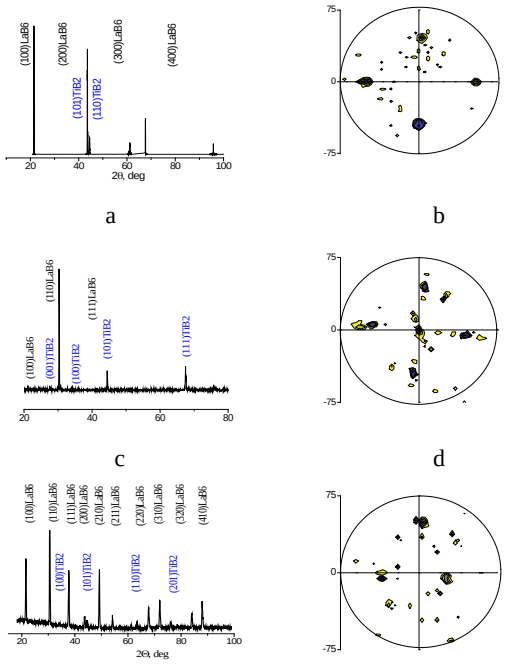
2. Experimental procedure

The LaB_6 and TiB_2 powders (purity 98 wt. % , average grain size 1 μm, Reaktiv Co Donetsk, Ukraine) were mixed in the eutectic, 89 wt. % LaB_6 and 11 wt. % TiB_2, composition. In order to assist the purification of the starting powder mixture during crucible-free FZM, 2 vol. % amorphous boron (purity 99.8 wt%, particle size 0.5 μm, Reaktiv Co Donetsk, Ukraine) powders was admixed. 15 ml of a 2.5 wt% polyvinyl alcohol aqueous solution was used as binder per 100 g of powder mixture. After mixing by 10 times manual wet sieving through a 100 μm mesh sieve, the dried powder mixture was sieve granulated (1000 mm mesh) and uniaxial pressed in a hydraulic press at 100 MPa in a steel cylindrical mold with a working cavity diameter of 10 mm and length of 145 mm. Directionally reinforced LaB_6–TiB_2 composites were obtained by the original floating zone method, developed at the National Technical University of Ukraine (NTUU “Igor Sikorsky KPI”). FZM was performed at a speed of 3 mm/min in the "Crystal 206"(Russia) induction equipment in a 0.1 MPa helium

environment using single crystal LaB_6 substrate seeds with <100>, <110> and <111> orientations. 5-6 samples for studies were cut perpendicular to the axis of the central part of each cylindrical crystal. The disks (d = 8 mm, h = 6-8 mm) were polished with diamond suspensions of 15 and 3 μm. Microstructure investigation of the composites was performed by scanning electron microscopy (PEM 106I). X-ray diffraction investigations were produced on a XRD diffractometer (Ultima IV, Rigaku, Japan) using $Cu_{K\alpha}$ radiation, a 2Θ step size of 0.02° and measuring time of 2s/step. The RS in different planes were determined by the sin2Θ method. To reduce the error in the determination of RS (up to <20-25%) measurements were made on ~10 different sample regions and with their inclination in opposite directions. The microhardness was measured by Vickers pyramidal indentation (MHV-1000 microhardness tester with time exposure 15 s, and averaging 7 measurements under a load of 30N. The fracture toughness on the transverse cross-section was computed from the Vickers hardness, using the expression proposed by Evans and Charles for Palmqvist cracks [22].

3. Results and discussion

The distribution of intensity on "Θ-2Θ" X-ray diffraction patterns and pole figures for different LaB_6-TiB_2 composites is shown on fig 1. For composites of all orientations there are reflexes for the matrix phase (LaB_6) and fibers (TiB_2) (Fig 1 a, c, e). The content of the matrix phase is ~ 87-89 wt.% and the fibers are ~ 11-13 wt.%. A significant number of reflexes are observed on the pole figures (Fig. 1 b, d, f) of samples for all orientations. Reflexes with a high intensity in accordance with their positions allow one to determine the preferential orientation of the samples, which repeats the orientation of the substrates. The symmetry of fourth-order for the high intensity reflexes is observed in composite produced on a substrate <100>, and for composites on substrates <110> and <111> there are the second and third orders, respectively. The total intensity of polycrystalline reflexes at the pole figures FZM-grown composites allow us to estimate their volume in ~8-20%. The volume of polycrystalline components of composites depends on the orientation of the substrate and can be reduced during annealing of composites [21]. Polycrystalline constituents of composites are represented on "Θ-2Θ" diffraction patterns (Fig. 1a, c, e) as additional to single-crystal reflexes.



a,b – <100>; c, d – <110>; e, f – <111>

Fig 1. *«θ–2θ» X-ray diffractograms and pole figures matrix components LaB_6 of composite LaB_6-TiB_2*

The significant temperature gradients and difference in the coefficients of thermal expansion leads to the fact that when cooled sintered by FZM composites from temperatures below which the phases cannot be plastically deformed, there is the formation of internal stresses around not only a fibers interface with a larger coefficient of thermal expansion (CTE) compared with the matrix but in the matrix and the fibers. The coefficient of thermal expansion matrix phase LaB_6 is ~6 10-6 K^{-1} [23] and for TiB_2 in c-axis is ~ 9.3 10-6 K^{-1} and in a-axis is ~ 6.35 10-6 K^{-1} [24]. In the equilibrium state LaB_6-TiB_2 composites have only interfacial stresses to which at FZM in conditions of significant temperature gradients added residual macrostresses in the composites components.

The orientation of the seed during the formation of composite materials is also main key factors shaping the residual stresses after FZM. On the Fig. 2 [6] shown the distribution of residual stresses in cross-sections of crystals obtained with different moving speed with orientations of the axes <111> and <100> having symmetries of 3 and 4 orders respectively.

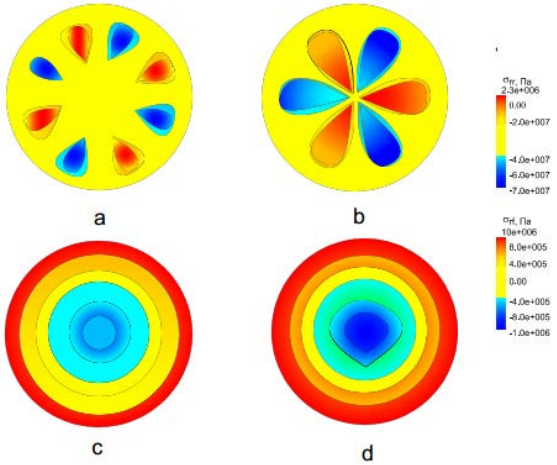


Fig. 2. *Cylindrical stress components σ_{rr} (middle) and $\sigma_{r\phi}$ (bottom) on the crystallization interface of FZM crystals with <100> (a, c) and <111> (b, d) orientation and a growth rate of 2.5 mm/min*

For the orientation of crystals <100>, the lateral surface of the cross sections is in a tensile state while the central part is compressed, which corresponds to a negative value of the shift on the X-ray diffraction patterns. As the crystallization rate decreases, absolute values of residual stresses decrease. The change in the sign of the stresses from the center to the lateral surface is symmetrical and occurs uniformly for any radial direction. In crystals with orientation <111>, a change in the sign of RS along the circumference is observed. As the rate of crystallization decreases, the absolute values of the residual stresses decrease, but the change in the stress sign remains, albeit in a smaller region of the material. The distribution of RS (Fig. 2) in the cross section of single crystals is related to the mutual position of the sliding planes, the direction of preferential growth and the temperature gradient at the crystallization front.

On the X-ray diffraction patterns, this is manifested in a change in the displacement of the reflexes when the slope of the sample is changed, which is used in the "$\sin^2\psi$" method (Fig.3). The leading parameter in analyzing the characteristics of growth is the growth rate. Each type of plane grows at a certain speed. The growth rate is directly proportional to the number of atoms forming the plane, and is calculated as the ratio of the number of atoms entering the plane to the area of the plane, that is, determined by the reticular density. For La atoms, the relative reticular density of the different planes is: {100}: {110}: {111} as 1: 0.707: 0.650.

In Fig.3, for disk samples of composites {100} (Fig.3a) and {111} (Fig.3b), the change of the RS in different planes is shown. Differences in the RS values significantly exceed the measurement error. In composites {100} a different level of compressing RS is

observed in different planes and for all planes in the cross-section are dominated by compression stresses. In the composite {111}, not only different levels of RS are observed in the planes, but also different signs of these RS. It is very important to note that in the matrix phase of the composite in different directions, a different sign is formed. The complex-stress state is characteristic for composites obtained by FZM process.

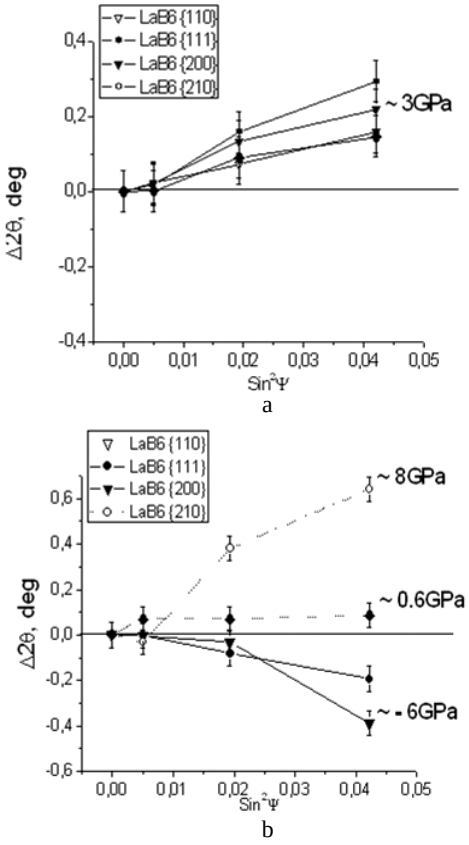


Fig 3. *The residual macrostresses in various planes of the matrix phase of the composites <100> (a) and <111> (b), which are determined by the sin²ψ method on the transverse sections of the samples*

The residual stresses significantly affect the mechanical behavior of the material. Concerning the crack propagation modes, tensile stresses within a phase will act in favor of transverse crack propagation in this phase, whereas a normal tensile stress on the phase boundaries will help the interface crack propagation [9, 14-17]. Interplay between RS and external mechanical deformation (indentation of a pyramid) results in a complex distribution of dilatational strain in the LaB_6 matrix and TiB_2 fibers and differs in composites of different orientations. This interaction is manifested in the peculiarities of the propagation of cracks. In Fig.4 shows the microstructures of composites with pyramid indentation obtained on substrates with orientations of {100}, {110} and {111}. Common for cracks in composites of all orientations due to the indentation of the pyramid is their formation and stopping in the matrix phase, enveloping the reinforcing fibers and not penetrating the matrix-fiber interface. The peculiarities of the appearance of cracks in composites of different orientations are the regions of generation and the directions of their propagation relative to the diagonals of the indentation. In the {100} composites cracks originate from the tops of indentation area and extend in the direction of their diagonals, corresponding to the places and directions of the maximum load (Fig.4a). The microstructure of the {111} composite in the region of the indentation with cracks is shown in Fig.4b. In the area of indentation, we can distinguish several grains that easily differ in the position of the fibers in them (Fig.4c). Cracks are generated and propagated in any direction relative to the maximum load (diagonals of the indentation) and the melting direction of the zone.

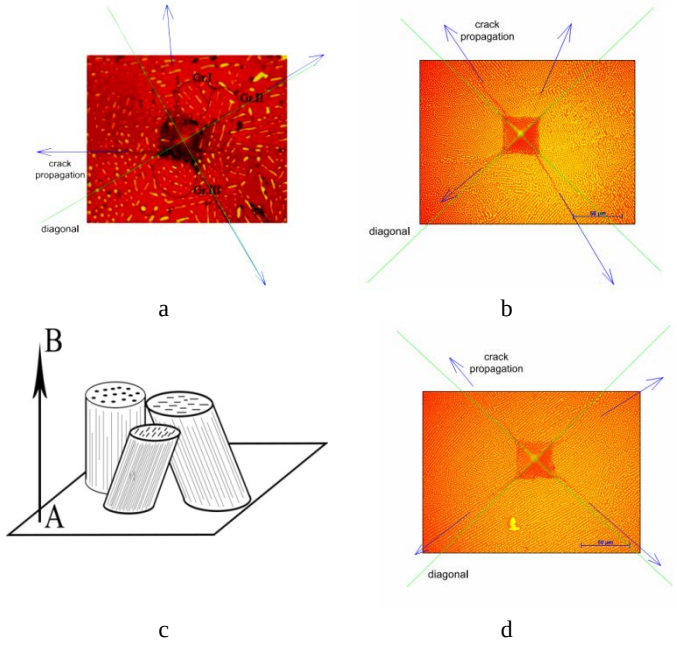


Fig 4. *Typical microstructures indentations (a, b, d) in composites with orientations <111> (a), <110> (b), <100> (d) and scheme grains structure in composite <111> (c); directions of cracks propagation (blue lines) and diagonals indentations (green lines), AB - direction of the maximum temperature gradient*

The distribution of cracks indicates the existence of regions with a lighter and more difficult motion in the matrix phase. In composites with these orientations, RS of different signs were found, which leads to the formation of a complex stress state. The measurement of the crack length after Vickers indentation (tab. 1) shows very strong anisotropy for single crystals with different direction of crystallization.

Table 1 – *Anisotropy crack length in the single crystals LaB_6-TiB_2 composite after FZM*

Direction of crystallization	<100>	<110>	<111>
Anisotropy of crack length, %	7.8	29.7	41.5

To the anisotropy of the coupling of the atoms of lanthanum and boron in the matrix LaB_6 and taking the interaction between the matrix and the fibers is added to the complex stress-strain state arising as a result of FZM process.

4. Conclusions

In ceramic composites produced by FZM, residual stresses are formed, which determine their crack resistance. In the cross sections of composites obtained in seedlings with different reticular densities, different residual stresses are observed not only in magnitude but also in sign. When using the seed {111}, the matrix phase of the composite is in a complex stressed state with an inhomogeneous distribution of residual compressive and tensile stresses. The larger the reticular density, the greater the rate of equilibrium crystallization and the more homogeneous RS are observed. Conversely, the smaller the reticular density, the lower the rate of equilibrium crystallization and the more complex the stress state is formed in the composites. The same rate of crystallization of composites of different orientations occurs with different supercooling and bending at the crystallization front. The

deviation of the direction of the preferential growth of the crystal from the maximum temperature gradient leads to additional deformations of the composites.

5. References

1. H. Bei, E.P. George, Microstructures and mechanical properties of a directionally solidified NiAl–Mo eutectic alloy, *Acta Materialia*, Vol. 53 (2005), p. 69–77.

2. V. M. Orera, I. Merino, A. Pardo and etc., Microstructure and physical properties of some oxide eutectic composites processed by directional solidification, *Acta mater.*, Vol. 48 (2000), p. 4683–4689.

3. R.S. Bradt, V.S. Stubican, Eutectic solidification in ceramic systems, *Ann. Rev Mater. Sci*., Vol. 11 (1981), p. 267–297.

4. I. Bogomol, T. Nishimura, O. Vasylkiv and etc., High-temperature strength of directionally reinforced LaB_6–TiB_2 composite, *J. of Alloys and Compounds*, Vol. 505 (2010), p. 130–134.

5. Q. Ren, H. Su, Ju. Zhang and etc., Directional solidification and growth characteristics of Al2O3/Er3Al5O12/ZrO2 ternary eutectic ceramic by laser floating zone melting, *J. Mater. Sci.*, Vol. 52 (2017), p. 5559–5568.

6. I. Drikis, M. Plate, Ju. Sennikovs and etc., Effect of process parameters and crystal orientation on 3D anisotropic stress during CZ and FZ growth of silicon, *J. of Crystal Growth*, Vol. 12 (2016).

7. A. Augusto, D. Pera, H. J. Choi and etc., Residual stress and dislocations density in silicon ribbons grown via optical zone melting, *J. of Applied Physics*, Vol. 113 (2013), p. 083510-1 - 083510-7.

8. W.-T. Chen, R.M. White, T. Goto and etc., Directionally Solidified Boride and Carbide Eutectic Ceramics, *J. Am. Ceram. Soc.*, Vol. 99 (2016), p. 1837–1851.

9. I. Bogomol, T. Nishimura, Yu. Nesterenkoa ant etc., The bending strength temperature dependence of the directionally solidified eutectic LaB_6–ZrB_2 composite, *J. of Alloys and Compounds*, Vol. 509 (2011), p. 6123–6129.

10. Yu. Paderno, V. Paderno, V. Filippov, Some Peculiarities of Eutectic Crystallization of LaB_6–$(Ti,Zr)B_2$ Alloys, *J. Solid State Chem.*, Vol. 154 (2000), p. 165–167.

11. H. Volkova, V. Filipov, Yu. Podrezov, The influence of Ti addition on fracture toughness and failure of directionally solidified LaB_6–ZrB_2 eutectic composite with monocrystalline matrix, *J. of the European Ceramic Society*, Vol.14 (2014), p. 3399-3405.

12. D.Walton, B. Chalmers, The origin of the preferred orientation in the columnar zone of ingots, *Transaction of AIME*, Vol. 215 (1959), p. 447-452.

13. L.D Landau,. E.M. Lifshitz, Theory of elasticity, Oxford ; New York : Pergamon Press, 1970, 168 p.

14. P.I. Loboda, Features of Structure Formation with Zone Melting of Powder Boron-Containing Refractory Materials, *Powder Metall. Met. Ceram.*, Vol. 39 (2000), p. 480–486.

15. H. Deng, E.C. Dickey, Y. Paderno and etc., Crystallographic characterization and indentation mechanical properties of LaB_6-ZrB_2 directionally solidified eutectics, *J. Mater. Sci.*, Vol. 39 (2004), p. 5987–5994.

16. Yu. Paderno, V. Paderno, V. Filippov, Directionally Crystallized Ceramic fiber-Reinforced Boride Composites, *J. Solid State Chem.*, Vol. 154 (2000), p. 165–167.

17. G.E. Ice, R.I. Barabash In: Nabarro FRN, Hirth JP, Strain and Dislocation Gradients from Diffraction: Spatially-Resolved Local Structure and Defects, *Dislocations in solids*, Vol. 13 (2007), p. 500–60.

18. E.C. Dickey, C.S. Frazer, T.R. Watkins and etc. Residual stresses in high-temperature ceramic eutectics, *J. Eur. Ceram. Soc.*, Vol. 19 (1999), p. 2503–2509.

19. H. Suzuki, K. Akita, Y. Yoshioka and etc., Evaluation of phase stresses of Al sub 2 O sub 3 /YAG binary MGC by synchrotron radiation. Residual stress states and stress behavior of YAG phase, *J. Soc. Mater. Sci. Jpn.*, Vol. 52 (2003), p. 770–775.

20. S. Torii, T. Kamiyama, K. Oikawa and etc., Strain measurement of the directionally solidified eutectic Al2O3/Y3Al5O12 (YAG) ceramic by neutron diffraction, *J. Eur. Ceram. Soc.*, Vol. 25 (2005), p. 1307–1311.

21. P.I.Loboda, O.P. Karasevska, T.O. Soloviova, Mode of Deformation of Phase Components of a Ceramic Composite LaB_6-TiB_2, *Metallofiz. Noveishie Tekhnol*., Vol. 38 (2016), p. 1249-1263 (in Ukrainian).

22. F. Sergejev, M. Antonov, Comparative study on indentation fracture toughness measurements of cemented carbides, *Proc. Estonian Acad. Sci. Eng.*, Vol. 12 (2006), p. 388–398.

23. N. N. Sirota, V. V. Novikov, V. A. Vinokurov and etc., Temperature dependence of the heat capacity and lattice constant of lanthanum and samarium hexaborides, *Fiz. Tverd. Tela* (St. Petersburg), Vol. 40 (1998), p. 2051–2053.

24. Norihiko L. Okamoto, Misato Kusakari, Katsushi Tanaka and etc., Anisotropic elastic constants and thermal expansivities in monocrystal CrB2, TiB2, ZrB2, *Acta Materialia*, Vol. 58 (2010), p. 76–84.

C-BETAVOLTAIC ENERGYCONVERTER IN POR-SIC/SI

V.I.Chepurnov[1], M.V.Dolgopolov[1], A.V.Gurskaya[1], A.A.Akimchenko[1], O.V.Kuznetsov[1], A.V.Radenko[2], V.V.Radenko[2], A.S.Mashnin[3]
(Samara University, Institute of Natural Sciences)[1], (MEC QUASAR Ltd)[2] (SPAIT LlC)[3]

Abstract*. The miniature and low-power devices with long service life in hard operating conditions like the ^{14}C ß-decay energyconverters indeed with eternal resource for integrated MEMS and NEMS are considered. Authors will discuss how to create a power source for MEMS devices, based on SiC/Si porous structure, which are tested to be used as the β-decay energyconverter of radioactive carbon-14 into electrical energy. This is based on the silicon carbide obtaining by self-organizing mono 3C-SiC endotaxi on the Si substrate.*

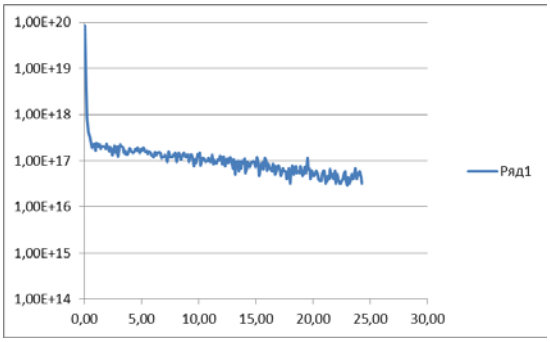
Introduction. The development of energy-saving technologies, the functioning of the MEMS devices, the reliability of their operation for a long time in offline conditions led to the search of appropriate means of generating energy for them. The work of authors will discuss how to create the power source for MEMS devices based on por-*SiC/Si* porous structure, which is tested to be used as the *β*-decay energy converter of radioactive carbon-14 into electrical energy [1,2,3,4]. This involves silicon carbide obtaining by self-organizing mono 3*C*-*SiC* endotaxi way on the *Si* substrate [5,6].

Energyconverters of beta radiation are based on isotopes transformations reactions with half-lives of more than 100 years. Energy converters are designed to secure operational performance, allowing reinstallation on the objects with the corresponding lifetime. Analogues were brought out to the laboratory samples level for two years. The groundwork of this project on the part of semiconductor technology: mastered growing por-*SiC/Si* heterostructures. The groundwork for the development of an energy source not specified. But there is information of methods and businesses with similar activities. The use of the product will effectively solve the following problems: the provision of energy for autonomous systems and devices, MEMS devices, sensors in oil capital constructions as example, information systems, systems, including medical direction and equipment.

Self-organizing mono 3*C*-*SiC* endotaxy technology. Authors present an original technology of manufacture and a model of the isotope energy converter based on the silicon carbide heterostructure, with carbon-14 as fuel. The radionuclide ^{14}C is incorporated into the *SiC* molecule instead ^{12}C in the por-SiC phase *in-por-SiC/SiC/Si* heterostructure. Beta-radiation generates nonequilibrium charge carriers, separated by the internal field of *p-n* junction in the *SiC*-phase. The concept is based on the semiconductor implantation technology of the solid-phase transformation according to the diffusion model of the *Si*-phase transformation into the *SiC*-phase, which allows the buildup of por-*SiC* heterostructures [6,7]. This is also possible to achieve by ion implantation of carbon-14 into the silicon carbide phase. The latter approach to the direct conversion can increase the effectiveness of beta-voltaic energyconverters.

The method of secondary ion mass spectrometry (SIMS) is used to analyze the composition of solid surfaces and thin substrates. The essence of the method is to irradiate the sample surface by a focused beam of ions (primary ions). When hitting the sample, the primary ions undergo multiple collisions, which are emitted from the sample atoms and clusters of atoms in the process of collisions, the latter spontaneously ionized (forming secondary ions). These secondary ions are collected in the secondary beam and analyzed.

KDB_C. The analyzed depth ranges from $5.3*10^{-8}$ to $24.3*10^{-6}$ m. The concentration of ^{12}C atoms, depending on the analyzed depth ranges from $8.4*10^{19}$ to $3.2*10^{16}$.



There are two competitive directions of the beta-voltaic converters development: the accumulation of charges in the reactions of transformation of elements using supercapacitors; the charge separation in *p-n* junction of the solar battery analogue; the combination of the two directions. In all cases, the main competitive advantage over other energy sources is the long life cycle of beta-converter. A disadvantage is due to low capacity and low efficiency, which is overcome technological way (a higher degree of enrichment of isotope using the developed nanoporous surfaces, reducing the leakage current of super capacitor and *p-n* junction, using a combination of several sources of beta-radiation flux; the system microcontroller, which controls the flow of the charge).

The ratio ‘price/performance' is determined by several factors: semiconductors heterostructures provide a price level conventional semiconductor discrete diodes or transistors, high power, the technology of nuclear fusion, the working fluid used in the operation of medical devices provide a level of price acceptable to the consumer, when there is no alternative.

Planning design parameters and performances are following: Voltage range ~ 2 mV, Size of the device ~ 10×10×(0.3÷0.5)mm, Mass of each structural element 0.17 g, Working current range 0.1μA, Working temperature range -50° ÷ 350° C.

Magnetooptic synthesis chamber. The synthesis of carbon-14 can be also performed by using the electronically controlled synthesis of nucleons in the 8-cyclic magnetooptic synthesis chamber. The setup consists of electronically controlled ion sources with magnetooptic flux concentration with the ion energy of up to 50 keV, electronically controlled pulsed accelerator sections that form discrete ion flux with the ion energy from 200 to 600 keV, combined with an 8-cyclic magnetooptic synthesis chamber and a controlled magnetodynamic trap for generating dense neutron fluxes. The synthesis of ^{14}C by neutrons goes in a 4-cycle magnetooptic chamber on a dense ion target. At the final stage, ^{14}C from the magnetooptic storage is deposited on the *SiC* substrate. Multilayer formation of ^{14}C on a *SiC* substrate or on substrates from other materials is also possible.

Comparison. Note the comparison with a technology that uses Nickel-63.

1. The production of ^{14}C in the dense ion plasma flow is much cheaper than the production of ^{63}Ni in Nickel target, due to the low cost of ^{14}N.

2. Ion-plasma implantation ^{14}C on *SiC* substrate allows to reduce the crystal production process and realize mass production on semiconductor converters ^{14}C.

3. At the same time, the production of ^{63}Ni by this technology is

possible, and the cost will be much reduced compared to traditional methods. Because of the greater mass of the ions, the equipment for ion-plasma sputtering with a seal of the flow of Nickel ions will be several times more expensive because of increased size of the installation. At this stage, it is more sophisticated to produce ^{14}C.

4. Specific activity of ^{14}C is different from the ^{63}Ni in terms of unit volume about 10 times, due to the huge difference in half-life times.

5. Self-absorption of ^{63}Ni is higher by approximately three times, which leads to the maximum optimal thickness of the layer to 4 microns, and for ^{14}C, this thickness is about 60 microns, which is better suited. The total quantity of the isotope ^{14}C may be an order of magnitude greater, therefore, guaranteed more power for the same size of power converters.

6. The specific power of ^{63}Ni per g of the substance 5 times (due to more activity) exceeds the power density of ^{14}C. But the maximum and average energies of electrons in the decay of ^{14}C is 2 to 3 times more than in the decay of ^{63}Ni.

7. The production cost of ^{14}C 12 mg will take 8 hours, taking into account equipment depreciation, will cost about 170$.

Summary. *This development is intended for practical applications in MEMS and NEMS systems and sensors that require long-term autonomous operation.*

References

[1] V.I.Chepurnov, M.V.Dolgopolov, A.V.Gurskaya, S.N.Podgornov, A.N.Scherbakov Por-SiC/Si heterostructure for applied purposes // International Conference "Electronics-2015", 2015, P.13.

[2] A.V.Gurskaya, V.I.Chepurnov, M.V.Dolgopolov C-14 Beta decay energyconverters // 22 All-Russian Scientific Conference of physics students and young scientists, April 21-28, Rostov, 2016, P.183.

[3] S.P.Zavodov, V.I.Chepurnov, A.A.Kirpichev Development of betavoltaic power supply on the energyconverter-based C-14 beta decay with up to 100 years for MEMS. In book: Modern problems of physics and technologies. MEPhI. 2016. 189-191 pp.

[4] The Patent Application №2016129598, 19.07.2016.

[5] The Patent of The RUSSIAN FEDERATION №02370851 C2 Method of self-organizing mono 3c-SiC endotaxi on Si substrate / V.I.Chepurnov, since 15.12.2005.

[6] ROSRID, R & D report, with references to the literature, V.I.Chepurnov, etc. AAAA-B16-216122220098-7.

[7] CHEPURNOV V.I., Dolgopolov M.V., GURSKAYA A.V., SOROKOV A.S. ON THE POSSIBILITY OF USING AUTONOMOUS POWER SOURCES FOR MICRODROPERS IN CAPITAL CONSTRUCTIONS. OIL. GAS. NOVATSIYA. Number: 12 Year: 2016 Pages: 80-82.